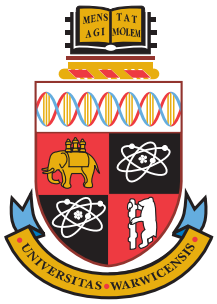

Experimentally Verified Reduced Models of Neocortical Pyramidal Cells

by

Paul Michael Harrison

Thesis

Submitted to the University of Warwick

for the degree of

Doctor of Philosophy

in

Mathematical Biology and Biophysical Chemistry

Supervisors: Dr Magnus J. E. Richardson and Dr Mark J. Wall

MOAC Doctoral Training Centre

October 2014

THE UNIVERSITY OF WARWICK

Contents

List of Figures

List of Tables

Acknowledgements

First and foremost I would like to thank my supervisors, Dr Magnus Richardson and Dr Mark Wall, for their continued support and advice throughout the course of this project. Their contribution has been invaluable and this work would not have been possible without them. I would also like the thank my advisory committee members Prof. Matthew Turner, Dr Dawn Collins, and Dr Till Bretschneider for their helpful advice, and also Prof. Alison Rodger for going above and beyond the scope of her position to support my cohort and I throughout the last three years. I would also like to extend my gratitude to the Molecular Organisation and Assembly in Cells Doctoral Training Centre and the Engineering and Physical Sciences Research Council for funding this research.

I would like to thank the Richardson-Wall research group for their continuing support and stimulating discussions, and in particular Dr Francesco Fermani for proof reading this work. A special mention must also go to Dr Michael Kerr for his extensive experimental assistance during the early months of my PhD. My heartfelt thanks also goes to my MOAC cohort for making post-graduate life bearable, providing a constant source of entertainment, and off-topic mathematical discussions. Finally, I would like to thank my parents, brother, and girlfriend for their unwavering love and support throughout my PhD.

Declarations

I, Paul Michael Harrison, declare that, to the best of my knowledge, the material contained in this thesis is original and my own work except otherwise indicated, cited, or commonly known. I confirm that this thesis has not been submitted for a degree at another University. Chapters 4 and 5 have been accepted for publication in *PLoS* Computational Biology (Experimentally verified parameter sets for modelling heterogeneous neocortical pyramidal-cell populations, in press).

Abstract

Reduced neuron models are essential tools in computational neuroscience to aid understanding from the single cell to network level. In this thesis I use these models to address two key challenges: introducing experimentally verified heterogeneity into neocortical network models, and furthering understanding of post-spike refractory mechanisms.

Neocortical network models are increasingly including cell class diversity. However, within these classes significant heterogeneity is displayed, an aspect often neglected in modelling studies due to the lack of empirical constraints on the variance and covariance of neuronal parameters. To address this I quantified the response of pyramidal cells in neocortical layers 2/3-5 to square-pulse and naturalistic current stimuli. I used standard and dynamic I-V protocols to measure electrophysiological parameters, a byproduct of which is the straightforward extraction of reduced neuron models. I examined the between- and within-class heterogeneity, culminating in an algorithm to generate populations of exponential integrate-and-fire (EIF) neurons adhering to the empirical marginal distributions and covariance structure. This provides a novel tool for investigating heterogeneity in neocortical network models.

Spike threshold is dynamic and, on spike initiation, displays a jump and subsequent exponential decay back to baseline. I examine extensions to the EIF model that include these dynamics, finding that a simple renewal process model well captures the cell's response. It has been previously noted that a two-variable EIF model describing the voltage and threshold dynamics can be reduced to a single-variable system when the membrane and threshold time constants are similar. I examine the response properties of networks of these models by taking a perturbative approach to solving the corresponding Fokker-Planck equation, finding the results in agreement with simulations over the physiological range of the membrane to threshold time constant ratio. Finally, I found that the observed threshold dynamics are not fully described by the inclusion of slow sodium-channel inactivation.

Abbreviations

2vEIF	Two variable exponential integrate-and-fire
5HT3A	5-hydroxytryptamine 3A
AdEx	Adaptive exponential integrate-and-fire
AHP	Afterhyperpolarization
AMPA	α-Amino-3-hydroxy-5-methyl-4-isoxazolepropionic acid
ATrEIF	Accumulating threshold refractory exponential integrate-and-fire
BC	Basket cell
CC	Corticocortical
ChC	Chandelier cells
CT	Corticothalamic
EIF	Exponential integrate-and-fire
FN	FitzHugh-Nagumo
GABA	γ-Aminobutyric acid
HH	Hodgkin-Huxley
HR	Hindmarsh-Rose
IF	Integrate-and-fire
L2/3	Layer 2/3
L4	Layer 4
LIF	Leaky integrate-and-fire
MAT	Multi-timescale adaptive threshold
ML	Morris-Lecar
NG	Neurogliaform cells

NIF	Non-linear integrate-and-fire
NMDA	N-methyl-D-aspartate
OOB	Out-of-bag
PC	Principal component
PCA	Principal component analysis
PV	Parvalbumin-expressing
rEIF	Refractory exponential integrate-and-fire
SL5	Slender-tufted layer 5
SOM	Somatostatin-expressing
SRM	Spike response model
STR	Spike-triggered rate
TL5	Thick-tufted layer 5
VIP	Vasoactive intestinal peptide
WB	Wang-Buzsáki

Chapter 1

Introduction

Neurons are the fundamental electrically active computational unit of the brain. Understanding their behaviour is a prerequisite in comprehending more complex structures, from small microcircuits to brain-wide activity. In this thesis I shall be focussing on furthering our understanding of neocortical pyramidal cells, which are of central importance to high level processes such as motor control, speech, and hearing. The aims of this project are twofold: to construct experimentally verified parameter sets for heterogeneous network models of the somatosensory cortex, and to better understand the mechanism behind spike-threshold variability.

This introduction will review the biological and mathematical aspects of neuroscience relevant to this project. I shall begin with an overview of the function and structure of the mammalian neocortex, with particular focus on the role of pyramidal cells in information transfer within cortical microcircuits. This will be followed by a review of action potential physiology, and specifically the potential mechanisms underlying spike threshold variability. Next I shall provide a summary of several important detailed and reduced mathematical models. Finally, the introduction will conclude with an outline of the content of this thesis.

1.1 The Neocortex

The neocortex is the most evolutionary recent part of the brain located in the outer cerebral hemispheres (Figure 1.1A) and is responsible for high level functioning such

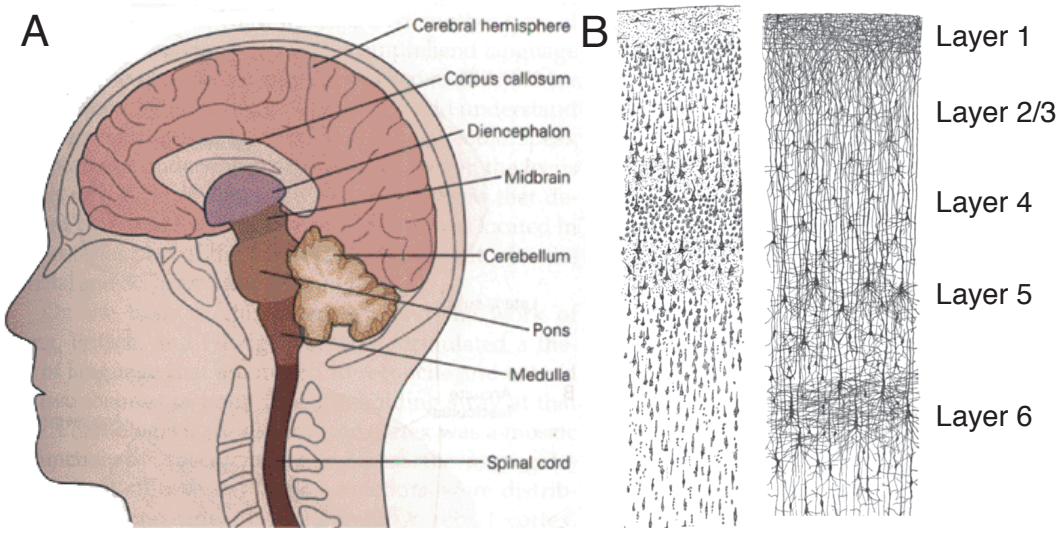

Figure 1.1: Location and structure of the neocortex in the mammalian brain. **A** Schematic of regions in the human brain (Kandel *et al.* 2000). **B** Nissl (left) and golgi (right) stain illustrating the layered structure of the neocortex (Ramón y Cajal 1909).

as motor control and conscious thought. Over the last 200 million years the neocortex has undergone significant expansion and diversification between mammalian species (Herculano-Houzel *et al.* 2008), with more complex behaviours typically correlated with a larger surface area and neuron number (Lui *et al.* 2011). It is divided into distinct layers characterised by a variety of neuronal physiologies, morphologies, and functions. This layered organisation of the cortex was famously illustrated by Ramón y Cajal (1909, Figure 1.1B) and has since been studied extensively in an attempt to relate these fundamental features to behaviour.

A complementary organising principal to this layered structure is the notion of cortical columns forming canonical microcircuits specialised for specific functions, an idea that is currently the focus of significant study (Markram 2006; Helmstaedter *et al.* 2007). First proposed by Mountcastle *et al.* (1957) as the fundamental cortical processing unit, examples of columns have subsequently been found in a range of species across a variety of regions (Hubel and Wiesel 1962; Woolsey and Van der Loos 1970; Bugbee and Goldman-Rakic 1983; Jones 2000; Buxhoeveden and Casanova 2002). However, the definition of a cortical column has broadened significantly over the last half century (Rakic 2008), leading some to question whether they have a functional role at all (Horton and Adams 2005).

Regardless of the ongoing debate over the existence and function of columns,

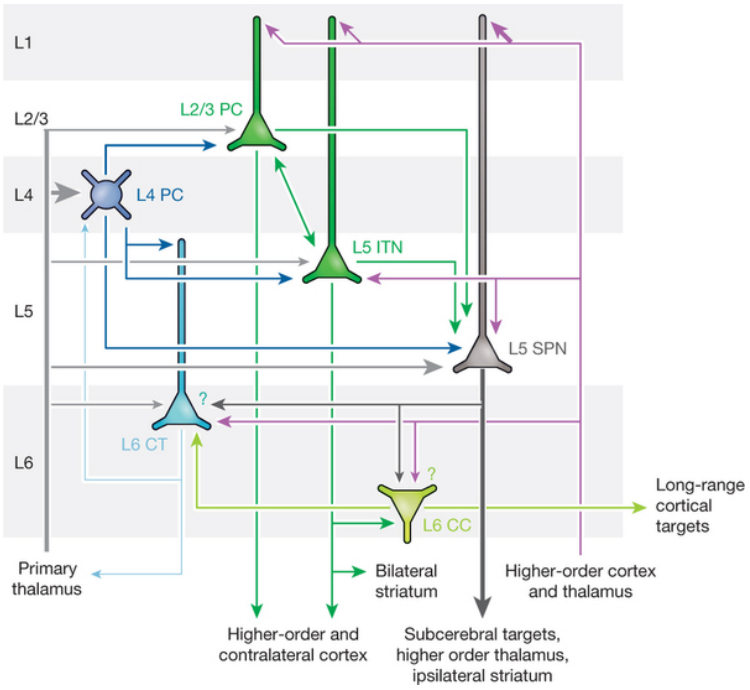

Figure 1.2: Schematic of the excitatory cell locations and connectivity in the neocortex (Harris and Mrsic-Flogel 2013).

canonical microcircuits are a key feature of information processing in the cortex, and indeed other brain regions (Grillner and Graybiel 2006; Cutsuridis *et al.* 2009b) such as the hippocampus (Cutsuridis *et al.* 2009a), and the cerebellum (Dean *et al.* 2009). Understanding microcircuits is currently one of the most important challenges in modern neuroscience (Silberberg *et al.* 2002; Douglas and Martin 2004; Harris and Mrsic-Flogel 2013).

1.1.1 Neocortical Microcircuits

What is most remarkable about microcircuits in the neocortex is that, despite different regions varying a great deal in function, there appears to be a large degree of stereotypy in their spatial organisation and connectivity (Jones 1999; Kozloski *et al.* 2001; Silberberg *et al.* 2002). Thus far attention has focussed primarily on sensory areas such as the visual, auditory, and somatosensory cortices, where a common organisational principal has emerged governing the flow of information between layers (Figure 1.2).

Layer 1 is the most superficial layer in the neocortex and primarily consists of distal dendritic arbours of pyramidal cells from lower layers. However, there is a

sparse population of neuronal somata consisting almost entirely of γ-aminobutyric acid (GABA) releasing interneurons (Hestrin and Armstrong 1996). Layer 1 primarily receives horizontal cortico-cortical feedback (Felleman and Van Essen 1991; Cauller and Connors 1994) that has been suggested to provide top-down contextual information to the bottom-up sensory signals arriving via the thalamus and other sub-cortical regions (Cauller 1995; Petreanu *et al.* 2013).

Layers 2 and 3 are generally considered as a single layer outside of the visual cortex (Gur and Snodderly 2008), and receive the strongest feed-forward excitation from layer 4. This is integrated together with input from other layers before being relayed to layer 5, the major output layer of the cortex projecting to the thalamus and other sub-cortical regions (Feldmeyer *et al.* 2002; Douglas and Martin 2004; Schubert *et al.* 2007; Feldmeyer 2012; Harris and Mrsic-Flogel 2013). This layer comprises a single pyramidal PC class, though it has been suggested these cells can be divided into sub-classes based on their morphology (Oberlaender *et al.* 2012; van Aerde and Feldmeyer 2013) and electrophysiology (Zaitsev *et al.* 2012; van Aerde and Feldmeyer 2013).

The granular layer 4 receives the strongest input from the primary thalamus. It comprises two principle cell (PC) morphologies, pyramidal and spiny stellate, although their physiology and function seem similar (Brecht and Sakmann 2002). Layer 4 is absent from the motor cortex, an area where the organisation has yet to be elucidated (Shepherd 2009; Hooks *et al.* 2011).

Layer 5 consists of two major classes of excitatory cells. Thick-tufted pyramidal cells, also referred to as subcerebral projection neurons (SPNs), are the major cortical output neuron located deeper in the layer (layer 5b) and tend to elicit bursts of action potentials. Slender-tufted pyramidal cells, also referred to as intratelencephalic neurons (ITNs), are located more superficially (layer 5a) and have a regular spiking pattern. In addition to layer 4, the layer 5/6 border receives significant input from the primary thalamus (Constantinople and Bruno 2013).

Finally, layer 6 is the least well understood layer comprising two primary principal cell classes (Oberlaender *et al.* 2012; Watakabe *et al.* 2012; Harris and Mrsic-Flogel 2013). Cortiocortical (CC) cells display a sparse dendritic structure, make

horizontal connections to long-range cortical targets, and display unique morphologies such as inverted somata (Thomson 2010). Corticothalamic (CT) cells send weak projections to the reticular and primary sensory thalamic nuclei (Sherman 2012), travelling via slow conducting fibres (Swadlow 1989). In addition, these cells also project to layer 4 where they strongly innervate interneurons (Watakabe *et al.* 2012) and can hyperpolarize principal cells via group II metabotropic glutamate receptors (Lee and Sherman 2009). Furthermore, layer 6 has been shown to exhibit gain control of other layers (Olsen *et al.* 2012), with CC neurons strongly activating layer 5a pyramidal cells whilst disynaptically inhibiting layer 4 (Kim *et al.* 2014).

1.1.2 Pyramidal Neurons

Pyramidal neurons, so called due to their pyramid-like cell body, are glutamatergic and are mainly found in structures associated with high level functioning such as the neocortex and hippocampus. In the neocortex they make up approximately 80% of the total number of cells (DeFelipe and Fariñas 1992) and their somata are found in all layers except layer 1. All pyramidal neurons in the brain are characterised by multiple branching dendrites and a single axon protruding from the base (Figure 1.3A). Although the main characteristics of pyramidal cells are relatively homogenous throughout the brain there is still a large degree of variation (Gao and Zheng 2004; Thomson and Lamy 2007; Spruston 2008; Oberlaender *et al.* 2012; van Aerde and Feldmeyer 2013).

With the exception of the diverse class of CC cells in layer 6 (Thomson 2010), neocortical pyramidal neurons share several key morphological features. A single apical dendrite protrudes from the apex of the soma that extends upwards to receive inputs from higher layers; in the case of thick-tufted layer 5 cells this can extend up to a millimetre into layer 1. In most cases this apical dendrite extends several hundred micrometers giving off oblique branches before separating further into a tuft. Multiple basal dendrites extend from the base of the neuron; they are not as thick or as far reaching as the apical dendrite and are thought to make up about 90% of the total dendritic length of the cell (Larkman 1991).

Pyramidal cells receive synaptic input across their dendritic processes, somata,

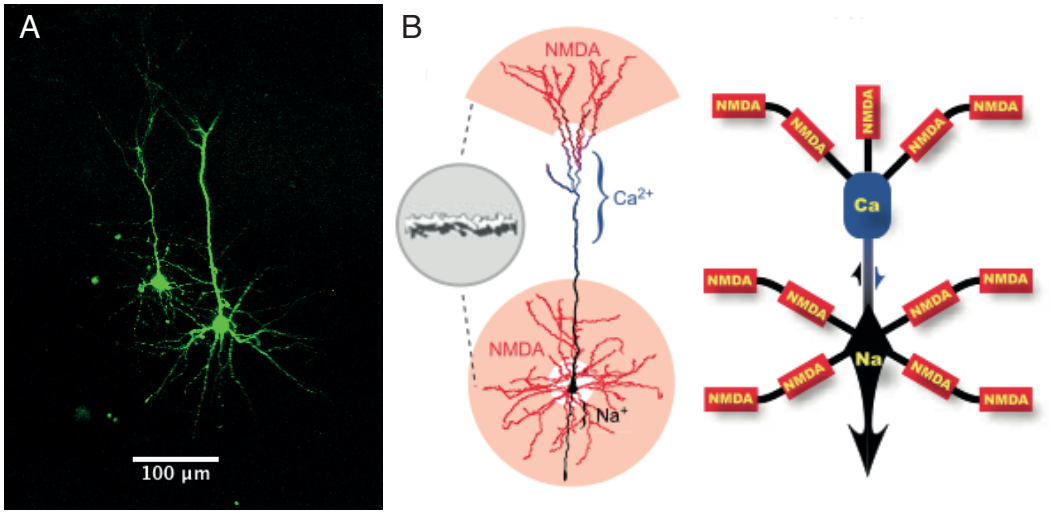

Figure 1.3: Morphology and synaptic integration in cortical pyramidal cells. **A** Two layer 2/3 pyramidal cells from the rat somatosensory cortex filled with a fluorescent dye and imaged using confocal microscopy. **B** Proposed unifying principal of synaptic integration in thick-tufted layer 5 pyramidal cells (Larkum *et al.* 2009).

and axon. This information is integrated at the axon hillock where, if sufficient input is received an action potential is generated. Different domains across the cell receive distinct inputs; the soma and axon receive primarily GABAergic inputs, whereas the majority of excitatory inputs arrive via the dendrites (Spruston 2008). The spatial extent of synaptic input is crucial for sensory processing (Chadderton *et al.* 2014), and the function of domain specific inputs are gradually being elucidated. For example, it has been suggested that excitatory input into the distal tuft dendrites of thick-tufted layer 5 pyramidal cells could provide gain control over the cell's output (Larkum 2004), and that in hippocampal CA1 pyramidal cells inputs to the main apical dendrites and oblique dendrites are integrated differently (Gasparini 2004; Losonczy and Magee 2006).

Dendrites can also generate active responses. The apical dendrite can illicit calcium mediated spikes, often initiated by back-propagating action potentials from the soma and leading to somatic action potential bursts (Kim and Connors 1993; Schiller *et al.* 1997; Larkum *et al.* 1999). *N*-methyl-D-aspartate (NMDA) receptor-dependent spikes are seen in both the basal (Schiller *et al.* 2000; Nevian *et al.* 2007) and tuft (Larkum *et al.* 2009; Palmer *et al.* 2014) dendrites. Furthermore, a three stage integration principle has been proposed for thick-tufted layer 5 pyramidal

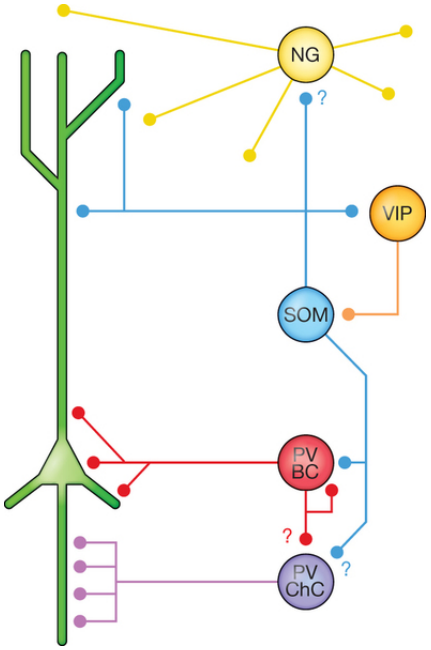

Figure 1.4: Schematic illustrating synaptic targets of the five classes of neocortical interneurons. Question marks illustrate connections that seem likely but have not yet been observed (Harris and Mrsic-Flogel 2013).

cells where these two active dendritic mechanisms, in combination with somatic and proximal voltage-gated sodium channels, contribute to information transfer through the cell to the axon hillock (Larkum *et al.* 2009, Figure 1.3B).

1.1.3 Interneurons

Interneurons are GABAergic cells and generally have an inhibitory effect of their targets. They are incredibly diverse in their morphological features, axonal targeting properties, and electrical response (Gupta *et al.* 2000; Markram *et al.* 2004). They do not typically have axons or dendrites that extend beyond the neocortex, but rather are mainly involved in local circuitry and lateral connections (Letinic *et al.* 2002); one can think of interneurons as providing the fine tuning to the main cortical output signals from pyramidal cells. Their most salient feature is their ability to target specific regions of principal cells (DeFelipe 1997; Somogyi *et al.* 1998; Wang *et al.* 2002; Silberberg and Markram 2007), leading to very specialised functions within the neocortical microcircuit.

There are three broad classes of interneurons in the neocortex (Rudy *et al.* 2010, Figure 1.4). Parvalbumin-expressing interneurons (PVs) are fast-spiking cells that

receive strong excitation from the thalamus (Cruikshank *et al.* 2007). The class comprises two sub-classes: basket cells (BCs), which target the perisomatic region of principal cells; and chandelier cells (ChCs), which target the axon initial segment and have either an inhibitory or excitatory effect when the network is in an active or quiet state, respectively (Woodruff 2009; Woodruff *et al.* 2010; Woodruff *et al.* 2011). The vast majority of somatostatin-expressing interneurons (SOMs) are Martinotti cells. These target the distal tuft region of principal cells where they heavily influence dendritic integration (Gentet *et al.* 2012), and have been shown to mediate disynaptic inhibition between thick-tufted layer 5 pyramidal cells (Silberberg and Markram 2007). Finally, the least well understood class of interneurons are the superficially located 5-hydroxytryptamine 3A (5HT3A) receptor expressing cells. This class consists of two main sub-groups: neurogliaform cells (NGs), which release GABA via volume transmission (Oláh *et al.* 2009); and vasoactive intestinal peptide (VIP) expressing cells, which primarily target SOM interneurons (Lee *et al.* 2013).

1.2 Action Potential Physiology

The action potential is the fundamental unit of communication between neurons. It is a brief, all-or-nothing event that propagates along the axon to synapses with other cells, resulting from the integration of sufficient synaptic input to drive the cell's membrane potential above a threshold value. The first thorough investigation of action potential physiology was conducted by Hodgkin and Huxley (1952a,b,c,d), where they examined the squid giant axon. Their description of the action potential involved just two voltage-dependent ion channels: sodium and potassium. The fast inwards sodium current is responsible for the rapid depolarisation at spike onset and the delayed repolarisation is due to the outwards potassium current (Figure 1.5). However, across mammalian species there are more than a dozen voltage-gated sodium-channel types involved in the action potential, along with calcium- and hyperpolarisation-activated currents (Bean 2007).

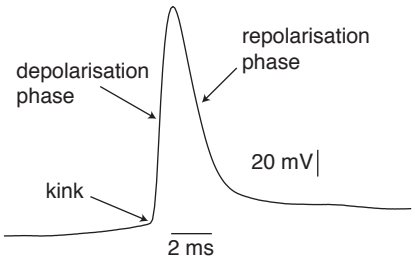

Figure 1.5: Action potential physiology of a thick-tufted layer 5 pyramidal cell from the somatosensory cortex of a juvenile rat, recorded during naturalistic *in vivo*-like stimuli (see Experimental Methods).

1.2.1 Action Potential Initiation

Action potentials are initiated at the axon initial segment 30-60 μm from the soma. Once initiated they propagate along the axon towards post-synaptic neurons, as well as back towards the soma (Stuart *et al.* 1997; Palmer and Stuart 2006; Shu *et al.* 2007a), which is the typical recording site during whole-cell patch-clamp experiments. The somatic voltage displays a 'kink', or rapid depolarisation at spike-initiation (Figure 1.5), the voltage value of which is commonly taken as the initiation threshold of that action potential (Sekerli *et al.* 2004). At the site of initiation the membrane potential is smooth at spike onset, with the 'kink' in somatic voltage due to action potential backpropogation from the axon initial segment (Yu *et al.* 2008).

The spike-initiation threshold is highly variable (Azouz and Gray 2000, 2003; de Polavieja 2005), which could result from a number of sources such as channel noise (White *et al.* 2000), plasticity in the spike initiation zone via ion channel adaptation or structural reorganisation (Grubb *et al.* 2011), or synaptic modulation by axo-axonic cells (Howard *et al.* 2005). Furthermore, the threshold has been shown to strongly correlate with recent voltage history (Azouz and Gray 2000, 2003; Fontaine *et al.* 2014) and time since the last spike (Henze and Buzsáki 2001; Badel *et al.* 2008a,b). It has also been suggested that this variability may be an experimental artefact due to the backpropagation of action potentials from the spike initiation zone to the measurement location at the soma (Yu *et al.* 2008).

1.3 Mathematical Models of Neurons

Mathematical modelling provides a tool for understanding the mechanisms by which neurons encode information, from the single cell to network level. Neuron models are based on Kirchhoff's laws of electrical circuit theory and vary in complexity from one variable ordinary differential equations describing the timings of action potentials, to multi-variable and multi-dimensional partial differential equations describing the membrane potential across the full spatial extent of the neuron.

The complexity of a model depends on the question being asked. Complex models can capture a multitude of ion-channel dynamics and cell behaviours (Hines and Carnevale 1997). They can be used to elucidate intricate mechanisms such as how the cell's dendritic structure affects its output (Hay *et al.* 2011, 2013), the mechanisms underlying spike-threshold variability (Naundorf *et al.* 2006; McCormick *et al.* 2007; Shu *et al.* 2007a), or the temperature dependence of action potential efficiency (Yu *et al.* 2012). However, models such as this are difficult to reliably fit to experimental results due to their inherent non-identifiability.

On the other hand, whilst simple models do not incorporate the full biophysical realism of more complex models, they do not suffer the same overfitting problems and can be more readily incorporated into network models. Furthermore, simple models can be extended to investigate specific cellular properties such as synaptic filtering (Brunel and Hakim 1999), synaptic dynamics (Tsodyks *et al.* 1998), voltage-gated or calcium-gated conductances (Izhikevich 2003; Richardson 2009), and spike-frequency adaptation (Schwalger *et al.* 2010).

In the simplest case the cell is modelled as an RC circuit with a capacitor representing the cell membrane, resistors representing ion channels, and batteries representing the ionic reversal potentials (Figure 1.6). Each additional ionic channel or input current included in the model is then added to the circuit in parallel. The potential difference across the membrane $V(t)$ is governed by

$$C\frac{\mathrm{d}V}{\mathrm{d}t} + I_{\mathrm{ion}} = I_{\mathrm{in}}, \tag{1.1}$$

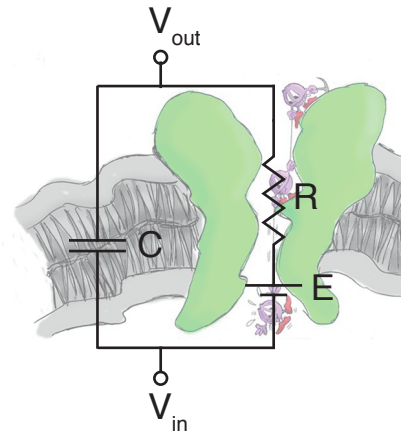

Figure 1.6: A simple neuron model is an RC circuit.

where C is the membrane capacitance; I_{ion} the ionic current, which is the sum of currents from all the ion channels in the model; and I_{in} is any input into the cell, which could be synaptic current or current injected during an experiment.

1.3.1 Continuous Models

Continuous models are biophysically detailed neuron models that aim to capture the full dynamics of both the sub-threshold behaviour and action potential, and are used in complex simulations (Hines and Carnevale 1997). They are characterised by ionic currents with time dependent conductances describing the underlying channel dynamics. These ionic currents take the general form

$$I_{\text{ion}}(t, V(t)) = \sum_i g_i(t)(V(t) - E_i), \tag{1.2}$$

where E_i is the ionic reversal potential of ion i and $g_i(t)$ the channel conductance, which takes the general form

$$g_i(t) = \bar{g}_i \prod_k x_{ik}^{j_k}(t), \tag{1.3}$$

where $\bar{g}_i$ is the maximal channel conductance, $x_{ik}(t)$ the k^{th} gating variable of channel i, taking a value between zero (closed) and one (open), and j_k the number of

gates of type k. The gating variable follows the dynamics

$$\tau_{x_{ik}}(V)\frac{\mathrm{d}x_{ik}}{\mathrm{d}t} = x_{ik\infty}(V) - x_{ik}, \tag{1.4}$$

where $x_{ik\infty}(V)$ is the steady-state gate state and $\tau_{x_{ik}}(V)$ is the gate time constant, which are defined by

$$x_{ik\infty}(V) = \frac{\alpha_{ik}(V)}{\alpha_{ik}(V) + \beta_{ik}(V)}, \tag{1.5}$$

$$\tau_{x_{ik}}(V) = \frac{1}{\alpha_{ik}(V) + \beta_{ik}(V)} \tag{1.6}$$

respectively, where $\alpha_{ik}(V)$ and $\beta_{ik}(V)$ are the opening and closing rates of gate k in channel i, respectively. The form of $\alpha_{ik}(V)$ and $\beta_{ik}(V)$ are specific to each gating variable, but are typically exponential or sigmoidal functions.

Hodgkin-Huxley Model

The Hodgkin-Huxley (HH) model (Hodgkin and Huxley 1952a,b,c,d) of the squid giant axon is probably the most important model in modern neuroscience as it was the first to describe the ion-channel dynamics underlying an action potential. The general principles determined by Hodgkin and Huxley have formed the basis of the majority of neuron models used today, although there has been some recent debate into the validity of this model for cortical neurons (Naundorf *et al.* 2006; McCormick *et al.* 2007).

Hodgkin and Huxley determined that there are three major conductances responsible for the sub-threshold and action potential dynamics of the action potential: leak conductance, due to passive ion channels, sodium conductance, and potassium conductance. The membrane potential can then be described by equation (1.1) and the ionic current given by

$$I_{\mathrm{ion}} = g_{\mathrm{L}}(V - E_{\mathrm{L}}) + \bar{g}_{\mathrm{Na}}m^3h(V - E_{\mathrm{Na}}) + \bar{g}_{\mathrm{K}}n^4(V - E_{\mathrm{K}}), \tag{1.7}$$

where the gating variables m, h, and n, governed by equations of the form of equa-

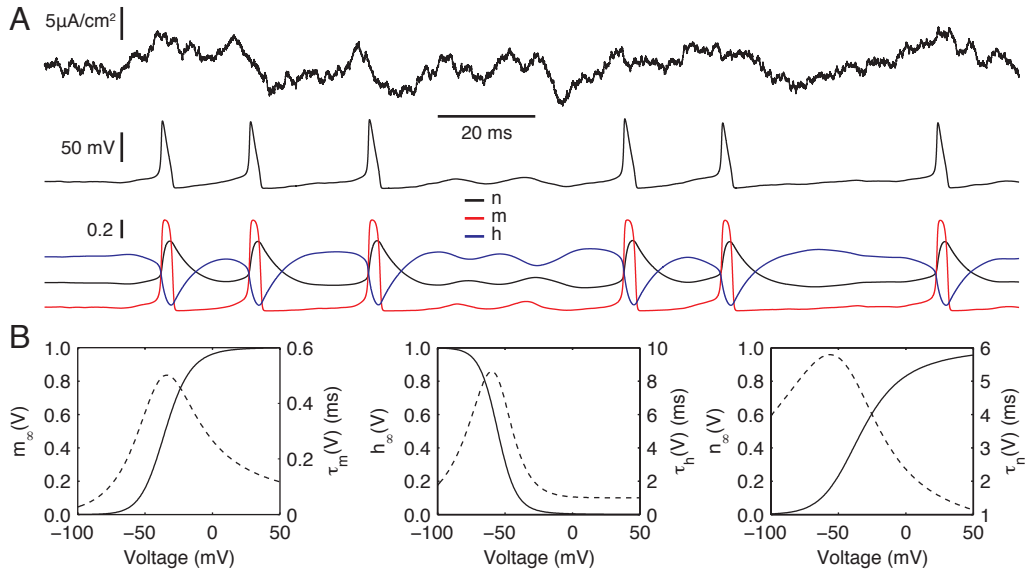

Figure 1.7: Voltage response and channel gating variable dynamics of the Hodgkin-Huxley model. **A** Response of the membrane potential (middle) and gating variables (bottom) to a coloured noise current stimuli (top). **B** Steady-state channel states (left axes, solid lines) and time constants (right axes, dashed lines) of the three gating variables in the Model. Parameters used to generate this figure are given in Table 1.1.

tion (1.4), are responsible for the activation and deactivation of sodium channels and the activation of potassium channels, respectively; g_{L} is the leak conductance, $\bar{g}_{\mathrm{Na}}$ and $\bar{g}_{\mathrm{K}}$ the maximal sodium and potassium conductances, respectively; and E_{L}, E_{Na}, and E_{K} the leak, sodium, and potassium reversal potentials, respectively.

Figure 1.7A illustrates the dynamics of the membrane potential (middle) and gating variables (bottom) in response to a fluctuating current input (top). The action potentials are wider than those of neocortical pyramidal cells (*cf.* Figure 1.5) and are followed by a strong afterhyperpolarization (AHP) where the membrane potential drops to 10 mV below rest. The gating variables m, h, and n follow the dynamics of equation (1.4), with voltage-dependent steady-state channel states and time constants as shown in Figure 1.7B. Parameters used to generate Figure 1.7 are given in Table 1.1.

Simplified Continuous Models

The HH model of the action potential seeded extensive development in computational neuron modelling. Models based on the work of Hodgkin and Huxley display features such as reduced dimensionality (Gerstner and Kistler 2002), additional con-

Table 1.1: Parameters for the Hodgkin-Huxley model.

α_m	$\frac{(25-V)/10}{e^{(25-V)/10}-1}$	g_{L}	0.3 μS/cm^2
β_m	$4e^{-V/18}$	E_{L}	-54.4 mV
α_h	$0.07e^{-V/20}$	g_{Na}	120 μS/cm^2
β_h	$\frac{1}{1+e^{(30-V)/10}}$	E_{Na}	50 mV
α_n	$0.1\frac{(10-V)/10}{e^{(10-V)/10}-1}$	g_K	36 μS/cm^2
β_n	$0.125e^{-V/80}$	E_{K}	-77 mV

ductances (Izhikevich 2007), more cell-type specificity (Pospischil *et al.* 2008), or multiple cell compartments (Sterratt *et al.* 2011). Three such models shall be discussed in this section.

One of the first and perhaps most well studied simplified HH-type neuron models is the FitzHugh-Nagumo (FN) model. First suggested by FitzHugh (1961), the dynamics of the model are described by a two-dimensional van der Pol-like system comprising a voltage-like excitable variable V and a refractory variable W:

$$\frac{\mathrm{d}V}{\mathrm{d}t} = V - \frac{V^3}{3} - W + I, \tag{1.8a}$$

$$\frac{\mathrm{d}W}{\mathrm{d}t} = 0.08(V + 0.7 - 0.8W), \tag{1.8b}$$

where I is the input to the system. The equivalent circuit was formulated by Nagumo *et al.* (1962, Figure 1.8A), which adds a tunnel diode and inductor to the basic neural circuit shown in Figure 1.6.

Although the HH model is more biophysically realistic the FN model captures the two key elements of the system: excitability and refractoriness. Furthermore, the entire phase plane can be viewed (Figure 1.8B), rather than projections of four-dimensional phase trajectories as in the HH model; the example phase trajectory in Figure 1.8B (green) illustrates the excitability and refractoriness of the FN model. The model explains a number of features observed in the HH model, such as the absence of all-or-nothing action potentials, a consequence of which is that the model does not have a well-defined spike threshold and is related to the absence of a saddle-node bifurcation (FitzHugh 1955); the cessation of repetitive spiking as the

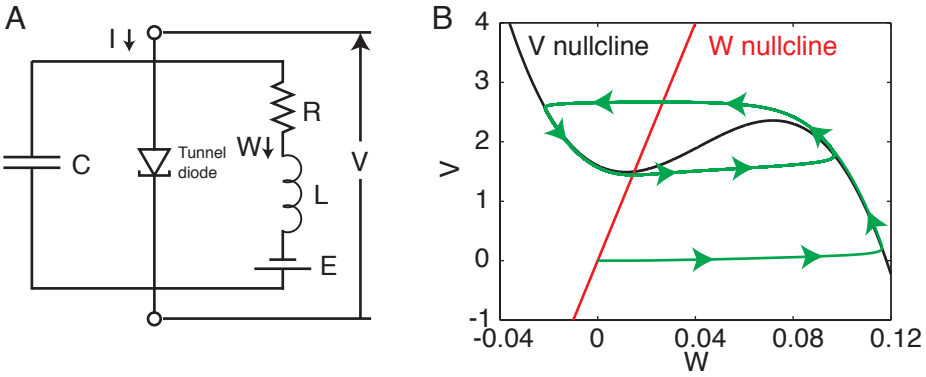

Figure 1.8: The FitzHugh-Nagumo model is a simplification of the Hodgkin-Huxley model introduced by FitzHugh (1961). **A** The model can be described by the circuit suggested by Nagumo *et al.* (1962), consisting of a capacitor (C), tunnel diode, resistor (R), inductor (L), battery (E), and input current I. **B** The V (black) and W (red) nullclines of the system, along with an example trajectory (green).

stimulus amplitude increases, caused by an upwards shift in the V nullcline; and post-inhibitory rebound spikes, caused by a left-hand shift in the stable fixed point during a negative stimulus.

The Morris-Lecar (ML) model (Morris and Lecar 1981) is another widely used continuous model of an excitable system; originally applied to the barnacle giant muscle fibre, it has become a popular choice in computational neuroscience (Sterratt *et al.* 2011) and has been applied to other systems such as lobster stomatogastric ganglion neurons (Skinner *et al.* 1993) and mammalian spinal sensory neurons (Prescott *et al.* 2008). The model is a two dimensional system comprising a passive leak conductance and two non-inactivating voltage-dependent conductances: an excitatory calcium conductance and a delayed rectifying potassium conductance. Furthermore, the ML model can display a range of firing behaviours, depending on the parameter values.

Finally, the Wang-Buzsáki (WB) model is a simplification of the Hodgkin-Huxley model that was originally applied to hippocampal interneurons (Wang and Buzsáki 1996). The model approximates the spike generating fast activation of sodium channels in the HH model [equation (1.7)] as instantaneous. The ionic current is then given by

$$I_{\text{ion}} = g_{\text{L}}(V - E_{\text{L}}) + \bar{g}_{\text{Na}} m_{\infty}^3 h (V - E_{\text{Na}}) + \bar{g}_{\text{K}} n^4 (V - E_{\text{K}}), \tag{1.9}$$

where the fast sodium-channel activation term is given by

$$m_\infty(V) = \frac{\alpha_m(V)}{\alpha_m(V) + \beta_m(V)}, \tag{1.10}$$

where $\alpha_m(V)$ and $\beta_m(V)$ are the voltage-dependent channel opening and closing rates, respectively. This is a valid approximation due to the magnitude of τ_m, which is an order of magnitude smaller than the other gating variable time constants (Figure 1.7, dashed lines). The model has been incorporated into network models to investigate the mechanism underlying gamma oscillations in the hippocampus (Buzsáki and Wang 2012), and has also been used to validate fitting methods for reduced neuron models (Badel *et al.* 2008b). In Chapter 8 I will extended this model to explore the effect that slow sodium-channel inactivation has on spike threshold variability.

1.3.2 Discontinuous Integrate-and-Fire Models

Integrate-and-fire (IF) neurons are models that, rather than explicitly describing the dynamics of the action potential, register a spike when the membrane potential reaches a pre-defined threshold V_{th} before being reset to a value V_{re} a short time later (Figure 1.9). This gross simplification of the continuous models discussed in Section 1.3.1 is popular due the mathematical tractability of these models. Indeed, removal of the action potential results in greatly reduced dimensionality; the simplest IF models reduce the neuron to an electrical circuit that is completely described by its membrane potential (for review see Burkitt 2006a,b). However, this approximation is justified if one is interested only in the precise timing of action potentials, which is of central importance to neural coding (Markram *et al.* 2011). Furthermore, with the addition of simple refractory mechanisms IF models can faithfully reproduce experimental perisomatic voltage recordings from a variety of cell classes (Jolivet *et al.* 2006a; Badel *et al.* 2008a; Jolivet *et al.* 2008; Gerstner and Naud 2009; Kobayashi *et al.* 2009; Rossant *et al.* 2011; Mensi *et al.* 2012).

The very first integrate-and-fire neuron model was the perfect integrator formulated by Lapicque (1907), which describes the neuron as a capacitor being charged

by an external current $I_{\text{in}}(t)$:

$$C\frac{\mathrm{d}V}{\mathrm{d}t} = I_{\text{in}}(t), \tag{1.11}$$

where C is the membrane capacitance and V the membrane potential. Lapicque extended this model to be more physiologically realistic by introducing an ohmic term representing the sub-threshold passive membrane response, the leak current, given by the first term in equation (1.7) above. This can be incorporated into equation (1.11) to give the leaky integrate-and-fire (LIF) model:

$$C\frac{\mathrm{d}V}{\mathrm{d}t} = g_L(E_L - V) + I_{\text{in}}(t), \tag{1.12}$$

where g_{L} is the leak conductance and $\tau_L = C/g_L$ is the membrane time constant. The LIF has been used extensively to study the response of a single neuron by Lapicque and others (Burkitt 2006a), has been extended to include more complicated cell features such as an explicit spike generating term (Fourcaud-Trocmé *et al.* 2003; Izhikevich 2010) or a variable spike threshold (Chacron *et al.* 2003; Lindner and Longtin 2005), and has also been incorporated into network models (Brunel and Hakim 1999; Burkitt 2006b; Câteau and Reyes 2006; Ledoux and Brunel 2011).

Exponential Integrate-and-Fire Model

The natural extension of the LIF is to add terms that describe specific aspects of the spike dynamics. These equations take the form

$$\frac{\mathrm{d}V}{\mathrm{d}t} = F(V) + \frac{I_{\text{in}}(t)}{C}, \tag{1.13}$$

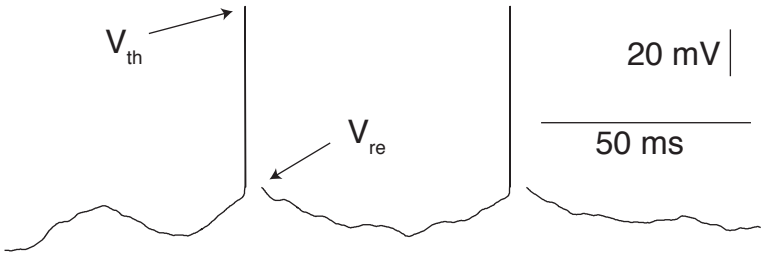

Figure 1.9: Integrate-and-fire models do not model the full dynamics of the action potential, but define a threshold V_{th} after which the membrane potential is reset to a value V_{re} before the integration continues.

where $F(V)$ is in general a non-linear forcing function of V; these are referred to as non-linear IF (NIF) models. One important NIF is the exponential IF (EIF) model (Fourcaud-Trocmé *et al.* 2003), which incorporates an exponential term describing the fast activation of voltage-gated sodium channels responsible for the initial sharp rise in membrane potential at spike onset. The forcing function is then given by

$$F(V) = \frac{1}{\tau}\left(E - V + \Delta_T \exp\left(\frac{V - V_T}{\Delta_T}\right)\right), \tag{1.14}$$

where τ is the membrane time constant, E the membrane resting potential, Δ_T the spike sharpness, and V_T the spike-onset threshold. Although originally derived from the WB model (Wang and Buzsáki 1996), it has since been experimentally verified for thick-tufted layer 5 pyramidal cells (Badel *et al.* 2008a), GABAergic fast-spiking interneurons (Badel *et al.* 2008b), and striatal medium spiny neurons (Dorst 2013). Furthermore, Badel *et al.* (2008a,b) extended the model to include spike-triggered dynamics of the four parameters in equation (1.14), yielding the refractory EIF (rEIF) model. This extended model proved a more accurate fit to the spike-timing and sub-threshold voltage response of thick-tufted layer 5 pyramidal cells over the standard EIF model.

1.4 Thesis Outline

This thesis focuses on constraining and extending reduced models of neocortical pyramidal neurons. I address two important challenges in computational neuroscience, namely experimental verification of model parameters and furthering our understanding of the biophysical processes underlying post-spike refractory mechanisms. Addressing these two challenges is crucial for understanding how neurons interact at the network level; the large scale network models required for this are only as relevant as the cells of which they comprise.

In Chapter 2 I describe detailed methods of the electrophysiology and pharmacology experiments I performed, and imaging techniques I used in this work. Chapter 3 gives a background to the theoretical methods I used, including detailed

descriptions of all model formulations, model fitting and simulation protocols, model performance measure calculations, and full derivations of analytical results.

In Chapter 4 I quantify the somatic electrophysiology of pyramidal cells in neocortical layers 2/3-5 using a combination of square-pulse and fluctuating *in vivo*-like stimuli. Many parameters are measured using the dynamic I-V method (Badel *et al.* 2008a,b), which fits a non-linear function to the instantaneous current-voltage relationship of the cell. This fit is an empirical measurement of the forcing function for a reduced neuron model, without an *a priori* assumption of model form. I found that each cell class investigated fit a forcing function of the EIF form, extending the scope of applicability of this model. Furthermore, I provide a MATLAB toolbox to perform this fitting procedure in Appendix A. I discuss alternative models and fitting methods, finding that the rEIF model fit using the dynamic I-V method performs comparably or better despite no attempt at optimising the model. I next investigate the post-spike parameter dynamics of the conductance, spike-onset threshold, and resting potential. I give particular focus to the latter, finding that it is mediated by I_{h} channels. Finally, I quantify the marginal parameter distributions and investigate between-class differences, noting that the major differences appear to be in the steady-state parameters: the sub-threshold parameters; cell excitability; and action potential shape, and also the refractory dynamics of the resting potential.

In Chapter 5 I conduct a more in-depth analysis of the sources of variability in the dataset extracted in Chapter 4. I find that, in agreement with pairwise significance tests, principal component analysis suggests the key determinants of cell class are the steady-state parameters, with the post-spike sag in the resting potential dynamics also contributing significantly to the overall variability. Using a combination of Gaussian mixture models, linear discriminant analysis, and random decision forests I find that layer 4 and slender-tufted layer 5 pyramidal cells appear almost indistinguishable in their electrophysiology. This is surprising given they are located at different cortical depths (Thomson and Lamy 2007), have distinct morphologies (Staiger 2004; Oberlaender *et al.* 2012), and receive synaptic input from different origins (de Kock *et al.* 2007). I conclude this chapter by examining the variance and covariance structure of parameter space, finding non-trivial correlations relating to

the I_{h} current. I further provide an algorithm to generate EIF and rEIF model parameter sets that respect this empirical covariance structure and the marginal distributions measured in Chapter 4. This is a novel tool for exploring the effects of heterogeneities in neocortical network models. A MATLAB implementation of these algorithms are provided in Appendices B and C, and the full experimental dataset has been made available elsewhere.

The focus of Chapter 6 is on the refractory nature of the spike-onset threshold and the response of populations of neurons displaying these dynamics. I begin the chapter by quantifying the degree to which the threshold accumulates over multiple closely spaced action potentials and attempt to use this to extend the rEIF model. However, after incorporating this threshold accumulation only a very small performance improvement was seen, suggesting the benefit from including this more physiologically accurate behaviour is not worth the additional mathematical complexity. I also investigate a two-variable EIF model that includes only the post-spike threshold dynamics, ignoring the rEIF model's addition of a dynamic conductance and resting potential. Although this model performed worse than the rEIF model it was a significant improvement over the standard EIF model and has the advantage of being simple to analyse yet remaining experimentally relevant. Indeed, in the case of equal membrane and threshold timescales the model reduces to the standard EIF model with a lower reset. In pyramidal cells across the neocortex I demonstrate that the ratio of these timescales is close to one, suggesting that this is a physiologically realistic approximation.

In Chapter 7 I continue investigating the two-variable EIF model introduced in the previous chapter. I take a perturbative approach to analyse populations of these neuron models using a previously introduced threshold integration method (Richardson 2007), extending previous work on networks of LIF models with a dynamic threshold to a non-small spike-triggered threshold jump (Lindner and Longtin 2005). This analysis captures the population response across the entire physiological range of the membrane to threshold timescale ratio.

Chapter 8 investigates slow sodium-channel inactivation, a possible mechanism underlying the observed post-spike threshold behaviour. After incorporating this

mechanism into an existing continuous spiking neuron model (Wang and Buzsáki 1996) and the EIF model I show that the inclusion of this gating variable implies a large post-spike jump in spike-onset threshold followed by a rapid decay into a slower, mono-exponential decay back to baseline over tens of milliseconds. However, this form is a poor fit to the response measured from thick-tufted layer 5 pyramidal cells, which display a mono-exponential decay, suggesting either that this mechanism is not responsible for the observed dynamics or is supplemented by additional conductances.

Finally, in Chapter 9 I conclude by summarising the key results of this thesis and discussing their wider implications, suggesting possible future directions for extending this research.

Chapter 2

Experimental Methods

2.1 Preparation of Neocortical Slices

I prepared parasagittal slices of somatosensory neocortex (300 μm) from male Wistar rats (a strain of outbred, wild type albino rats), at postnatal day 16-18 (Kerr *et al.* 2013). Rats were kept on a 12 hour light-dark cycle and I made slices 90 minutes after entering the light cycle. In accordance with the UK Animals (Scientific Procedures) Act (1986), I euthanised the rats by cervical dislocation followed by decapitation. I rapidly removed the brain, cut down the midline and stuck down the two hemispheres. I angled the brain at 15° so that I could obtain planar slices with the dendritic structure of the excitatory neurons intact. To cut slices I used a Microm HM 650 V micro-slicer (Carl Zeiss) with the brain immersed in cold (2-4°C) high Mg^{2+} low Ca^{2+} artificial cerebral spinal fluid (aCSF) consisting of 127 mM NaCl, 1.18 mM KH_2PO_4, 2.14 mM KCl, 26 mM $NaHCO_3$, 8 mM $MgCl_2$, 0.5 mM $CaCl_2$, and 10 mM glucose. I incubated the slices at 34°C for 1 hour in standard aCSF (1 mM Mg^{2+} and 2 mM $CaCl_2$) and then stored them at room temperature for 1-6 hours until they were used.

2.2 Intracellular Recording

I transferred a slice to the recording chamber and perfused at 2 ml/min with aCSF at 32°C. I visualised the slices using an Olympus BX51W1 microscope with IR-DIC

optics and a Hitachi CCD camera (Scientifica, Bedford, UK). I took single or double whole-cell current-clamp recordings from unconnected cells with patch pipettes (5-8 mΩ) manufactured from thick walled glass (Harvard Apparatus Edenbridge UK) containing 135 mM k-gluconoate, 7 mM NaCl, 10 mM HEPES, 0.5 mM EGTA, 2 mM ATP, 0.3 mM GTP, and 10 mM phosphocreatine (290 mOSM, pH 7.2). I obtained voltage recordings using an Axon Multiclamp 700B amplifier and digitised at 20 Khz with a Digidata 1440A (Molecular Devices, Sunnyvale, CA). The liquid junction potential was 10 mV and was not corrected for. I identified pyramidal neurons based on their somata size, and the location of layers 2/3, 4, and 5 by the distance from the pia. During recording, I labelled neurons either with the fluorescent dye Alexa Fluor® 488 hydrazide (12.5 mM, Life Technologies, Paisley, UK) or with biocytin (1 mg/mL, Sigma-Aldrich, Dorset, UK) to allow confirmation of the cell type and to ensure an intact apical dendrite.

I stimulated cells with square-pulse currents (Figure 2.1A) and naturalistic *in vivo*-like currents (Figure 2.1B), during which the typical access resistance was 9-13 MΩ. The form of the naturalistic currents I injected consisted of two summed Ornstein-Uhlenbeck processes with time constants $\tau_{\text{fast}} = 3$ ms and $\tau_{\text{slow}} = 10$ ms, representing α-Amino-3-hydroxy-5-methyl-4-isoxazolepropionic acid (AMPA) and γ-Aminobutyric acid A (GABA_A) conductances, respectively, as used by Badel *et al.* (2008a,b). I used two sets of variances, a low ($\sigma_{\text{fast}} = 0.18 = \sigma_{\text{slow}}$) and a high ($\sigma_{\text{fast}} = 0.36$, $\sigma_{\text{slow}} = 0.25$), along with two DC biases (0.5 and 1), giving four distinct current traces that were used for each recording. I applied a multiplicative gain factor in the range 200-2000 pA to each current to give a resulting firing rate of 5-15 Hz.

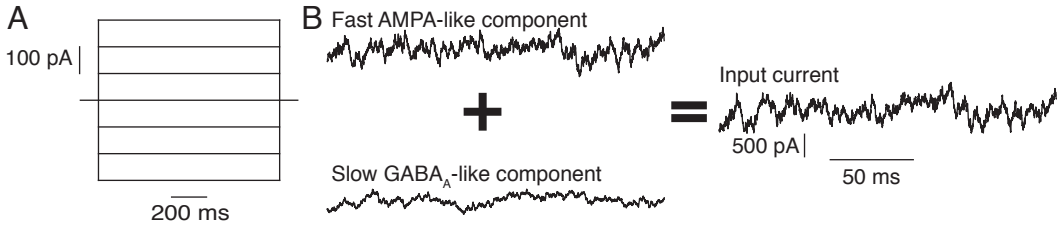

Figure 2.1: Example current stimuli used in this study. **A** Square pulse current stimulus. **B** Naturalistic *in vivo*-like current stimulus comprising fast AMPA-like and slow GABA_A-like Ornstein-Uhlenbeck processes.

I recorded from a total of 156 cells across four pyramidal cell classes: layer 2/3 (L2/3, $n = 35$), layer 4 (L4, $n = 37$), slender-tufted layer 5 (SL5, $n = 33$), and thick-tufted layer 5 (TL5, $n = 51$). For each of these cells I recorded the response to a series of square-pulse currents followed by the four naturalistic stimuli described above. One or two of the four naturalistic stimuli was used for model fitting with the remaining recordings used to test the quality of the model fits (see Sections 3.2 and 3.5 for details of the model fitting procedures). After these initial recordings I waited 10 min before repeating these protocols so as I could quantify the cell's intrinsic reliability; neurons are inherently stochastic and so multiple instances of the same current stimulus will evoke different spike trains. Furthermore, whole-cell patch-clamping can produce errors inherent to the technique such as baseline drift or an increasing access resistance, so by repeating the stimuli I could ensure the recording was stable.

To asses whether or not a recording was unreliable I calculated a previously defined coincidence measure (Kistler *et al.* 1997; Jolivet *et al.* 2004; Badel *et al.* 2008a) given by

$$\Gamma = \frac{N_{\text{coinc}} - \langle N_{\text{coinc}} \rangle}{1/2(N_1 + N_2)} \frac{1}{\mathcal{N}}, \tag{2.1}$$

where N_1 is the number of spikes in the reference spike train; N_2 is the number of spikes in the spike train for comparison; N_{coinc} is the number of coincidence spike occurrences between the two spike trains with a precision Δ, which in this case was set to 5 ms; $\langle N_{\text{coinc}} \rangle = 2f\Delta N_1$ is the number of expected coincidences generated by a homogeneous Poisson process with firing rate f, the rate of the reference spike train; and $\mathcal{N} = 1 - 2f\Delta$ is a normalising factor so that $\Gamma = 1$ corresponds to an exactly coincident spike train.

I calculated Γ_{rep}, comparing the repeat recording to the first, for the naturalistic current stimulus used for model fitting. I then set a previously established threshold (Badel *et al.* 2008a,b) of 0.75, a Γ_{rep} lower than which implies that the cell and/or recording were unreliable. This criterion was failed by 13% of the recordings, leaving a population of 136 cells comprising 31 L2/3, 29 L4, 29 SL5, and 47 TL5 pyramidal cells.

2.3 Histology and Confocal Microscopy

During recording I filled the cells with either the fluorescent dye Alexa Fluor® 488 hydrazide (12.5 mM, Life Technologies, Paisley, UK) or biocytin (1 mg/mL, Sigma-Aldrich, Dorset, UK) to allow post-recording identification. Post-recording I carefully removed the patch pipettes from the neuron so as to not to cause damage. On removal from the bath I immediately transferred the slice to a 4% paraformaldehyde/phosphate buffer solution (PBS, pH 7.3) and incubated overnight at ~ 4°C. I throughly washed slices containing fluorescently labelled neurons in PBS (5×5 min) and tris buffer solution (TBS, pH 7.3, 3×5 min). I then mounted these slices on a transparent microscope slide in a 50% glycerol/DI water solution and imaged using a Leica SP5 cofocal microscope (Figure 1.3A).

For biocytin filled neurons, I incubated slices overnight at 4°C in 1% triton/TBS solution to permeabalise the membrane. I then washed the slices several times in TBS (3×5 min), followed by incubating them at room temperature in 3% H_2O_2/methanol whilst agitating to remove endogenous peroxidase activity. I then washed the slices once in 1% triton/TBS solution followed by several washes in TBS (3×5 min) and incubated in ABC solution (mixed as per manufacturer's instructions) for 2 hours whilst agitating. I then washed the slices again in TBS (3×5 min) prior to application of the DAB reaction mixture. I quenched the reaction when the dendritic structure of the cells became visible under visual inspection using TBS. I dehydrated the slices using increasingly concentrated ethanol/H_2O solutions, cleared them using methyl salicitate, and mounted them on microscope slides for visual inspection (Figure 2.2).

2.4 I_h Channel Blocking Experiments.

To investigate the effect of I_h channels on the equilibrium potential I made whole-cell patch-clamp recordings from eight cells, four from Wistar rats and four from Sprague-Dawley rats. Both of these rats strains are wild type, outbred albino rats, the data from which were indistinguishable and so was pooled. I applied the same combination of square-pulse and naturalistic stimuli as outlined above (Figure 2.1)

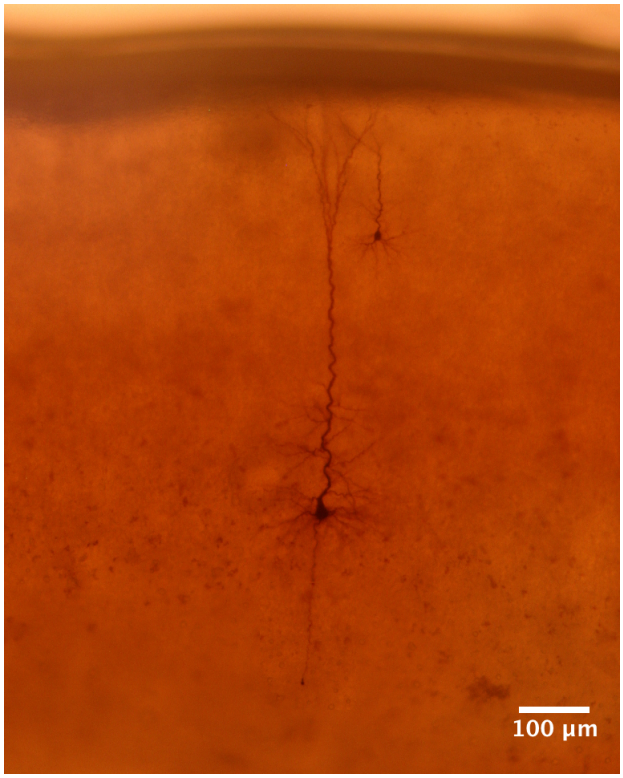

Figure 2.2: Example thick-tufted layer 5 (left) and layer 2/3 (right) pyramidal cells filled with biocytin and imaged.

in control then after applying ZD7288 (25 μM, Sigma-Aldrich, Dorset, UK). This has been shown to block I_{h} channel conductances at this concentration (Harris and Constanti 1995). The effects of ZD7288 reached steady state after approximately 10 min, after which time I could perform the non-control experiments.

Chapter 3

Theoretical Background

3.1 Electrode Filter

Due to the high frequency of the naturalistic stimuli described in Section 2.2, standard techniques compensating for the filtering properties of the electrode are not sufficient. An active electrode compensation (AEC) technique has been previously introduced to eliminate this problem (Brette *et al.* 2007, 2008), which has been validated for use with the dynamic *I-V* method (Badel *et al.* 2008a). We assume that the potential across the electrode $V_{\mathrm{el}}(t)$ is a linearly filtered version of the injected current $I(t)$, so can be written as the convolution of $I(t)$ and an unknown electrode filter $f(t)$. The recorded potential $V_{\mathrm{rec}}(t)$ is then the sum of $V_{\mathrm{el}}(t)$ and the true membrane potential $V(t)$, given by

$$V_{\mathrm{rec}}(t) = V(t) + V_{\mathrm{el}}(t) = V(t) + \int_0^\infty f(s)I(t-s)\mathrm{d}s. \tag{3.1}$$

However, $V(t)$ is filtered by the cell membrane and can thus be written in the form $V(t) = E + \int_0^\infty g(s)I(t-s)\mathrm{d}s$, where $g(s)$ is the membrane filter and E is the resting potential. As such $f(t)$ cannot be determined directly, but we can extract the combined filter $\tilde{f}(s) = f(s) + g(s)$. This can be determined by the minimisation approach taken by Badel *et al.* (2008a). The tail of the resulting filter $\tilde{f}(s)$ can then be fitted with a double exponential, with a long time constant component ($\sim 15\,\mathrm{ms}$) and a short time constant component ($\sim 0.5\,\mathrm{ms}$) corresponding to the membrane

and electrode, respectively. Subtracting the long time constant component then yields the electrode filter, which can then be used to calculate the true membrane potential from equation (3.1).

3.2 Dynamic I-V Method

The dynamic I-V curve method measures the instantaneous current-voltage relationship from the response of the cell to an *in vivo*-like current injection, and is an efficient technique for accurately characterising neuronal parameters (Badel *et al.* 2008a,b). The relationship between the total ionic current I_{ion} and the membrane potential V is defined by the equation

$$I_{\text{ion}}(V,t) = I_{\text{in}}(t) - C\frac{\mathrm{d}V}{\mathrm{d}t}, \tag{3.2}$$

where C is the membrane capacitance and I_{in} is the current injected during whole-cell patch-clamping. The membrane capacitance can be extracted via a previously used variance minimisation technique (Badel *et al.* 2008a,b). We can re-write equation (3.2) in the form

$$\frac{I_{\text{in}}(t)}{C_e} - \frac{\mathrm{d}V}{\mathrm{d}t} = \frac{I_{\text{ion}}(V,t)}{C} + \left(\frac{1}{C_e} - \frac{1}{C}\right) I_{\text{in}}(t), \tag{3.3}$$

where C_e is an estimate of the true capacitance. The variance is then given by

$$\text{Var}\left[\frac{I_{\text{in}}(t)}{C_e} - \frac{\mathrm{d}V}{\mathrm{d}t}\right] = \text{Var}\left[\frac{I_{\text{ion}}(V,t)}{C}\right] + \left(\frac{1}{C_e} - \frac{1}{C}\right)^2 \text{Var}\left[I_{\text{in}}(t)\right], \tag{3.4}$$

the right hand side of which is minimised when $C = C_e$.

Having determined the membrane capacitance we can then calculate the instantaneous current-voltage relationship. The dynamic I-V curve is then defined as

$$I_{\text{d}}(V) = \langle I_{\text{ion}}(V,t)\rangle_{\text{V}}\,, \tag{3.5}$$

the average ionic current as a function of voltage.

One important consequence of the dynamic I-V method is that it validates

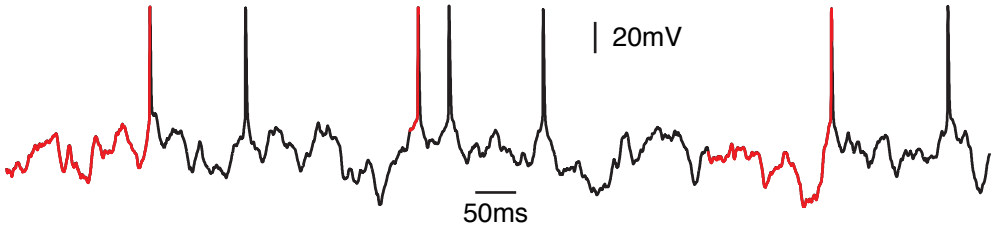

Figure 3.1: The baseline parameter values are extracted from quantifying the dynamic I-V curve after omitting data 200 ms after each action potential peak, leaving the data shown in red. The remaining data is used to quantify the transient post-spike parameter dynamics.

the form of the non-linear term in the exponential integrate-and-fire (EIF) model (Fourcaud-Trocmé *et al.* 2003), given by equation (1.14). The dynamic I-V curve and F are related via $F(V) = -I_{\mathrm{d}}(V)/C$, and so by fitting equation 1.14 to the experimentally determined $I_{\mathrm{d}}(V)$ we can quantify the dynamic I-V curve. Considering first only data in the sub-threshold voltage regime and in the run-up to action potentials, achieved by omitting data points in the 200 ms following each action potential peak (leaving the data shown in red in Figure 3.1), we can then determine baseline values of the four parameters in equation (1.14). This 200 ms window was chosen since any transient spike-triggered parameter dynamics have returned to baseline after this time (Badel *et al.* 2008a,b). Spikes included in this subset of the voltage trace are hereby referred to as isolated spikes.

This method can be used to quantify the spike-triggered response of the parameters in equation (1.14) by fitting the dynamic I-V curve to data from small time slices following each spike (subsets of the black region in Figure 3.1 following an action potential), which shifts on spike initiation and subsequently relaxes back to baseline over a period of tens of milliseconds. The conductance g (calculated from $g = C/\tau$), resting potential, and spike-onset threshold all follow a spike-triggered dynamics that can be well captured by a single- or double-exponential, whereas the spike sharpness follows no specific dynamics. The standard EIF model combined with these spike-triggered parameter dynamics define the refractory EIF (rEIF) model, which has been shown to offer significant improvement over the standard model in capturing the response of thick-tufted layer 5 pyramidal cells and GABAergic fast-spiking interneurons *in vitro* (Badel *et al.* 2008a,b).

3.3 Additional Cell Parameters

Three further parameters were extracted from the naturalistic currents used for the dynamic I-V method. The action potential amplitude, duration, and maximal rate of rise were calculated for each isolated spike in the same noisy current injection used to fit the dynamic I-V curve and averaged to give values for that cell. Amplitude was defined as the distance between the spike-initiation threshold for that spike, calculated using the second derivative method (Sekerli *et al.* 2004), and the maximum voltage reached; duration as the width at half maximum; and maximal rate of rise as the maximum first voltage derivative between spike-initiation threshold and spike peak.

Three parameters were extracted from step current injections. The input resistance R_{in} was calculated from the gradient of the current voltage relationship for two to three successive step current injections around rest, measured from the mean voltage of the last 200 ms of each 1 sec current step. The input conductance G_{in} was calculated as the inverse of R_{in}. The sag percentage S was defined as the difference between the minimum voltage during a hyperpolarising current injection and the steady voltage, again measured from the last 200 ms of a 1 sec current step, as a percentage of the steady voltage compared to rest (Figure 4.1C).

Finally, two hybrid parameters describing the cell's excitability were measured: the distance to spike-onset threshold from rest $V_{\text{T}} - E$ and the spike initiation current, defined by $I_{\text{spike}} = (V_{\text{T}} - E)/R_{\text{in}}$.

3.4 Simulation of the rEIF Model

To test the performance of the dynamic I-V method I simulated the rEIF model in response to novel stimuli not used for fitting. The rEIF model is defined by

$$\frac{\mathrm{d}V}{\mathrm{d}t} = \frac{1}{\tau}\left(E - V + \Delta_T \exp\left(\frac{V - V_T}{\Delta_T}\right)\right) + \frac{I_{\text{in}}}{C}, \tag{3.6}$$

where τ is the membrane time constant, E the resting potential, Δ_{T} the spike sharpness, and V_{T} the spike-onset threshold, combined with the post-spike parameter

dynamics of g, E, and V_{T}. Note that in this work I discuss the refractory dynamics of the membrane conductance g rather than the membrane time constant τ, where $g = C/\tau$. This is because the refractory dynamics of τ are not of a simple form consistent with the other transient parameters, but rather it is $1/\tau$ that follows a mono-exponential. Therefore the dynamics of g, which is proportional to $1/\tau$, is a more intuitive quantity to discuss.

The rEIF model, along with all other integrate-and-fire models in this work, was simulated using a forward Euler scheme with a time step of 50 μs, corresponding to the acquisition rate of the experimental recordings (20 kHz). Due to the exponential spike-generating term, action potentials appear as a rapid rise in membrane potential, and so a spike was defined when the membrane potential reached 30 mV. The model does not explicitly include the downswing of the action potential and so the integration was stopped for a refractory period of t_{ref}. On resumption of the integration the parameters g, E, and V_{T} were increased to their post-spike jump values and subsequently followed their fixed post-spike dynamics, given by

$$g = g_0 + g_1 e^{-(t-t_{\mathrm{ref}})/\tau_{\mathrm{g}}}, \tag{3.7}$$

$$E = E_0 - E_1 e^{-(t-t_{\mathrm{ref}})/\tau_1} + E_2 e^{-(t-t_{\mathrm{ref}})/\tau_2}, \text{ and} \tag{3.8}$$

$$V_{\mathrm{T}} = V_{\mathrm{T0}} + V_{\mathrm{T1}} e^{-(t-t_{\mathrm{ref}})/\tau_{\mathrm{T}}}, \tag{3.9}$$

respectively, where t is the time since the peak of the previous spike; g_0, E_0, and V_{T0} are baseline values calculated from the pre-spike dynamic I-V curve; g_1, E_1, E_2, and V_{T1} are constant exponential coefficients; and τ_{g}, τ_1, τ_2, and τ_{T} are the exponential time constants. Since Δ_{T} has no specific post-spike dynamics it was held constant at its pre-spike value.

On registering a spike the voltage was reset to a value V_{re} before the integration continued. In Chapters 4 and 5 this value was determined from the fluctuating current input(s) used to fit the model. I calculated the average waveform for all isolated spikes, and set V_{re} to the value at time t_{ref} after its peak. This was in general above the pre-spike baseline threshold V_{T0}, and so if t_{ref} was too short then V_{re} was too high for the transient threshold increase to prevent the cell firing

continuously. I found a refractory period of 4 ms long enough to avoid this problem.

In Chapter 6 I compare the rEIF model with the standard EIF model along with two other EIF model variants. Since the standard EIF has no transient parameter dynamics, a reset value more depolarised than threshold would result in continual firing. As such, I set V_{re} to equal to 2 mV less than threshold. I set t_{ref} equal to 2 ms, in part due to a lower reset value allowing a more physiological refractory period - the width on an action potential in neocortical pyramidal cells is approximately 2 ms (Bean 2007) - but also to be consistent with previous work (Richardson 2007; Badel *et al.* 2008a; Richardson 2008; Badel *et al.* 2008b)

3.5 Additional Model Fitting and Simulation Procedures

3.5.1 Spike-response Model

The spike-response model (SRM, Mensi *et al.* 2012) is defined by deterministic sub-threshold dynamics and stochastic spike emission. The sub-threshold dynamics are defined by

$$C\frac{\mathrm{d}V}{\mathrm{d}t} = -g_{\mathrm{L}}(V(t) - E_{\mathrm{L}}) + \sum_{\{\hat{t}_j\}} \eta(t - \hat{t}_j) + I(t), \tag{3.10}$$

where C is the membrane capacitance, g_{L} the leak conductance, E_{L} the resting potential, $I(t)$ the time-dependent input to the cell, and $\eta(t - \hat{t}_j)$ the adaptation current triggered by spike j at time $\hat{t}_j$.

Spike emission in the SRM is stochastic and follows an inhomogeneous point process with conditional firing intensity (i.e. rate parameter) given by

$$\lambda(t|V, V_{\mathrm{T}}) = e^{(V(t) - V_{\mathrm{T}}(t))/\Delta V}, \tag{3.11}$$

where ΔV describes the sharpness of the exponential firing intensity and $V_{\mathrm{T}}(t)$ is the spike threshold, given by

$$V_{\mathrm{T}}(t) = V_0 + \sum_{\{\hat{t}_j\}} \gamma(t - \hat{t}_j), \tag{3.12}$$

where V_0 is the baseline threshold and $\gamma(t-\hat{t}_j)$ describes the spike-triggered threshold dynamics. Both η and γ were expressed as a linear combination of rectangular basis functions. The fitting procedure of the SRM proceeds in two steps. The first is to fit the sub-threshold parameters in equation (3.10) by minimising the sum of the squared difference between the model and experiment of the voltage time derivative away from spikes. The second step is to fit the threshold dynamics given by equations (3.11) and (3.12) by maximising the likelihood of observing the experimental spike train. To implement this procedure I used the MATLAB implementation published by Mensi *et al.* (2012) adapted to accept our experimental data. Since spike generation in this alternative model is stochastic, to quantify the performance of the SRM I simulated the response to each novel current 1000 times, measured the relevant metrics for each simulation, and used their average values for comparison.

3.5.2 Multi-timescale Adaptive Threshold Model

The multi-timescale adaptive threshold (MAT, Kobayashi *et al.* 2009) model has a deterministic sub-threshold behaviour described by a leaky integrator, similar to the SRM but without an adaptation current. This is supplemented by a deterministic spike-triggered threshold described by the sum of three exponentials. The sub-threshold behaviour is described by

$$\tau \frac{\mathrm{d}V}{\mathrm{d}t} = E - V(t) + RI(t), \tag{3.13}$$

where, τ is the membrane time constant, E the resting potential, and R the input resistance. These parameters were fit by minimising the sum of the squared difference between the model and experimental voltage traces away from spikes. The spike threshold was of the form

$$\theta(t) = \omega + \sum_{\{t_k\}} \sum_{j=1}^{3} \alpha_j e^{-t/\tau_j}, \tag{3.14}$$

where ω is the baseline threshold, α_j the exponential pre-factors and τ_j the decay time constants. The three time constants were held constant at 10 ms, 50 ms, and

200 ms [referred to as the MAT(3) model by Kobayashi *et al.* (2009)], and the remaining four parameters were chosen to maximise the spike train coincidence measure, defined in equation (2.1), with the experimental trace. As no explicit algorithm was described by Kobayashi *et al.* I implemented custom MATLAB scripts utilising the statistics and global optimisation toolboxes.

3.5.3 Adaptive Exponential Integrate-and-Fire Model

The adaptive exponential integrate-and-fire (AdEx, Brette and Gerstner 2005) model is a two-dimensional extension to the standard EIF that has the addition of an adaptation current. The model is defined by

$$C\frac{\mathrm{d}V}{\mathrm{d}t} = -g_{\mathrm{L}}(V(t) - E_{\mathrm{L}}) + g_{\mathrm{L}}\Delta_{\mathrm{T}}e^{(V(t)-V_{\mathrm{T}})/\Delta_{\mathrm{T}}} - w(t) + I(t), \tag{3.15}$$

where C is the membrane capacitance, g_{L} the leak conductance, E_{L} the resting potential, Δ_{T} the spike sharpness, V_{T} the spike-onset threshold, $I(t)$ the time-dependent input to the cell, and $w(t)$ the adaptation variable, which is governed by

$$\tau_{\mathrm{w}}\frac{\mathrm{d}w}{\mathrm{d}t} = a(V(t) - E_{\mathrm{L}}) - w(t), \tag{3.16}$$

where τ_{w} is the adaptation time constant and a the sub-threshold adaptation parameter. As with the standard EIF model, a spike was registered when the membrane potential reached 30 mV. On spike generation the membrane was reset to a value V_{re} and w increased by an amount b.

The parameters common to the AdEx and EIF model, namely C, g_{L}, E_{L}, Δ_{T}, and V_{T}, were fit using the dynamic I-V method described in section 3.2. The adaptation parameters τ_{w}, a, and b, along with the voltage reset V_{re} were then optimised by maximising the spike coincidence measure, defined below by equation (2.1), with the experimental trace using custom MATLAB scripts utilising the global optimisation toolbox.

3.6 Performance Metrics

A number of performance metrics were used to asses the quality of the fitted models. Since neurons have some intrinsic unreliability two identical current inputs will not produce identical spike trains. As such, when testing the performance of a model I computed two spike train coincidence measure values [equation (2.1)]: Γ_{rep}, comparing the target experimental spike train to a repeat recording obtained 10 minutes later with the same driving current; and Γ_{sim}, comparing the result of simulating the model to the target experimental recording. The ratio $\Gamma_{\text{sim}}/\Gamma_{\text{rep}}$ compares the model spike train to the intrinsic reliability of the cell. As stated in Section 2.2, cells were discarded as unreliable if $\Gamma_{\text{rep}} < 0.75$, a criterion failed by 13% of all cells analysed.

To compare the sub-threshold voltage behaviour between the model and the experimental recording I used the root mean squared deviation (RMSD), which is defined by

$$RMSD = \frac{1}{N}\sqrt{\sum_{t\in\psi}\left(V_{\text{ref}}(t) - V_{\text{sim}}(t)\right)^2}, \tag{3.17}$$

where ψ is the set of data points omitting those within a time 2 ms prior to and a time t_{ref} (the refractory period) after spike peaks; N is the total number of data points in ψ; $V_{\text{ref}}(t)$ is the reference voltage trace (i.e. the cell); and V_{sim} is the simulated (i.e. model) voltage trace. To quantify the sub-threshold performance of the model relative to the intrinsic reliability of the cell I took the RMSD ratio, which is defined as the ratio of the RMSD between the model and experiment to the RMSD between the experiment and a repeat recording.

3.7 Simulation of Continuous Models

In Chapter 8 I investigate the role of slow sodium-channel inactivation in spike-threshold variability, for which I simulate the responses of two continuous models: the Wang-Buzsáki model, introduced on page 15; and the novel slow sodium inactivation (SSI) model, introduced later in Section 8.2.1. To simulate these models I implemented a Runge-Kutta 4^{th} order method to numerically integrate the system

using a time step of 50 μs. Simulations with background channel noise were performed using an input current consisting of an excitatory (e) and an inhibitory (i) conductance:

$$I = g_e(t)(E_e - V) + g_i(t)(E_i - V), \tag{3.18}$$

where $g_j(t)$ is the time dependent conductance and E_j the reversal potential of channel $j \in \{e, i\}$. The conductances are governed by an Ornstein-Uhlenbeck Process (Uhlenbeck and Ornstein 1930) shown to be representative of *in vivo*-like activity (Destexhe *et al.* 2001):

$$\tau_j \frac{\mathrm{d}g_j}{\mathrm{d}t} = g_{j0} - g_j + \sigma_j \sqrt{2\tau_j}\xi_j(t), \tag{3.19}$$

where ξ_j is a delta-correlated white noise, τ_j the channel time constant, g_{j0} the mean conductance, and σ_j the noise amplitude for channel $j \in \{e, i\}$. The time constants, reversal potentials, and noise amplitudes were based on Richardson *et al.* (2003) and held constant (Table 3.1), and the mean conductances chosen to give a mean firing rate of ~ 5 Hz in the absence of any external drive. These values were $g_{e0} = 0.046$ μS/cm^2 for the SSI model, $g_{e0} = 0.041$ μS/cm^2 for the original model, and $g_{i0} = 0.07$ μS/cm^2 for both models.

Table 3.1: Channel noise parameters.

τ_e	3 ms	τ_i	10 ms
E_e	0 mV	E_i	-75 mV
σ_e	0.019 μS/cm^2	σ_i	0.015 μS/cm^2

3.8 Statistical Analysis

In Chapters 4 and 5 I use a number of advanced statistical techniques, which will be detailed here. Unless otherwise stated I made pairwise comparisons by performing Mann-Whitney's U test at the 5% significance level, and means are quoted $\pm$ the standard error of the mean. To control for the familywise error rate I applied the Bonferroni correction for multiple comparisons.

In Chapter 5 I use principal component analysis (PCA) to investigate the sources of variability in the dataset, along with Gaussian mixture models, linear discriminant analysis, and random forests in an attempt to automatically discriminate between cell classes. Prior to performing any of these techniques I transformed log-normally distributed parameters into log-space, so that they were normally distributed, to remove any bias towards high numerical values of a given parameter. After this I normalised the dataset by calculating the Z-score:

$$Z = (\mu_i - X)/\sigma_i, \tag{3.20}$$

where μ_i and σ_i are the mean and standard deviation, respectively, of parameter i.

Since random decision forests, introduced by Breiman (2001), are a non-standard technique in neuroscience I shall describe the method of fitting and using them here in detail. A random forest is constructed of many individual classification trees that are each trained on a bootstrapped sample of the dataset. During classification each tree in the forest classifies the object independently, or 'votes' for the class. The forest output is then the class with the most votes. For a dataset of N objects (i.e. cells), each with M parameters (i.e. measured cell parameters). Each tree is then grown as follows:

1. A bootstrapped sample of size N is taken from the original dataset. This sample is then used for growing the tree, and the remaining objects are referred to as out-of-bag (OOB).
2. A number $m < M$ is chosen. At each node m parameters of the total M are chosen at random and the best binary split (i.e. each node as two child nodes) is decided upon based on these. This m value is held constant over the entire forest.
3. Each tree is grow in full with no pruning.

The forest classification error rate depends on two things: the correlation between the trees, an increase in which increases the forest error rate; and the strength of each tree (i.e. how good a predictor they are), an increase in which decreases the forest error rate. Using a large m value increases both of these and a small m

decreases them, so there is an optimum value of m somewhere in the middle.

When training the tree, the best split at each node is that which minimises the impurity at the two resulting child nodes. Impurity can be defined in several ways, but here I use Gini's diversity index. This is defined by

$$G = 1 - \sum_{i=1}^{c} f_i^2, \tag{3.21}$$

where c is the number of classes (in this case four) and f_i is the fraction of objects at the node of class i; if all objects are of the same class then $G = 0$, otherwise $G > 0$. Minimising G minimises the node's impurity. The best split is then that which minimises G at each of the child nodes.

There are two additional features that make random decision forests appealing for classification. Firstly, they provide an unbiased estimator of the classification error rate without the need for a separate test set or performing cross-validation. To calculate this, consider the k^{th} tree in the forest. After the k^{th} tree has been trained the OOB objects are the classified using that tree. The j^{th} object in the dataset is OOB in about one third of the trees (Breiman 2001). The proportion of times that the j^{th} object is not classified as its true class is averaged over all objects, giving an estimate of the forest error rate. This error rate decreases roughly monotonically as the number of trees in the forest increases before reaching a plateau. At this point additional trees will not provide any more predictive power.

The second appealing feature of random decision forests is that they provide an estimate of the importance of each parameter used for classification. To calculate the importance of parameter i, the algorithm proceeds as follows:

1. For each tree in the forest, classify the OOB objects and count the number of correct classifications.
2. Randomly permute the values of parameter i within the set of OOB objects for each tree.
3. Re-classify the OOB objects with permuted parameters and again count the number of correct classifications for each tree.
4. Calculate the difference between these two counts for each tree.

5. To obtain the parameter importance score of parameter i calculate the standard error of the result of step 4 from all trees in the forest.

To examine correlations in the dataset I calculated both Spearman's rank correlation coefficient and the standard covariance. To calculate Spearman's rank correlation coefficient, ρ, for a sample size n, the raw parameter values X_i and Y_i are first converted into ranks x_i and y_i, respectively, after which ρ is defined by

$$\rho = 1 - \frac{6 \sum_{i=1}^{n} d_i^2}{n(n^2 - 1)}, \tag{3.22}$$

where $d_i = x_i - y_i$. All data and statistical analyses was performed with custom MATLAB scripts utilising the Statistics and Global Optimisation toolboxes.

Chapter 4

Physiological Quantification of Neocortical Pyramidal Cells

4.1 Introduction

Pyramidal neurons are the principal excitatory cell in the neocortex and display heterogeneity in their morphology (Oberlaender *et al.* 2012; van Aerde and Feldmeyer 2013; Laramee *et al.* 2013; Marx and Feldmeyer 2013), electrophysiology (Nowak *et al.* 2003; Zaitsev *et al.* 2012; van Aerde and Feldmeyer 2013; Marx and Feldmeyer 2013), synaptic dynamics (Wang *et al.* 2006), and projection targets (Thomson and Lamy 2007). Specifically, quantifying the electrophysiology of different cell types helps us understand how neurons perform computations and relay information to the rest of the network.

Cell physiology is typically described by the cells' responses to a series of depolarising and hyperpolarising current steps. Whilst these inputs are simple and easy to interpret, they are not necessarily representative of those received *in vivo*. Furthermore, quantifying the physiological heterogeneity using these methods is often not useful for constructing a meaningful model. To address this one can quantify electrophysiology by fitting a model to a cell's response to a naturalistic stimuli that is representative of *in vivo*-like activity. Producing models that capture enough biological realism yet are simple enough to analyse, along with designing efficient algorithms with which to fit them is currently the focus of much research in compu-

tational neuroscience (Gerstner and Naud 2009). The complexity of these models ranges from the continuous biophysically realistic that capture the full action potential dynamics and can include dozens of ionic channels (Section 1.3.1), to the simple one-dimensional discontinuous that are primarily concerned with the precise timing of action potentials (Section 1.3.2).

Although attempts have been made to fit detailed continuous models (Huys *et al.* 2006; Druckmann *et al.* 2007; Huys and Paninski 2009; Hay *et al.* 2011), this is hugely challenging task due to their high dimensionality potentially leading to non-identifiability. Discontinuous integrate-and-fire models have proven to be far more popular due to their low dimensionality and mathematical tractability. Furthermore, it has been suggested that they are more relevant for somatic recordings than single-compartment, isopotential continuous models due to their sharp spike initiation (Brette 2013). Numerous discontinuous models and fitting methods have been suggested with varying degrees of success (Jolivet *et al.* 2008). Typically, the models that best fit both the sub-threshold response and spike timings have a dynamic threshold (Badel *et al.* 2008a,b; Kobayashi *et al.* 2009; Yamauchi *et al.* 2011), spike-triggered adaptation current (Brette and Gerstner 2005; Clopath *et al.* 2007), or both (Mensi *et al.* 2012). In practice, combining naturalistic stimuli with more traditional approaches will provide the most complete description of a cell's electrophysiology.

In this chapter I quantify the somatic electrophysiology of somatosensory cortical layer 2/3, layer 4, and slender- and thick-tufted layer 5 pyramidal cells. I extract key parameters from the cells' responses to a combination of square-pulse and naturalistic *in vivo*-like stimuli during whole-cell patch-clamp recordings. Many of the parameters were extracted from the cells' dynamic I-V curve (Badel *et al.* 2008a,b), a consequence of which is the generation of reduced neuron models that accurately replicate the experimental voltage time-course (a MATLAB toolbox to implement this analysis is provided in Appendix A). All cell classes studied were found to fit the exponential integrate-and-fire (EIF, Fourcaud-Trocmé *et al.* 2003) form with class-dependent parameter statistics. I quantify the fit quality of the dynamic I-V method, finding that, despite fitting parameters to an underlying biophysical

quantity rather than optimising directly to the voltage response, it is comparable or superior to that of alternative fitting approaches: the spike response model (Mensi *et al.* 2012), the multi-timescale adaptive threshold model (Kobayashi *et al.* 2009), and the adaptive exponential integrate-and-fire model (Brette and Gerstner 2005). I go on to investigate between-class differences in the post-spike response of the model parameters, with particular focus on the dynamics of the resting potential. Finally, I determine significant differences between cell classes and fit marginal parameter distributions.

4.2 Results

Whole-cell patch-clamp recordings from 136 pyramidal neurons in layers 2/3-5 of the somatosensory cortex were taken from juvenile (post-natal day 16-18) male Wistar rats (Figure 4.1A). Before proceeding with the quantitative analysis I first classified the cells based on laminar location, somatic size and morphology prior to recording, the spiking pattern in response to step currents (Figure 4.1B), and the post-recording morphology of the cell either filled with a fluorescent dye or stained with biocytin. I

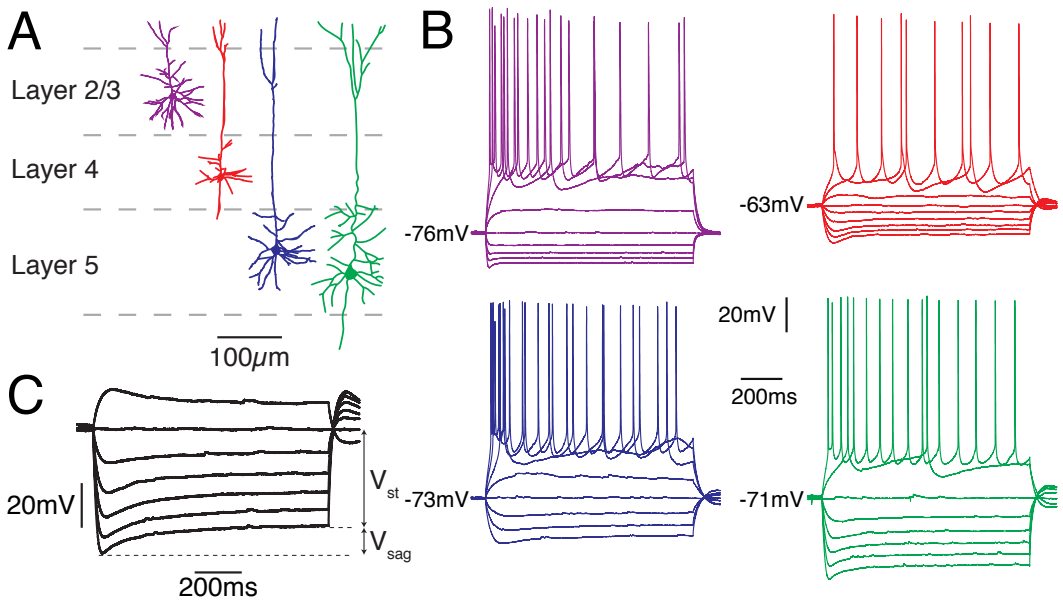

Figure 4.1: Four classes of pyramidal cells in layers 2/3, 4, and 5 were identified in this study. **A** From left to right, layer 2/3 (purple), layer 4 (red), slender-tufted layer 5 (blue), and thick-tufted layer 5 (green) pyramidal cells. **B** Representative intracellular-voltage response of the cells shown in A to a series of 1000 ms step currents. **C** The sag depth $S = 100 \times V_{\text{sag}}/V_{\text{st}}$.

recorded from four classes of pyramidal cells: layer 2/3 (L2/3, $n = 31$); layer 4 (L4, $n = 29$); slender-tufted layer 5 (SL5, $n = 29$); and thick-tufted layer 5 (TL5, $n = 47$), corresponding to previous classifications (Connors and Gutnick 1990; Douglas and Martin 2004; Thomson and Lamy 2007; Harris and Mrsic-Flogel 2013).

To determine a suitable sample size for each cell class I randomly generated values representative of the distribution of the resting potential using a Gaussian pseudorandom number generator. I generated 10,000 samples each of size n (in the range 10-100) with a fixed population mean $\mu_\mathrm{p} = -70\,\mathrm{mV}$ and a population standard deviation $\sigma_\mathrm{p} = 4\,\mathrm{mV}$ (other values of σ_p in the range 1-6 mV were tested and all showed the same trend). I then examined the distributions of the deviation of sample mean μ_s and sample standard deviation σ_s from μ_p and σ_p, respectively (Figures 4.2A and C main, respectively). These distributions were Gaussian and narrowed with increasing values of n. The mean of μ_s was approximately equal for all sample sizes (Figure 4.2A inset), though the mean of σ_s did not converge to the population value until n was approximately greater than 30 (Figure 4.2C inset). As one would expect, the standard deviation of μ_s and σ_s both decayed proportional to $1/\sqrt{n}$ (Figures 4.2B and D, respectively). I decided an n of approximately 30 was a

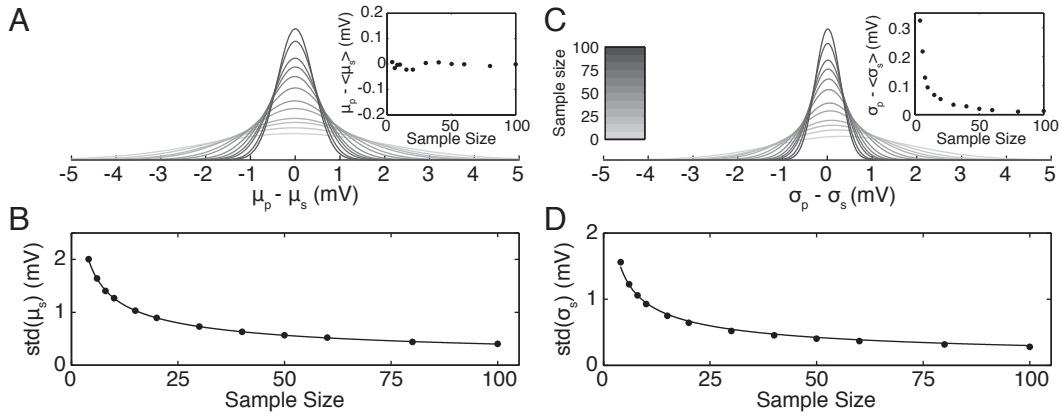

Figure 4.2: A sample size of 30 was a suitable trade off between accuracy of parameter estimation and experimental viability. Simulation of 10,000 independent normally distributed samples of the resting potential, each of size n with a fixed population mean $\mu_\mathrm{p} = -70\,\mathrm{mV}$ and population standard deviation $\sigma_\mathrm{p} = 4\,\mathrm{mV}$. **A** *Main:* Distributions of the difference between the sample mean μ_s and μ_p for n in the range 10-100. *Inset:* The mean deviation is approximately equal across all sample sizes, but **B** its standard deviation decays $\sim 1/\sqrt{n}$. **C** As panel A, for the deviation of the sample standard deviation σ_s from σ_p, which *Inset:* decays monotonically as the sample size increases. **D** As panel B, for σ_s. Data shown here is for $\sigma_\mathrm{p} = 4\,\mathrm{mV}$, but the same trends were observed across the entire parameter range (1-6 mV).

suitable trade off between accuracy and experimental viability. This gives the 95% confidence bound on μ_s and σ_s as $\pm 1.41\,\mathrm{mV}$ and $\pm 1.03\,\mathrm{mV}$, respectively.

4.2.1 Parameter Measurement

Parameters were extracted from responses to square-pulse currents and naturalistic *in vivo*-like stimuli (see Experimental Methods). A total of 25 parameters were extracted, summarised in Table 4.1, and divided into four groups: sub-threshold, firing, action potential shape, and post-spike. From the step current injections I measured three parameters: input resistance R_{in}, input conductance G_{in}, and sag depth S. The input resistance was measured from the gradient of the current-voltage relationship around the resting potential in the final 200 ms of successive 1000 ms current steps, and the input conductance calculated from its reciprocal. The sag depth was measured as the percentage change between the most negative membrane potential and the average membrane potential in the final 200 ms of a 1000 ms hyperpolarising current step (Figure 4.1C, $S = 100 \times V_{sag}/V_{st}$).

Four parameters and their refractory dynamics were extracted from the response to a fluctuating naturalistic stimuli using the dynamic I-V method, which measures the instantaneous current-voltage relationship of the cell. The time-course of the ionic current $I_{ion}(t)$ is calculated from the difference between the injected current $I_{in}(t)$ and the capacitive current:

$$I_{ion}(V,t) = I_{in}(t) - C\frac{\mathrm{d}V}{\mathrm{d}t}, \tag{4.1}$$

where C is the membrane capacitance and V is the membrane potential (Figure 4.3A). The membrane capacitance can be extracted via a previously used variance minimisation technique (Badel *et al.* 2008a,b, Section 3.2), allowing us to calculate the instantaneous current-voltage relationship (Figure 4.3B inset, grey). The dynamic I-V curve is then defined as

$$I_{dyn}(V) = \langle I_{ion}(V,t) \rangle_V \,, \tag{4.2}$$

Table 4.1: Parameters measured in this study, divided (from top to bottom) into sub-threshold, firing, action potential shape, and post-spike properties.

Parameter	**Description**
C	Membrane capacitance (pF)
R_{in}	Input Resistance (MΩ)
G_{in}	Input conductance (nS)
τ	Membrane time constant (ms)
E	Membrane resting potential (mV)
S	Sag percentage from hyperpolarising current
$V_{\text{T}} - E$	Distance between rest and spike-onset threshold (mV)
V_{T}	Spike-onset threshold (mV)
I_{spike}	Spike initiation current (pA)
Δ_{T}	Spike sharpness (mV)
A_{amp}	Action potential amplitude (mV)
A_{dur}	Action potential duration (ms)
A_{rise}	Action potential maximal rate of rise (mV/ms)
g_1	Post-spike jump in conductance (nS)
τ_g	Conductance decay time constant (ms)
V_{T1}	Post-spike jump in spike-onset threshold (mV)
τ_{T}	Spike-onset threshold decay time constant (ms)
E_1	1^{st} E exponential coefficient (mV)
τ_1	1^{st} E exponential time constant (ms)
E_2	2^{nd} E exponential coefficient (mV)
τ_2	2^{nd} E exponential time constant (ms)
E_{jump}	Post-spike jump in E (mV)
E_{sag}	Post-spike sag in E (mV)
t_{sag}	Post-spike time of E_{sag} (ms)
t_0	Post-spike time at which E crosses baseline (ms)

the average ionic current as a function of voltage (Figure 4.3B inset, red).

Relating the ionic current to a voltage dependent quantity allows for direct generation of non-linear integrate-and-fire models of the form

$$\frac{\mathrm{d}V}{\mathrm{d}t} = F(V) + \frac{I_{\text{in}}(t)}{C}, \tag{4.3}$$

where the forcing function $F(V)$ is related to the dynamic I-V curve via $F(V) = -I_{\text{dyn}}(V)/C$. It has previously been shown that the empirical forcing function of TL5 pyramidal cells is well fit by the exponential integrate-and-fire (EIF) form

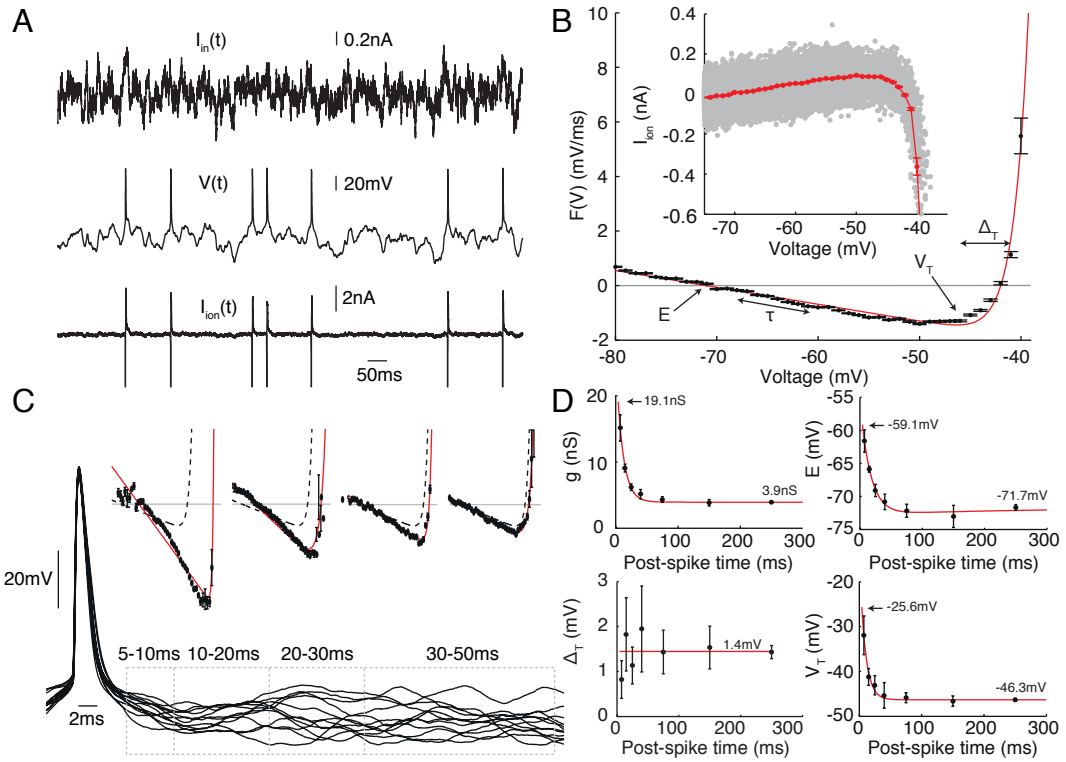

Figure 4.3: Quantification of the dynamic I-V curve. **A** A naturalistic current $I_{\text{in}}(t)$ was injected into the soma of a cortical layer 4 pyramidal cell and the voltage $V(t)$ measured. The ionic current $I_{\text{ion}}(t)$ was then calculated from equation (4.1). **B** *Inset*: Scatter plot of I_{ion} as a function of V (grey) and the dynamic I-V curve (red). Only isolated spikes were considered by excluding data 200 ms following each spike. *Main*: Quantification of the pre-spike dynamic I-V curve by fitting to the non-linear term of the exponential integrate-and-fire model given by equation (4.4). **C** Post-spike quantification of dynamic I-V curves in small time slices following spikes. Dashed lines indicate pre-spike curve. **D** Spike-triggered dynamics of, from top left to bottom right, the membrane conductance g (proportional to the inverse of the membrane time constant), membrane resting potential E, spike sharpness Δ_{T}, and spike-onset threshold V_{T}. Dynamics measured from the end of the refractory period t_{ref}, which in this case was 4 ms. All except Δ_{T} are well fit by exponential functions. Error bars indicate the standard deviation calculated from 500 bootstrap samples from the set of isolated spikes.

(Fourcaud-Trocmé *et al.* 2003), given by

$$F(V) = \frac{1}{\tau}\left(E - V + \Delta_{\text{T}} e^{(V-V_{\text{T}})/\Delta_{\text{T}}}\right), \tag{4.4}$$

where τ is the membrane time constant, E the resting potential, Δ_{T} the spike sharpness, and V_{T} the spike-onset threshold (Figure 4.3B, main). I found this form to be a good fit for all classes of pyramidal cells examined in this study. These four parameters together with the capacitance characterise the cell's response in the time period preceding isolated spikes (defined as spikes with a preceding inter-spike

interval greater than 200 ms).

This method can be used to quantify the post-spike response of the parameters in equation (4.4) by fitting the dynamic I-V curve to data from small time slices following each isolated spike; the I-V curve shifts on spike initiation and subsequently relaxes back to baseline over a period of tens of milliseconds (Figure 4.3C). We measure these parameter dynamics from the end of the absolute refractory period t_{ref} (in this case 4 ms) since this is a more relevant quantity than the parameter value at the peak of the spike. The spike-triggered response of the membrane conductance g (calculated from C/τ), resting potential, and spike-onset threshold all followed dynamics that could be well captured by a single- or double-exponential (Figure 4.3D), given by

$$g = g_0 + g_1 e^{-(t-t_{\mathrm{ref}})/\tau_{\mathrm{g}}}, \tag{4.5}$$

$$E = E_0 - E_1 e^{-(t-t_{\mathrm{ref}})/\tau_1} + E_2 e^{-(t-t_{\mathrm{ref}})/\tau_2}, \tag{4.6}$$

$$V_{\mathrm{T}} = V_{\mathrm{T0}} + V_{\mathrm{T1}} e^{-(t-t_{\mathrm{ref}})/\tau_{\mathrm{T}}}, \tag{4.7}$$

respectively, where t is the time since the peak of the previous spike; t_{ref} is the refractory period; g_0, E_0, and V_{T0} are baseline values calculated from the pre-spike dynamic I-V curve; g_1, E_1, E_2, and V_{T1} are constant exponential coefficients; and τ_{g}, τ_1, τ_2, and τ_{T} are the exponential time constants. The spike sharpness showed no spike-triggered dynamics (Figure 4.3D). These parameters are summarised in the fourth section of Table 4.1; the final four parameters, E_{jump}, E_{sag}, t_{sag}, and t_0 are measured from the dynamics of E and will be introduced on page 54. These parameter dynamics for L2/3, L4, and SL5 pyramidal cells were of the same form as those previously found for TL5 pyramidal cells (Badel *et al.* 2008a,b).

Finally, two additional parameter sets were extracted. The action potential shape was characterised by the average amplitude, duration, and maximal rate of rise of isolated spikes. The excitability of the cell was quantified using two hybrid parameters, the distance to spike-onset threshold from rest $V_{\mathrm{T}} - E$, and the spike initiation current $I_{\mathrm{spike}} = G_{\mathrm{in}}(V_{\mathrm{T}} - E)$.

4.2.2 Quality of the Fitted Parameters

To determine the quality of the parameters fitted using the dynamic I-V method I simulated the response of the refractory EIF (rEIF) model, which is the standard EIF model supplemented by the post-spike dynamics shown in Figure 4.3D, to several novel naturalistic stimuli and compared the result to that of the real cell. I discussed the procedure for simulating the rEIF model in Section 3.4, but before I quantify the performance of this model I shall briefly discuss the problem of setting a post-spike reset value in this family of model.

Post-spike Voltage Reset in Integrate-and-fire Models

Integrate-and-fire models such as the rEIF model do not capture the action potential waveform. As such, once the voltage reaches a threshold V_{th} (in this case 30 mV) a spike is registered and the voltage reset to a value V_{re} where it is held for a refractory period t_{ref} that represents the spike duration and absolute refractory period. It is common for the reset to be set a long way below spike-onset threshold, typically around the value of the resting potential (Burkitt 2006a,b), to avoid repetitive firing. However, in neocortical pyramidal cells during a naturalistic current stimuli the reset is typically high (Figure 4.4 main). In a typical L2/3 pyramidal cell the mean voltage

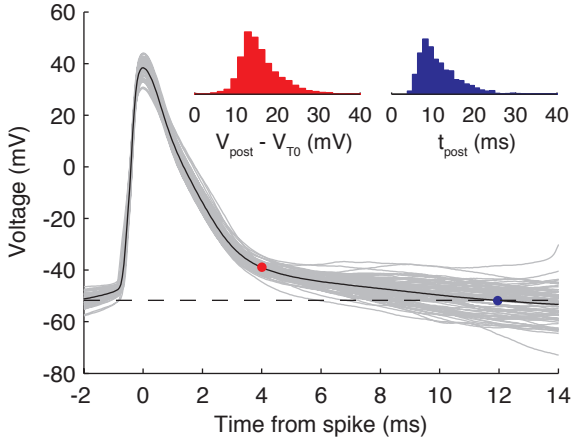

Figure 4.4: The post-spike voltage in pyramidal cells is typically above baseline threshold, implying a high reset. *Main:* Individual spikes (grey), average spike (black), baseline threshold (dotted line), average voltage after 4 ms (red dot, -39 mV), and average time to return to baseline threshold (blue dot, 12 ms) of a layer 2/3 pyramidal cell during a naturalistic current stimuli. *Inset:* Histograms of the voltage 4 ms post-spike (red) and the time to return to baseline threshold post-spike (blue). Data from 1833 spikes.

4 ms after the peak of an isolated spike, V_{post}, was 12.7 mV more depolarised than the baseline spike-onset threshold of -51.7 mV. Furthermore, the mean time at which the membrane potential crosses back below baseline threshold after a spike, t_{post}, was 12.0 ms. The distributions of V_{post} and t_{post} are wide (Figure 4.4 inset); the distance between V_{post} and baseline threshold ranges from approximately 5 mV to 30 mV and the value of t_{post} ranges between 5 ms and 50 ms. From this I concluded that to increase the experimental relevance of a model, the reset should be set to a high value at or above baseline threshold, with an adaptation mechanism preventing repetitive firing.

I chose t_{ref} to be 4 ms and then took V_{re} to be equal to the voltage 4 ms after the peak of the average action potential waveform of isolated spikes (corresponding to t_{post} and V_{post}, respectively, in Figure 4.4); In general this reset value was more depolarised than the baseline spike-onset threshold, but the model is prevented from firing repeatedly by the refractory parameter dynamics. However, setting t_{ref} to less than 4 ms resulted in repetitive firing. Finally, it is important to note that the reset and refractory period were not optimised as part of the dynamic I-V method, but rather measured directly from the cell's response.

Quantifying Performance of the rEIF Model

Figure 4.5A shows an example fit to the pre-spike dynamic I-V curve for each cell class, with sample traces comparing the model with the experiment shown in Figure 4.5B. The rEIF model performs well with all four cell classes. In particular, the model is in good agreement not only with the sub-threshold voltage and the spike timings but also the voltage response immediately after spikes.

To quantify the accuracy of the fits I used a number of measures, which are tabulated in Table 4.2. To asses the firing precision I used three measures: the percentage of correctly matched spikes; the percentage of false spikes; and the coincidence ratio, which compares the similarity of the model and experimental spike trains to the intrinsic cell reliability. Overall, the rEIF model successfully matched $75 \pm 0.85\%$ of spikes with a 5 ms precision, with an average false positive rate of $36 \pm 0.91\%$. The average coincidence ratio was 0.81 ± 0.011. The cell class in which

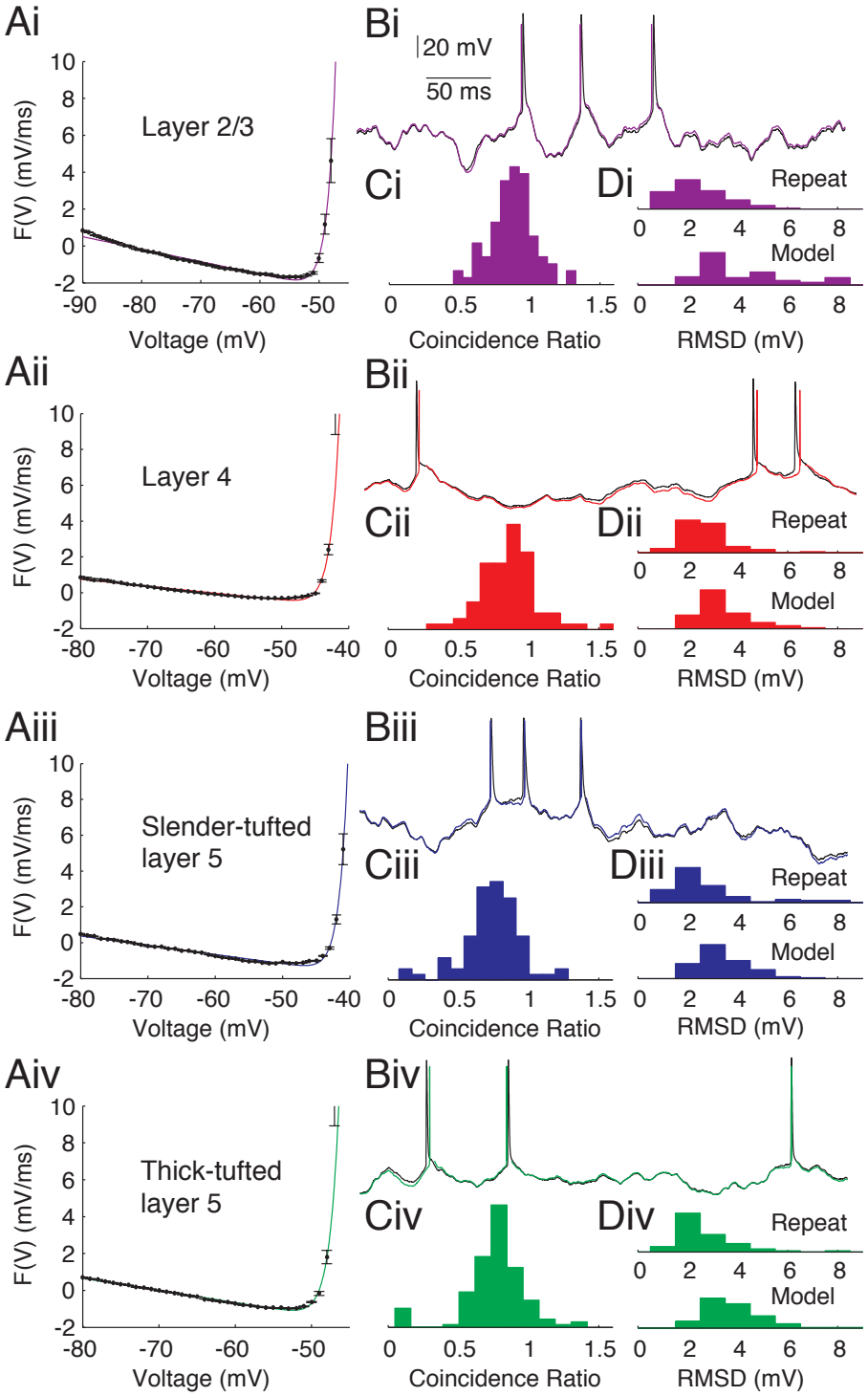

Figure 4.5: The dynamic I-V method of fitting the refractory EIF (rEIF) model matches the response of neocortical pyramidal neurons from layers 2/3-5. **A** Quantification of the dynamic I-V for example (i) layer 2/3 (purple), (ii) layer 4 (red), (iii) slender-tufted layer 5 (blue), and (iv) thick-tufted layer 5 (green) pyramidal cells. **B** Example traces (400 ms) comparing the response of the model (colour) to the experimental trace (black). **C** Histograms showing the distribution of coincidence ratios. **D** Histograms showing the root-mean-square deviation (RMSD) of the sub-threshold voltage (top) between the experiment and a repeat stimulus recorded 10 minutes later and (bottom) between the experiment and the model.

Table 4.2: Performance metrics for all cells and for each class separately of the rEIF model fit. Values quoted are mean ± SEM.

	All	**L2/3**	**L4**	**SL5**	**TL5**
Matched spikes %	75 ± 0.85	84 ± 1.1	71 ± 1.9	66 ± 2.2	77 ± 1.2
False spikes %	36 ± 0.91	30 ± 1.6	29 ± 1.6	39 ± 1.7	42 ± 1.7
Coincidence ratio	0.81 ± 0.011	0.88 ± 0.018	0.86 ± 0.023	0.74 ± 0.023	0.76 ± 0.020
Repeat RMSD (mV)	2.8 ± 0.088	2.5 ± 0.12	2.9 ± 0.184	2.7 ± 0.18	3.0 ± 0.18
Model RMSD (mV)	3.8 ± 0.089	4.6 ± 0.30	3.4 ± 0.12	3.4 ± 0.12	3.8 ± 0.10

the firing precision was best fit was L2/3 cells, where the rEIF model successfully matched $84 \pm 1.1\%$ of spikes with a coincidence ratio of 0.88 ± 0.018 (Figure 4.5Ci). The model performed worse with SL5 cells, only matching $66 \pm 2.2\%$ of spikes with a coincidence ratio of 0.74 ± 0.023 (Figure 4.5Ciii).

To asses the sub-threshold response I measured the root-mean-square deviation [RMSD, equation (3.17)] between the experiment and model (Figure 4.5D bottom) and compared it to the RMSD between the experiment and a repeat response to an identical stimulus recorded 10 min later (Figure 4.5D top), the results of which are tabulated in Table 4.2. Overall, the model deviated from the experiment on average 3.8 ± 0.089 mV, compared to a deviation of 2.8 ± 0.088 mV between the experiment and the repeat; a 36% increase. The RMSD between repeat experiments for the four cell classes separately were similar (2.5-3 mV, Figure 4.5D top). However, the model captured the sub-threshold response of L2/3 cells significantly worse than the other three classes with an RMSD of 4.6 ± 0.30 mV (Figure 4.5Di bottom), an 84% increase over the deviation between repeat experiments within that class.

Comparison with Alternative Model Fitting Approaches

I next compared the quality of fitting the rEIF model using the dynamic I-V method to that of three recent alternative models: the spike-response model (SRM, Mensi *et al.* 2012), which models the cell with a deterministic sub-threshold dynamics and stochastic spike emission displaying both a spike-triggered threshold decay and adaptation current; the multi-timescale adaptive threshold model (MAT, Kobayashi *et al.* 2009), which again has a deterministic sub-threshold dynamics but coupled with a deterministic spike-triggered multi-timescale threshold dynamics with no adaptation current; and the adaptive EIF model (AdEx, Brette and Gerstner 2005), which

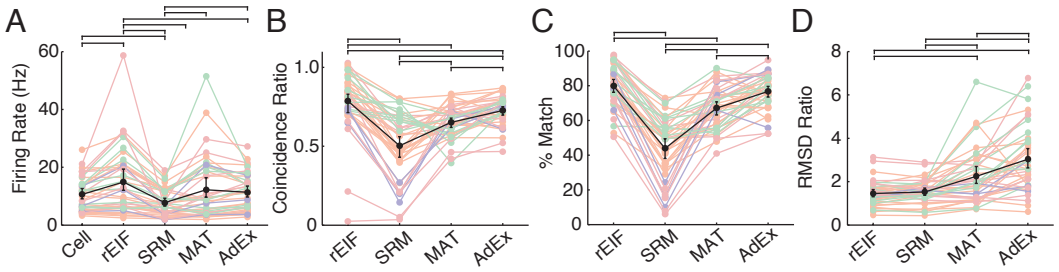

Figure 4.6: Comparison in performance between the rEIF model and three alternative models: the spike-response model (SRM, Mensi *et al.* 2012); the multi-timescale adaptive threshold model (MAT, Kobayashi *et al.* 2009); and the adaptive EIF model (AdEx, Brette and Gerstner 2005), quantified with the **A** firing rate, **B** coincidence ratio, **C** percentage of matched spikes, and **D** the ratio of the RMSD between the experiment and the model to the RMSD between the experiment and the repeat trace. Mean values indicated in black and results for individual cells (41 distinct sweeps from 16 cells) are indicated in colour corresponding to cell class. Error bars show the 95% bootstrap confidence interval calculated using 2000 bootstrap samples. Horizontal bars denote statistical significance between models calculated using the Wilcoxon ranked signed test for paired comparisons, with the application of the Bonferroni correction for multiple comparisons at a confidence level of 5%.

is the standard EIF model coupled to an adaptation variable with a spike-triggered jump and subsequent voltage dependent decay. See Sections 3.5.1, 3.5.2, and 3.5.3, respectively, for full descriptions of these models. The SRM and MAT models are fundamentally different to the dynamic I-V method in their fitting procedure as they fit directly to the voltage response of the cell rather than to a biophysical quantity. I re-fit a subset of my recordings from across all four cell classes using these alternative approaches. The AdEx model is an extension of the standard EIF model that adds an adaptation current with sub-threshold and spike-triggered components. To fit this model I used the pre-spike dynamic I-V curve to determine the parameters common to the AdEx and EIF models, and to fit the remaining adaptation parameters I implemented a procedure similar those used to fit the SRM and MAT models (see Theoretical Background).

Two of the models fired at a significantly different rate to the cell. The SRM fired at 7.8 ± 0.89Hz, compared to the cell's 11 ± 1.2 Hz, and the rEIF model at 15 ± 2.3 Hz (Figure 4.6A). The rEIF model had a significantly higher coincidence ratio than the other three models (0.79 ± 0.032), with the SRM having the lowest (0.50 ± 0.053, Figure 4.6B). The rEIF and AdEx models performed the best in terms of the percentage of matched (Figure 4.6C) and false spikes, having the highest

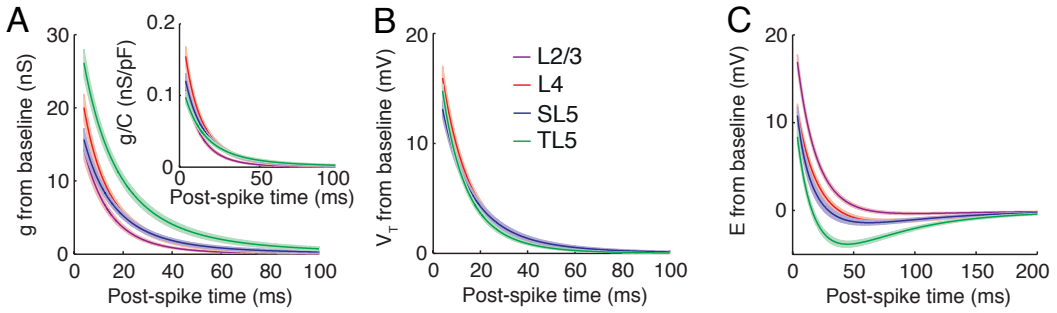

Figure 4.7: Post-spike resting potential dynamics varies considerably between cell classes. Post-spike dynamics of **A** membrane conductance, **B** spike-onset threshold, and **C** resting potential in layer 2/3 (purple), layer 4 (red), slender-tufted layer 5 (blue), and thick-tufted layer 5 (green) pyramidal cells. Mean (darker lines) ± SEM (shaded regions).

(rEIF: $80 \pm 3.0\%$, AdEx: $67 \pm 3.0\%$) and lowest (rEIF: $34 \pm 4.2\%$, AdEx: $26 \pm 2.0\%$) of these metrics, respectively. Again, the SRM performs the worst, having the lowest percentage of matched spikes ($44 \pm 4.5\%$) and highest percentage of false spikes ($44 \pm 3.8\%$). Finally, the rEIF model and SRM had the lowest RMSD ratio (rEIF: 1.45 ± 0.14, SRM: 1.52 ± 0.14) with no statistical difference between them. The AdEx model had the highest RMSD ratio (3.0 ± 0.37), significantly higher than the other three models (Figure 4.6D).

4.2.3 Post-spike Parameter Response

Figure 4.7 shows the mean responses of g, E, and V_{T} for each of the four cell classes. TL5 cells appear to have a larger post-spike conductance increase (Figure 4.7A main). However, after normalising by capacitance, a quantity proportional to membrane area, the responses were more similar across pyramidal populations indicating that this extra conductance increase in TL5 cells is due to their size rather than any differences in underlying channel properties (Figure 4.7A inset). The post-spike threshold response showed little difference between the four classes (Figure 4.7B), with all showing a significant jump of approximately 15 mV from baseline. Finally, the post-spike dynamics of the resting membrane potential was markedly different across cell classes with, L2/3 cells displaying a mono-exponential response whereas TL5 cells featured a large spike-triggered sag. The other two classes were intermediate (Figure 4.7C).

The post-spike response of the resting potential was fit by the double-exponential

given in equation (4.6). Despite a marked difference in the mean post-spike response of the resting potential between cell classes (Figure 4.7C), the parameters fit to the refractory dynamics showed little class dependence (Figure 4.8A). Interestingly, there was a class independent relationship between the two exponential coefficients given by $E_1 = E_2 - 17.3$ (Figure 4.8B), and 62% of cells lay on a class independent relationship between the two exponential time constants given by $\tau_{E1} = 1.10\tau_{E2} - 0.781$ (Figure 4.8C). After restricting the time constants to this relationship and re-fitting the refractory dynamics of E for every cell in the dataset, the exponential coefficients lay on virtually the same best-fit line as previously (Figure 4.8D). In restricting the fit in this way the sum of squared residuals did not change greatly from the original fit (Figure 4.8E), and neither did performing a global search for the optimal parameters. This suggests that the observed response is practically non-identifiable, i.e. there are multiple local minima in parameter space that fit the response equally well. These results indicate that the parameters E_1, τ_1, E_2, and τ_2 do not best describe the observed response difference between cell class.

To describe the shape of the spike-triggered resting potential response I defined four new parameters: the post-spike jump in the resting potential, E_{jump}; the post-spike time at which the response first crosses below baseline, t_0; and the depth, E_{sag}, and post-spike time, t_{sag}, of the subsequent sag (Figure 4.9A). It has previously been suggested (Badel *et al.* 2008a) that the double-exponential dynamics of E may be the result of a transient inactivation of the I_{h} current over the duration of the action potential followed by a gradual post-spike re-activation. To investigate this I measured the post-spike dynamics of E in TL5 cells under control conditions and following the application of 25 μM ZD7288, shown to block I_{h} channels at this concentration (Harris and Constanti 1995). On blockade of these channels the double-exponential response shifted to a mono-exponential (Figure 4.9B). Post drug application there was significant membrane hyperpolarisation (Figure 4.9C), an increase in post-spike jump (Figure 4.9D), and a reduction or complete abolition of the post-spike sag (Figure 4.9E).

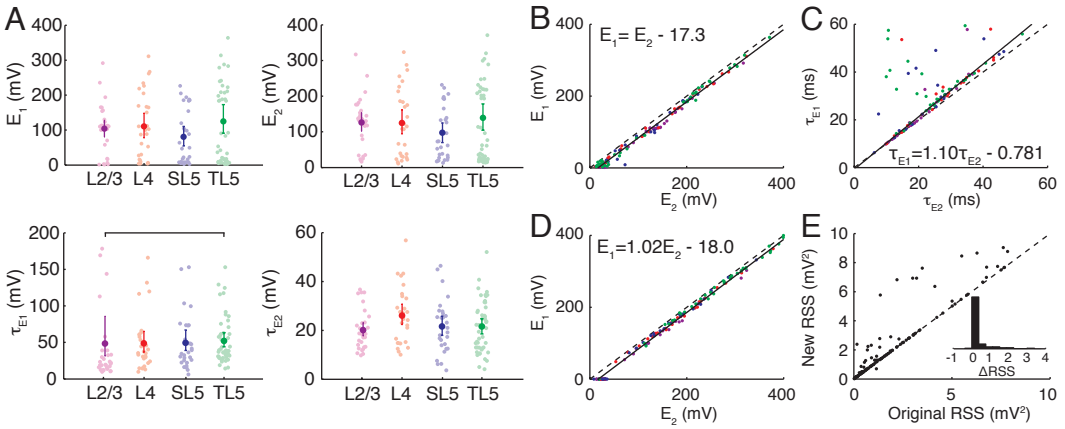

Figure 4.8: Parameters of a double exponential fit to the post-spike dynamics of the resting potential do not capture the class-dependent response. **A** Parameters of a double exponential fit to the post-spike dynamics of the resting potential for layer 2/3 (purple), layer 4 (red), slender-tufted layer 5 (blue), and thick-tufted layer 5 (green) neocortical pyramidal cells. Mean parameter values indicated by the dark coloured points and data points are indicated by pale coloured points. Error bars show the 95% bootstrap confidence interval calculated using 2000 bootstrap samples. Horizontal bars denote statistical significance between cell classes after applying the Bonferroni correction for multiple comparisons at a 5% confidence level. **B** Exponential coefficients have a class independent relationship given by $E_1 = E_2 - 17.3$. **C** Exponential time constants of 62% of cells lie on a class independent relationship given by $\tau_{E1} = 1.10\tau_{E2} - 0.781$. **D** After re-fitting the post-spike resting potential dynamics whilst restricting the time constants to the relationship shown in C, the exponential coefficients lay on an almost identical line to the original fitting. **E** The sum of squared residuals after refitting do not increase significantly from the original fit.

4.2.4 Differences Between Cell Classes

Between class comparisons of the 21 parameters outlined in Table 4.1 are shown in Figure 4.10 (left plots), along with fitted distributions (right plots). Pairwise significance tests were performed for each parameter to identify significant differences between classes.

Sub-threshold parameters are shown in Figure 4.10A. L2/3 cells were well distinguished by their shorter time constant, hyperpolarised resting potential, and lack of sag response to a hyperpolarising step current. TL5 cells were well distinguished by their larger capacitance and input conductance, smaller input resistance, and are further separated from L2/3 and L4 cells by their more depolarised resting potential and strong sag response. The only significant difference between L4 and SL5 cells is their sag percentage, with SL5 cells displaying a significantly larger response.

Firing parameters are shown in Figure 4.10B. The most prominent feature of this parameter grouping is that the distance between rest and spike-onset threshold

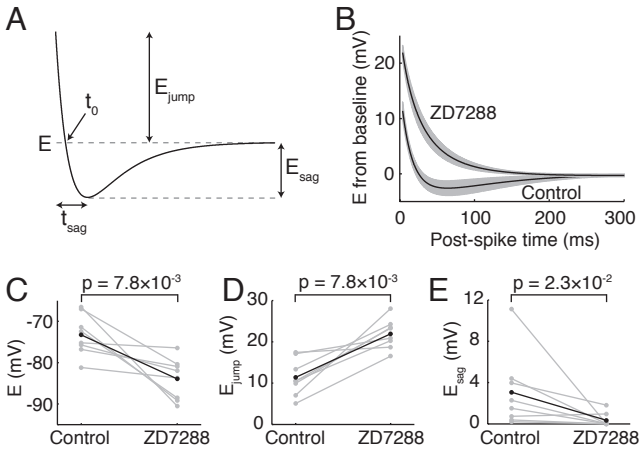

Figure 4.9: Post-spike sag in resting potential is mediated by I_{h} current. **A** Four measures were defined that capture the form of the response: the post-spike jump in the resting potential, E_{jump}; the post-spike time at which the response first crosses below baseline, t_0; and the depth, E_{sag}, and post-spike time, t_{sag}, of the subsequent sag. **B** Mean response $\pm$ SEM of eight thick-tufted layer 5 pyramidal cells in control and after application on 25 μM ZD7288. After drug application significant changes were seen in **C** the resting potential, **D** post-spike jump, and **E** sag depth.

$V_{\mathrm{T}} - E$ decreased monotonically between L2/3 and TL5 cells from 30 mV to 16 mV. The majority of this decrease is the result of an increasingly depolarised resting potential (Figure 4.10A bottom middle panel) rather than a drop in threshold; however, TL5 cells do have a significantly more hyperpolarised threshold than the other three classes. On normalising the distance to spike-onset threshold by the input conductance, L2/3 and TL5 have a larger spike initiation current than L4 and SL5 cells, indicative of a lower excitability.

Action potential shape parameters are shown in Figure 4.10C. TL5 cells were well separated by their larger spike amplitude (consistent with a lower spike-onset threshold), shorter duration, and larger maximal rate of rise. Furthermore, L2/3 cells can be discriminated from layer 5 cells by their longer spike duration. This parameter also discriminates L4 and SL5 cells, one of only two parameters in the dataset to do so. There was no difference in the spike sharpness parameter between classes.

Post-spike parameters are shown in Figure 4.10D. TL5 cells displayed a larger spike-triggered jump in conductance than L2/3 and SL5 cells (due to their larger size, *cf.* Figure 4.7A) and longer decay time constant than L2/3 cells. The only significance difference in the post-spike threshold dynamics was the jump size between

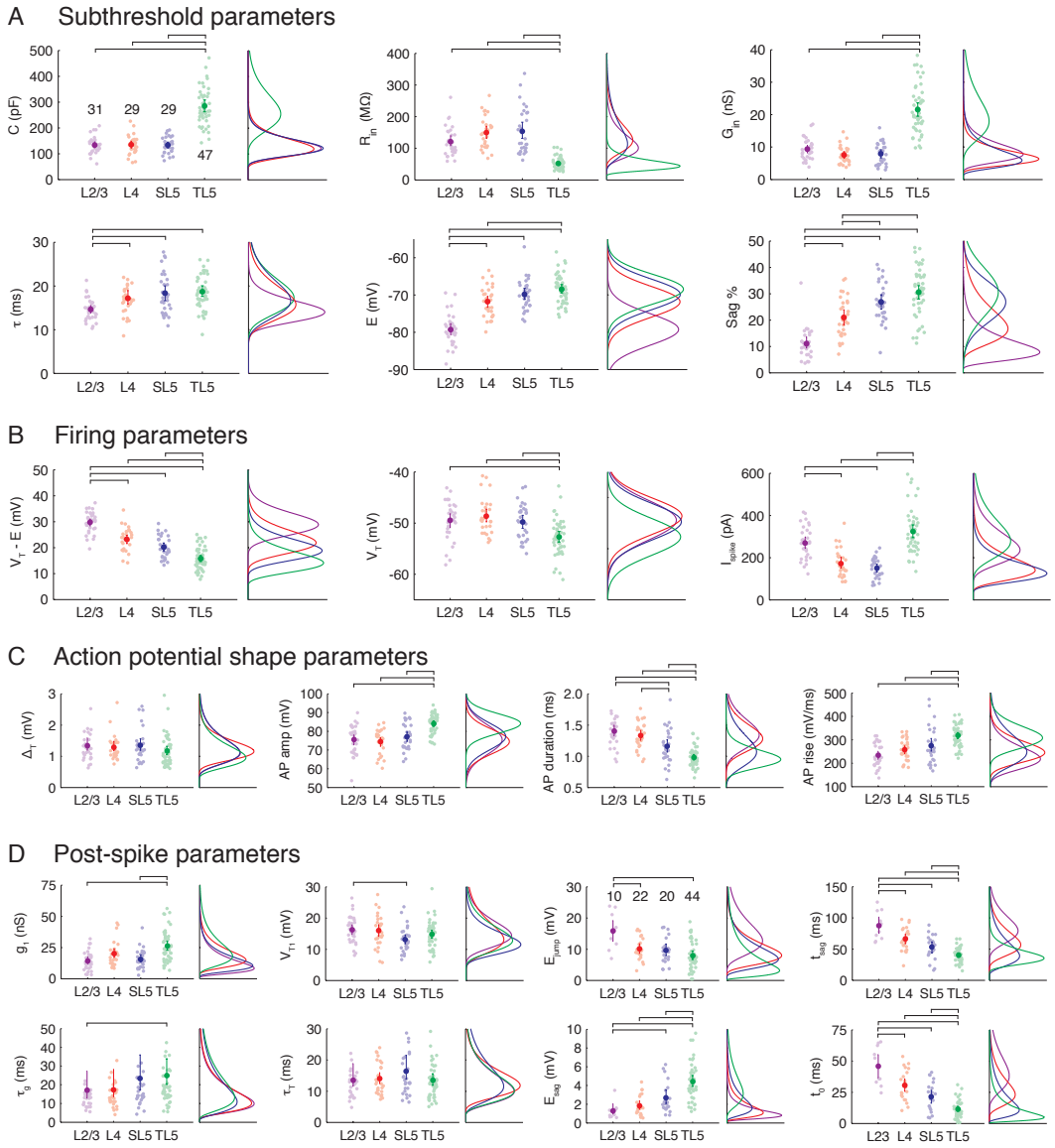

Figure 4.10: Quantification of heterogeneity in neocortical pyramidal cell populations. The parameter groupings are: **A** sub-threshold, **B** firing, **C** action potential shape, and **D** post-spike parameters for layer 2/3 (purple), layer 4 (red), slender-tufted layer 5 (blue), and thick-tufted layer 5 (green) neocortical pyramidal cells. For each parameter the left panel shows the mean value (darker point) and all data (pale points) with error bars showing the 95% bootstrap confidence interval from 2000 samples. Horizontal bars above each panel denote statistically significant differences between cell classes (5% confidence, Bonferroni corrected). The right panels show fitted distributions for each pyramidal cell class.

L2/3 and SL5 cells, with the latter having a smaller increase. The dynamics of the resting potential displayed a more marked difference between cell classes. Considering first only those cells that displayed a post-spike sag ($E_{\text{sag}} > 0.5\,\text{mV}$), the post-spike jump of L2/3 cells was significantly larger than that of L4 and TL5 cells. Furthermore, L2/3 and TL5 cells displayed a smaller and larger sag response, and

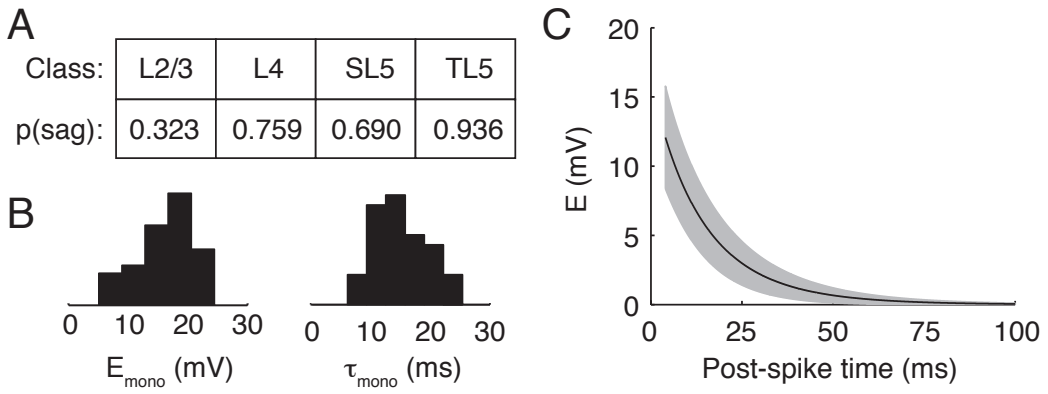

Figure 4.11: Cells not displaying a post-spike sag response in membrane resting potential could be described by a mono-exponential drawn from a class-independent distribution. **A** Proportion of cells in each class that displayed a post-spike sag response. **B** Histograms of the fitted values of post-spike jump E_{mono} and decay time constant τ_{mono} for those cells not displaying a post-spike sag ($n = 40$). **C** Mean mono-exponential post-spike response in resting potential (black) $\pm$ standard deviation (grey).

a later and earlier sag timing (measured from t_{sag} and t_0), respectively, than either L4 or SL5 cells. This is consistent with the sag depth magnitudes in response to a hyperpolarising step current (Figure 4.10A bottom right panel), given that the response is mediated by the I_{h} current (Figure 4.9).

The proportion of cells for each class that displayed a post-spike sag in the resting potential is summarised in Figure 4.11A. The response of the remaining cells ($n = 40$) could be captured by a mono-exponential function with post-spike jump E_{mono} and decay time constant τ_{mono}, both drawn from class-independent distributions (Figure 4.11B). The mean post-spike response of this group of cells is shown in Figure 4.11C.

Along with between-class comparisons I fitted marginal parameter distributions (i.e. ignoring parameter covariance) for each cell class. The resting potential, spike-onset threshold, and action potential amplitude were well fit by normal distributions, along with the sag percentage of layer 5 cells. The remaining parameters were fit with log-normal distributions. The means and standard deviations of the fitted distributions (from which the log-normal distribution parameters can be calculated) are summarised in Table 4.3, with the exception of E_{mono} and τ_{mono}. These two parameters were also well fit by log-normal distributions with means and standard deviations (μ, σ) given by (16.1 mV, 4.8 mV) and (15.1 ms, 4.5 ms), respectively.

Table 4.3: Fitted distribution means (μ) and standard deviations (σ).

Parameter	**L2/3**		**L4**		**SL5**		**TL5**	
	μ	σ	μ	σ	μ	σ	μ	σ
C (pF)	134	32.8	135	36.7	133	31.9	284	78.5
R_{in} (MΩ)	121	45.2	149	50.5	154	73.3	52.4	19.4
G_{in} (nS)	9.3	3.2	7.5	2.7	7.9	3.4	21.5	7.4
τ (ms)	14.6	2.5	17.2	4.2	18.3	4.7	18.7	4.2
E (mV)	-79.3	4.3	-71.8	4.2	-69.9	4.2	-68.5	4.0
S(%)	11.0	5.7	21.0	7.6	26.8	7.6	30.6	9.2
$V_{\text{T}} - E$ (mV)	29.8	4.2	23.2	4.5	20.1	4.3	15.7	4.3
V_{T} (mV)	-49.5	3.8	-48.7	3.5	-49.7	3.6	-52.7	3.6
I_{spike} (pA)	270	77.4	173	66.5	150	48.6	324	105
Δ_{T} (mV)	1.3	0.5	1.3	0.4	1.3	0.5	1.2	0.5
A_{amp} (mV)	75.5	7.8	74.5	6.5	77.2	7.1	84.1	5.1
A_{dur} (ms)	1.4	0.2	1.3	0.2	1.2	0.3	1.0	0.1
A_{rise} (mV/ms)	234	50.3	258	46.2	275	76.8	319	46.9
g_1 (nS)	14.3	7.5	20.0	9.6	15.7	7.7	26.1	12.5
τ_{g} (ms)	17.0	17.4	17.3	15.8	23.3	23.9	24.9	22.3
V_{T1} (mV)	16.2	4.4	15.9	5.1	13.1	4.0	14.8	4.4
τ_{T} (ms)	13.6	8.94	14.1	4.91	16.4	9.65	13.5	6.41
E_{jump} (mV)	15.8	5.7	10.1	3.7	9.6	4.3	7.9	4.6
E_{sag} (mV)	1.3	0.9	1.8	1.1	2.7	1.7	4.4	2.0
t_{sag} (ms)	87.5	23.2	66.2	18.9	53.0	19.9	40.4	11.5
t_0 (ms)	45.9	15.7	30.6	12.2	21.6	12.0	11.5	6.8

4.3 Discussion

In this chapter I examined the passive and dynamic properties of layer 2/3, layer 4, and slender- and thick-tufted layer 5 pyramidal cells of the juvenile rat somatosensory cortex (Figure 4.1A) in response to square-pulse (Figure 4.1B) and *in-vivo*-like naturalistic stimuli (Figure 4.3A). Using the dynamic I-V curve method I found that the forcing function $F(V)$ of the exponential integrate-and-fire model (Fourcaud-Trocmé *et al.* 2003) provided an accurate fit to the current-voltage relationship of all cells measured (Figures 4.5A, Table 4.2), extending the applicability of this model from thick-tufted layer 5 pyramidal cells (Badel *et al.* 2008a), GABAergic interneurons (Badel *et al.* 2008b), and striatal neurons (Dorst 2013). Furthermore, this method outperformed alternative parameter fitting approaches (Figures 4.6).

I next examined the post-spike response of the membrane conductance, spike-onset threshold, and resting potential (Figure 4.8), finding that the latter exhibited an I_{h} mediated sag response (Figure 4.9) with a marked difference between cell classes. Finally, I investigated significant between-class parameter differences, ob-

serving a significant degree of heterogeneity between populations, and fitted marginal parameter distributions (Figure 4.10).

4.3.1 Choice of Reduced Neuron Model

The dynamic *I-V* method measures a biophysical quantity - the instantaneous current-voltage relationship - and uses this to construct an integrate-and-fire model with an empirical non-linear voltage-forcing term (Figure 4.3). This is the key difference between the dynamic *I-V* method and alternative approaches that typically propose a model *a-priori*, which may have components not directly related to the underlying biology, and optimise parameters to the observed voltage response (Paninski *et al.* 2005; Jolivet *et al.* 2006b; Kobayashi *et al.* 2009; Mensi *et al.* 2012). It has previously been shown that the forcing term of the EIF model (Fourcaud-Trocmé *et al.* 2003) provides an accurate fit to the *I-V* relationship of thick-tufted layer 5 pyramidal cells (Badel *et al.* 2008a), GABAergic interneurons (Badel *et al.* 2008b), and striatal neurons (Dorst 2013). Here I extended the applicability of this model, showing that this forcing term also provides an excellent fit to the *I-V* relationship of layer 2/3, layer 4, and slender-tufted layer 5 pyramidal cells (Figure 4.5A).

To quantify the quality of the fitted model I simulated the response of the refractory EIF (rEIF) model, an extension (Badel *et al.* 2008a) of the standard EIF model that includes the post-spike parameter dynamics shown in Figure 4.7, to novel current stimuli (Figure 4.5B). I compared these results to the intrinsic reliability of a cell, measured via comparison of two repeat experiments to the same stimuli. Overall, the rEIF model matched $75 \pm 0.85\%$ of spikes with an average coincidence ratio of 0.81 ± 0.011, and deviated from the sub-threshold response of the cell by $3.8 \pm 0.089\,\mathrm{mV}$ (a 36% increase in deviation over the repeat trace). These values are comparable to values previously quoted for alternative fitting approaches (Jolivet *et al.* 2008).

In terms of spiking response, L2/3 cells were best captured by the rEIF model matching $84 \pm 1.1\%$ of spikes with a coincidence ratio of 0.88 ± 0.018. In contrast, the sub-threshold response of L2/3 cell was captured worst by the model with an average RMSD of $4.6 \pm 0.30\,\mathrm{mV}$, compared with $3.4 \pm 0.12\,\mathrm{mV}$, $3.4 \pm 0.12\,\mathrm{mV}$, and

$3.8 \pm 0.10\,\text{mV}$ for L4, SL5, and TL5 pyramidal cells, respectively. One reason for this may be the more negative resting potential of L2/3 cells (Figure 4.10A middle bottom panel).

I compared the response of the rEIF model, fit using the dynamic I-V method, to three alternative models: the SRM (Mensi *et al.* 2012), the MAT model (Kobayashi *et al.* 2009), and the AdEx model (Brette and Gerstner 2005). Mensi *et al.* (2012) and Kobayashi *et al.* (2009) implement their own novel fitting procedures, whereas I implemented my own procedure to fit the AdEx model. The AdEx model is an extension of the standard EIF that includes an additional adaptation current in an attempt to capture the refractory nature of the cell. To determine parameters for this model I fit the standard EIF parameters using the dynamic I-V method, and the additional adaptation parameters and spike reset by maximising the spike train coincidence measure between the model and experiment. The AdEx model performs comparably to the rEIF model in terms of percentage of matched spikes (Figure 4.6C). However, it had a significantly lower coincidence ratio (Figure 4.6B) and higher RMSD ratio (Figure 4.6D). The latter is most likely due to the fitted post-spike reset value being low, typically around resting potential.

Spike generation is described differently in the SRM and MAT model. Mensi *et al.* (2012) describe spike generation stochastically using the escape rate formulation (Plesser and Gerstner 2000; Paninski *et al.* 2005) whereas Kobayashi *et al.* (2009) fit a deterministic spike threshold. Both methods fit spiking parameters that maximise the coincidence measure between the model spike train and that of the experiment. Both models have sub-threshold dynamics described by a leaky integrator, with the SRM having an additional adaptation current. Overall, both the SRM and MAT model were outperformed by the rEIF and AdEx models. In particular, the SRM had a significantly lower firing rate (Figure 4.6A), coincidence ratio (Figure 4.6B), and percentage of matched spikes (Figure 4.6C) than the other three models. However, the RMSD ratio of the SRM was the lower than both the MAT and AdEx models, but not significantly lower than the rEIF model. The MAT model outperformed the SRM in terms of spike timing (Figures 4.6B and C), but performed worse in the RMSD ratio metric, though not as poorly as the AdEx model (Figure 4.6D).

It should be noted that the values of the performance measures quoted here are worse than those previously quoted for the three alternative models. In the case of the SRM the poor performance in spike timing prediction may be a consequence of the statistics of the input current. Mensi *et al.* (2012) constructed their stimuli as a sum of six independent inhomogeneous Poisson processes convolved with an exponential filter, weighted positively or negatively to mimic excitatory and inhibitory synapses, respectively. As a result, when a cell's membrane potential is driven through threshold during an experiment it is driven through at a high rate of depolarisation and quickly achieves a large value of $V - V_{\mathrm{T}}$. Since their model fires stochastically with a firing intensity proportional to $e^{(V-V_{\mathrm{T}})}$, a spike is registered with near certainty. The stimulus used here is a Gaussian process. The neuron therefore crosses threshold with less gusto than it would in the case of the Poissonian stimulus and as a result there is a far lower probability of a spike being registered. Similarly, there is more chance in the Guassian case that the neuron is close to but not quite above threshold, leading to an increased probability of registering a false spike.

In the case of the SRM I used MATLAB code published by Mensi *et al.* (2012) so I could be sure of the proper implementation. However, Kobayashi *et al.* (2009) did not publish an implementation of their fitting method and did not provide enough detail in their article to recreate their method exactly and so discrepancies in performance may be due to subtle differences in implementation. On its introduction the AdEx model was fit to a continuous, Hodgkin-Huxley type model using the responses to a series of current pulse, steps, and ramps and produced excellent agreement (Brette and Gerstner 2005). However, only limited work has been done to fit the AdEx model to the response of a real neuron receiving naturalistic stimuli, with the results begin comparable to those presented here (Clopath *et al.* 2007). Furthermore, it should be noted that extending the AdEx model to include a moving threshold or conductance based adaptation has produced improved results (Jolivet *et al.* 2008). More generally, recent advancements in parallel computing could lead to improved fit quality of this whole class of neuron model (Rossant *et al.* 2010, 2011).

4.3.2 Poor Performing Aspects of the rEIF Model

I observed two aspects where the model failed to accurately capture the response of the cell: the precise timings of bursts of multiple closely spaced action potentials, and the membrane potential during a period of strong hyperpolarising input. Bursts are typically caused by back-propagating action potentials (Larkum *et al.* 2009), which result in dendritic spikes that propagate back towards the soma resulting in a second action potential. The rEIF model is a single compartment model and makes no attempt to capture this mechanism. This leads to a reduction in spike-time prediction accuracy in cells with a high fraction of burst spikes.

Typically, the rEIF model will fire multiple additional spikes over the bursting period of the cell's response (Figure 4.12A top), or miss the burst spikes entirely (Figure 4.12B bottom). This phenomenon is especially noticeable in TL5 cells, which have a large dendritic structure (Romand *et al.* 2011) and are know to display frequent bursts of action potentials (Kim and Connors 1993; Schiller *et al.* 1997; Larkum *et al.* 1999). It goes some way to explaining why the smaller cells in the dataset from layer 2/3, which have a far smaller dendritic extent (Oberlaender *et al.* 2012), have a higher firing precision that the other three classes (Table 4.2).

To extend the model to capture bursts one could add a dendritic compartment, such as has been previously done for the AdEx model (Clopath *et al.* 2007). In principle patch-clamp recordings of the response to naturalistic stimuli could be obtained simultaneously from the soma and apical dendrite (Davie *et al.* 2006). Then the dynamic I-V method could be used to fit parameters to an rEIF model of the soma and an alternative IF model of the dendritic compartment.

The second mechanism not captured in the rEIF model is the response of I_{h} channels, which is a hyperpolarisation activated depolarising conductance (Biel *et al.* 2009) and has a half activation potential of between -90 mV and -80 mV in cortical neurons (Spain *et al.* 1987; Harris and Constanti 1995; Biel *et al.* 2009). The effect of this channel manifests itself as a curvature in the cell's I-V relationship at very negative potentials, illustrated by the empirical forcing function (Figure 4.12B main, black points). Since the forcing function of the rEIF model [equation (4.4)] does not

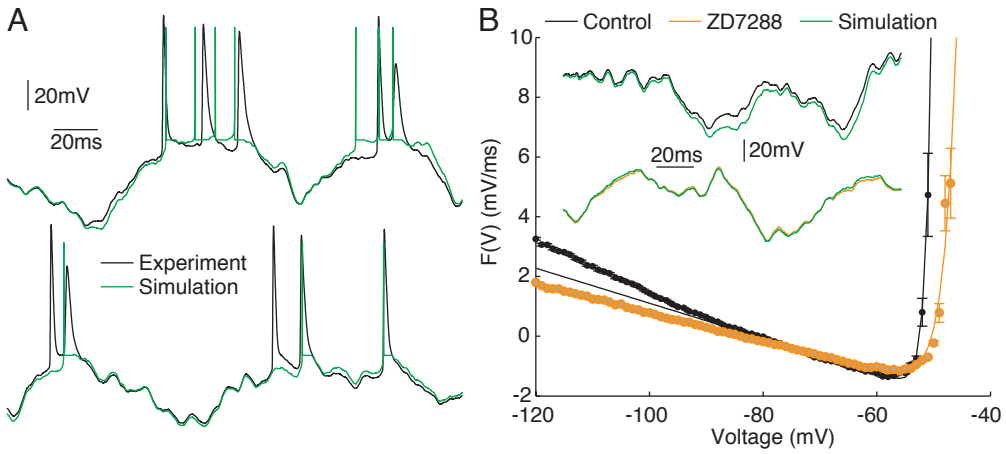

Figure 4.12: The rEIF model fails to well capture the precise timings of bursts of multiple closely spaced action potentials or the membrane potential during periods of strong hyperpolarising input. **A** The rEIF model tends to fire multiple additional action potentials during the bursting period of the cell (top), or miss the burst completely (bottom). **B** *Main*: Empirical (points ± SEM) and fitted forcing function in control (black) and in 25 μM ZD7288 (orange). *Inset*: Response of the cell in control (top) and blocked (orange) states, compared to simulation of the rEIF model (green).

include a term to account for this, the linear ohmic component continues indefinitely at more negative membrane potentials and deviates from the empirical function (Figure 4.12B main, black line).

At very negative membrane potentials (in general less than around -90 mV) this deviation results in a large discrepancy between the experiment and the model simulation (Figure 4.12B inset, top). On blockade with the I_h channel blocker ZD7288 (introduced in Figure 4.9) this curvature is no longer present in the forcing function, which instead displays a linear I-V relationship across the entire range of sub-threshold voltages (Figure 4.12B main, orange). As a consequence the experiment and the model simulation are in good agreement at hyperpolarised membrane potentials (Figure 4.12B inset, bottom).

L2/3 pyramidal cells have a significantly more hyperpolarised resting potential than the other three class (Figure 4.10A) and as a result, during a typical naturalistic stimulus (Figure 2.1B), they spend more time at negative membrane potentials. Since the model always underestimates these voltages this may explain the larger RMSD observed between the model simulation and the experiment in this class (Table 4.2). Including this current into an IF model (for example see Brunel *et al.* 2003) could significantly improve model performance.

4.3.3 Class-dependence of Post-spike Parameter Dynamics

I went on to investigate the between-class differences in post-spike response of the membrane conductance, resting potential, and spike-onset threshold (Figure 4.7). Both the membrane conductance and spike-onset threshold could be described by mono-exponential functions, and the resting potential by a double-exponential of the form of equation (4.6). The membrane conductance of TL5 cells displayed a larger deviation from baseline over the entire response duration than that of the other three cell classes (Figure 4.7A, main). This is to be expected since TL5 cells are significantly larger than other neocortical pyramidal cell classes (Spruston 2008; Oberlaender *et al.* 2012), and so have a far greater membrane surface area. Indeed, on normalising the membrane conductance by membrane capacitance, a value proportional the membrane area, the responses were more similar (Figure 4.7A, inset).

The most marked difference was in the post-spike response of the resting potential (Figure 4.7C). TL5 cells displayed a large post-spike sag, L2/3 cells displayed little or no sag, and the remaining two classes were intermediate. Interestingly, the fitted parameters did not relate to cell class (Figure 4.8A), despite there being a clear class dependence in response shape. Restricting the parameters to an empirically determined trend did not yield any correlation with cell class (Figure 4.8B-E), and neither did implementing a global minimisation algorithm to find the best fitting parameters. This suggests the system is practically non-identifiable, and so the precise values of the parameters do not matter so long as they give the correct response shape. As a result of this property I introduced four new parameters to describe the response of the resting potential: the post-spike jump in the resting potential, E_{jump}; the post-spike time at which the response first crosses below baseline, t_0; and the depth, E_{sag}, and post-spike time, t_{sag}, of the subsequent sag (Figure 4.9A).

In Figure 4.9 I confirmed the previous suggestion (Badel *et al.* 2008a) that the post-spike form of the resting potential in TL5 cells is mediated by I_{h} channels, with the sag occurring due to transient channel inactivation during the spike followed by a gradual re-activation. Blockade with the competitive I_{h} channel antagonist ZD7288

resulted in a mono-exponential response (Figure 4.9B), abolishing or significantly reducing the post-spike sag (Figure 4.9E).

4.3.4 Quantification of Marginal Parameter Distributions

I next quantified heterogeneity in my dataset between the four cell classes with pairwise significance tests (Figure 4.10 left plots). As expected, TL5 cells were separated from the other classes by parameters relating to membrane area, such as a larger capacitance, lower input resistance, and a greater post-spike jump in conductance. More surprisingly, TL5 cells were also well separated from the other classes by their action potential shape, having a larger amplitude (consistent with their lower threshold value, Figure 4.10B), shorter duration, and faster rate of rise (Figure 4.10C). Interestingly, action potential duration was one of only two parameters that distinguished L4 from SL5 cells, the other being the sag response to a hyperpolarising current, despite being located at different cortical depths (Thomson and Lamy 2007), having distinct morphologies (Staiger 2004; Oberlaender *et al.* 2012), and receiving input from different locations (de Kock *et al.* 2007).

Notably, the sag response to step-current input or an action potential increased monotonically from superficial to deep pyramidal cells, with TL5 cells displaying a three fold increase over L2/3 cells. Furthermore, cells could be separated into 'sag' and 'no sag' groups based on the presence or absence of a spike-triggered sag response, respectively. The latter group displayed a mono-exponential response with parameters drawn from class-independent distributions (Figure 4.11).

One of the most striking results of the between-class comparisons was in the excitability measures. There is a monotonic decrease of 14 mV in the potential difference between rest and spike-onset threshold from L2/3 to TL5 cells (Figure 4.10B left), which appears to be primarily determined by the resting potential rather than the absolute spike-onset threshold. Furthermore, on normalisation by the input conductance, yielding the current required to bring the neuron to threshold from rest, L2/3 and TL5 cells were seen to be similarly excitable despite their very different sizes (Oberlaender *et al.* 2012). Both were significantly less excitable than either L4 or SL5 cells (Figure 4.10B right).

Finally, I fitted probability distributions to each parameter measured (Figure 4.10 right plots). Most parameters were well described by a log-normal distribution, as one might expect (Buzsáki and Mizuseki 2014). The resting potential, spike-onset threshold, action potential amplitude, and the sag response of layer 5 cells to a hyperpolarising current were all well fit by normal distributions. The means a standard deviation of the fitted distributions are displayed in Table 4.3. Along with the work presented in the following chapter, I hope that providing these distributions will aid the construction of heterogeneous network models of neocortical pyramidal neurons. Indeed, to the best of my knowledge no work to date has systematically fit reduced neurons models to a number of different cell classes with this aim in mind, although there are a number of methods that have been applied to experimental data as proof of principle (Jolivet *et al.* 2006b; Clopath *et al.* 2007; Kobayashi *et al.* 2009; Yamauchi *et al.* 2011; Mensi *et al.* 2012).

Chapter 5

Heterogeneous Populations of Reduced Neuron Models

5.1 Introduction

Relating the dynamics of distinct neuronal classes to emergent states and ultimately behaviour is currently a key challenge in neuroscience. In addition to the aquisition of large-scale datasets, computational modelling and simulation are essential tools for addressing this (Deco *et al.* 2008; Sporns 2014). Indeed, large-scale network simulations comprising simple spiking neurons can generate responses qualitatively similar to those seen *in vivo* (Lumer *et al.* 1997; Izhikevich and Edelman 2008; Richert *et al.* 2011) and perform simple cognitive tasks (Eliasmith *et al.* 2012). Furthermore, mathematical frameworks have been developed that account for a range of biophysical detail such as synaptic filtering (Brunel and Hakim 1999), synaptic dynamics (Tsodyks *et al.* 1998), voltage- or calcium-gated currents (Richardson *et al.* 2003; Richardson 2009), and spike-frequency adaptation (Schwalger *et al.* 2010). However, thus far efforts have focused primarily on one or several homogeneous populations of neurons, each with identical physiology.

Distinct populations such as the neocortical pyramidal cell classes discussed in Chapter 4 display significant heterogeneity in their electrophysiology (Nowak *et al.* 2003; Zaitsev *et al.* 2012; van Aerde and Feldmeyer 2013; Oswald *et al.* 2013). Recently, there has been increasing theoretical interest in investigating how this

heterogeneity effects the response properties of populations and networks of neurons (Shamir and Sompolinsky 2006; Luccioli and Politi 2010; Alijani and Richardson 2011; Nicola and Campbell 2013; Yim *et al.* 2013; Mejias and Longtin 2014). This is most likely due to the technically challenging nature of the problem combined with the lack of experimental data describing the variance and covariance of cellular properties within and between neuronal classes. The responses of heterogeneous networks are not necessarily the same as equivalent homogeneous networks comprising typical neurons. Indeed, simulation studies have shown that heterogeneities in neuronal physiology leads to differences in synchronisation properties (Maex and De Schutter 2003; Hunsberger *et al.* 2014), coding efficiencies (Chelaru and Dragoi 2008; Padmanabhan and Urban 2010), and gain (Mejias and Longtin 2014) suggesting that further systematic experimental and theoretical study into neuronal heterogeneity is necessary.

Here I continue on from the previous chapter and use more advanced statistical techniques to quantify the heterogeneity both within and between classes of neocortical pyramidal cells, and investigate the sources of this variability. I go on to use unsupervised and supervised machine learning techniques to classify cells based on their electrophysiology alone, and systematically analyse the covariance structure of parameter space. Finally, I provide an algorithm to generate artificial parameter sets of EIF neurons that adhere to the experimentally determined parameter marginal distributions and covariance structure. This algorithm represents a novel tool for investigating heterogeneous networks with experimentally verified parameter distributions, amenable to numerical simulation and theoretical study.

5.2 Results

In this chapter I perform further, more advanced statistical analysis on the dataset I obtained in the previous chapter. The dataset comprised parameter sets from 136 neocortical pyramidal cells from four classes: layer 2/3 (L2/3, $n = 31$); layer 4 (L4, $n = 29$); slender-tufted layer 5 (SL5, $n = 29$); and thick-tufted layer 5 (TL5, $n = 47$). Of the 25 parameters measured (Table 4.1), 18 were taken forward

for further statistical analysis. The parameters omitted were: G_{in}, since this was calculated directly from R_{in} and so its inclusion would add bias to the analysis; E_1, τ_1, E_2, and τ_2, since these parameters didn't well describe the observed dynamics of E (Figure 4.8); and t_{sag} and t_0, since these parameters take infinite values for the subset of cells with a mono-exponential E response (Figure 4.11). To remove bias towards high numerical values, prior to the following analysis I first transformed log-normally distributed parameters (see Table 4.3) into log-space, so that they were normally distributed, followed by taking the Z-score [equation (3.20)].

5.2.1 Variability Between and Within Cell Classes

To determine the major sources of variability in the dataset I used principal component analysis (PCA); a technique that converts a set of correlated variables into linearly uncorrelated components via an orthogonal transformation. This is a useful technique for investigating the sources of variability in a dataset; the first principal component (PC) is the component with the largest variance, the second PC the component with the second largest variance, and so on. This variance allows us to quantify the contribution of a given PC to the overall variability in the dataset. As shown in Figure 5.1A, no small number of principal components (PCs) explained the majority of the variation in the data, with the first four PCs explaining 70% of the variability and 9 of the 18 components were required to explain 90%. Figure 5.1B shows the empirical cumulative distribution functions of the first four PCs. The first PC showed a strong distinction of TL5 cells, and to a lesser extent L2/3 cells from the remaining two classes. The second PC showed a small distinction between cell classes, and the third and fourth PCs did not discriminate.

To understand the cell properties contributing most to the variability in the dataset I looked at the percentage of the variance explained by each variable within each of the first four PCs (Figure 5.1C). The first PC was primarily determined by the steady-state properties of the cell: the sub-threshold properties; distance to spike-onset threshold; and action potential shape; although there was also a significant contribution from the depth of the post-spike sag in the resting potential. The second PC was mainly determined by the spike initiation current, which accounted

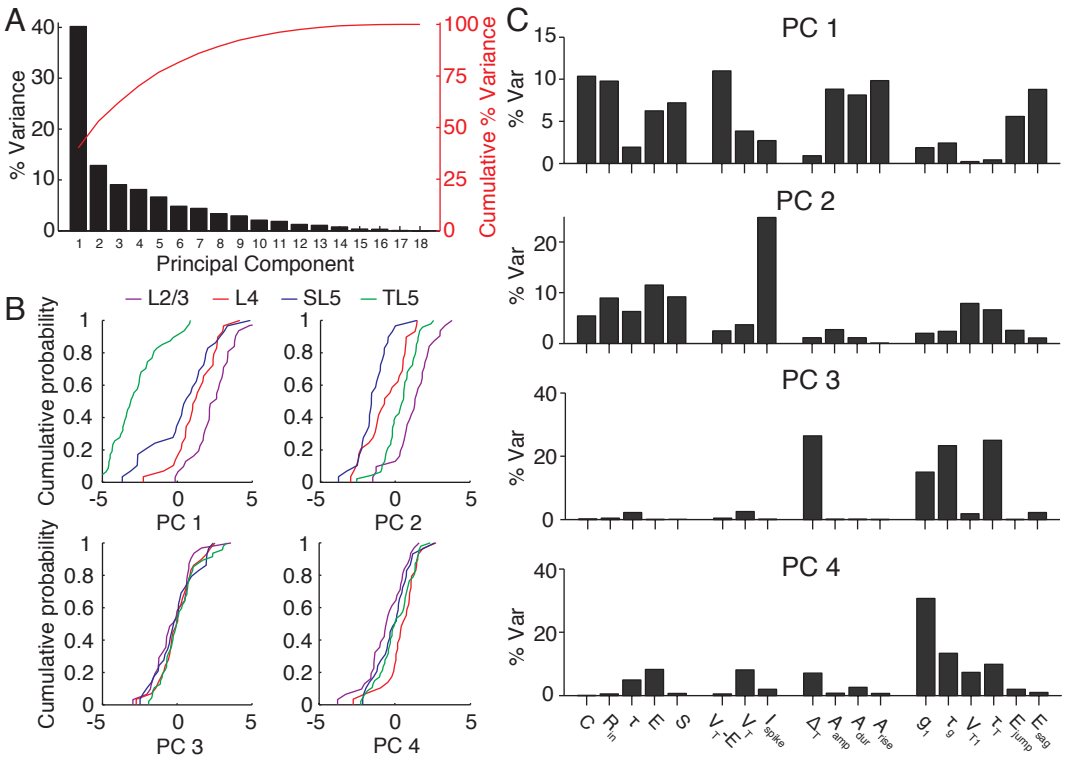

Figure 5.1: Analysis of variation across the dataset shows that the steady-state parameters, in particular the sub-threshold cell parameters, distance to spike-onset threshold, spike initiation current, and action potential shape, along with the post-spike dynamics of the resting potential are the clearest indicators of cell class. **A** Pareto plot of the percentage of the variance explained by each principal component (black bars), and the cumulative sum of the explained variance (red line). **B** Empirical cumulative distribution functions for each class in principal components one to four. **C** Contribution of each parameter to the variance of the first four principal components. Colours indicate layer 2/3 (black), layer 4 (red), slender-tufted layer 5 (blue), and thick-tufted layer 5 (green) neocortical pyramidal cells.

for more than 20% of the variance within this PC. The third PC was determined by the spike sharpness and, similarly to the fourth PC, the post-spike dynamics of the conductance and spike-onset threshold. Together, Figures 5.1B and C indicate that the primary determinants of cortical pyramidal cell class are the steady-state parameters, in particular the sub-threshold cell parameters, distance to spike-onset threshold, spike initiation current, and action potential shape, along with the post-spike sag depth in the resting potential. The spike sharpness and the post-spike dynamics of conductance and spike-onset threshold had far less variability between cell classes, as suggested by pairwise significance tests (Figures 4.10).

To investigate the sources of variability within each cell class I performed PCA on each class separately. The percentage of variance explained by each PC for each

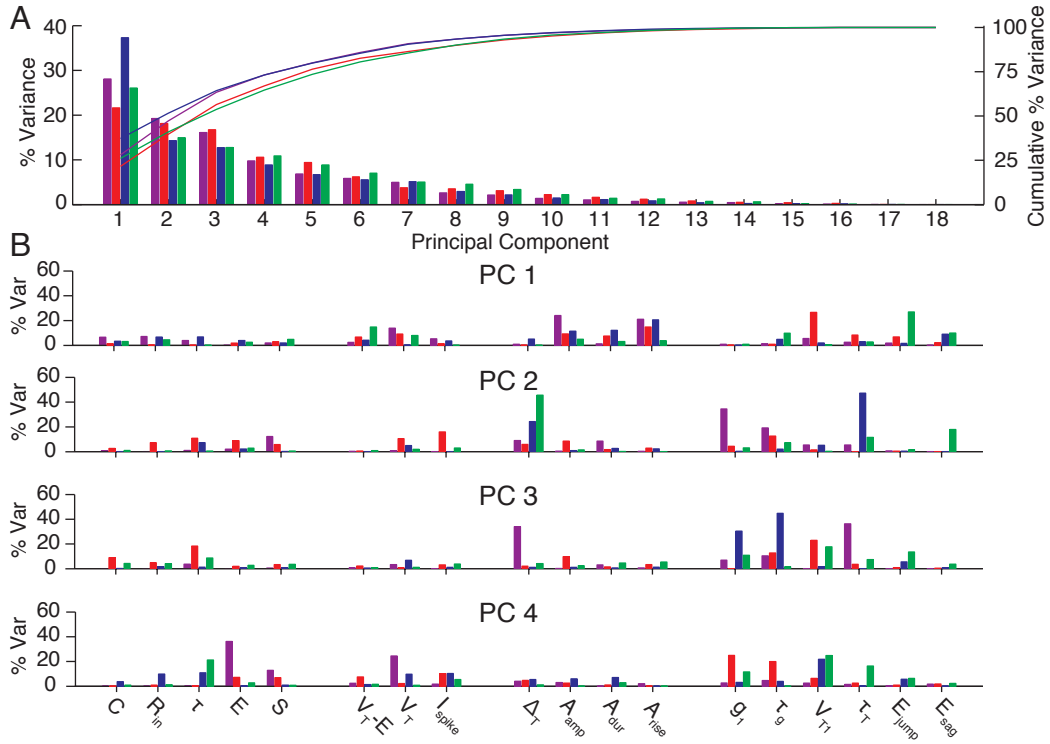

Figure 5.2: Analysis of variation with cell classes indicated that the dynamic post-spike parameters and action potential shape are responsible for the majority of within-class variation. **A** Pareto plot of the percentage of variance explained by each principal component when principal component analysis was performed on each class individually. **B** Contribution of each parameter to the variation of the first four principal components within each cell class individually. Colours indicate layer 2/3 (black), layer 4 (red), slender-tufted layer 5 (blue), and thick-tufted layer 5 (green) neocortical pyramidal cells.

cell class (Figure 5.2A) followed a similar trend to the equivalent result for the whole dataset (*cf.* Figure 5.1A), with the first four PCs explaining 73%, 67%, 73%, and 65% of the variance within L2/3, L4, SL5, and TL5 cells, respectively.

The within PC variation explained by each parameter is shown in Figure 5.2B. The action potential amplitude and rise time along with the post-spike conductance dynamics were the main source of variability within L2/3 cells. The largest contribution to L4 cell variation was the post-spike jump in spike-onset threshold, along with the other post-spike parameters and action potential shape. Similarly to L4, SL5 cells varied most in their post-spike dynamics, particularly the spike-onset threshold decay time constant and action potential shape. Finally, TL5 cells varied most in their post-spike dynamics and spike sharpness parameter.

5.2.2 Discrimination Between Cell Classes

To attempt to discriminate between cell classes based on their elecrophysiological parameters I used a three techniques: Gaussian mixture models, fitted by maximising the model likelihood using the expectation-maximisation algorithm (Dempster *et al.* 1977); linear discriminate analysis, a classification technique that assumes each class is generated by a different Gaussian distribution to fit a linear function to separate classes; and random decision forests, a non-parameteric supervised classification technique where multiple classification trees are trained thus rectifying the problem of overfitting to the training set suffered by a single classification tree (Breiman 2001). The Gaussian mixture models and linear discriminators were fit in PC-space, and the decision forest in normalised parameter space.

Discrimination in PC-space

A scatter plot in PC1-PC2 space showed that L4 and SL5 cells were located in one group (Figure 5.3A, points). A bi-variate Gaussian mixture model with three components showed three clear peaks that separate the distributions of L2/3 and TL5 cells from the combined distribution of L4 and SL5 cells (Figure 5.3, contours); in a four component model a fourth peak was not distinguishable. Furthermore, the three distributions could be well separated using a linear classifier (Figure 5.3A, lines).

After applying PCA to L4 and SL5 cells only the two classes still could not be distinguished in PC space with a two-component Gaussian mixture model (Figure 5.3B). To ensure I had indeed recorded correctly from L4 and SL5 cells I measured their somatic distance from the pial surface (as a ratio of the total neocortical depth, measured as the distance between the pail surface and white matter) of a subset ($n = 84$) of the cells in the dataset. Their somata were indeed located in layer 4 and upper layer 5 (Figure 5.3C) as expected (Oberlaender *et al.* 2012). Together, this implies that it may be more appropriate to model L4 and SL5 cells as having the same distribution, in agreement with pairwise significance tests (Figure 4.10).

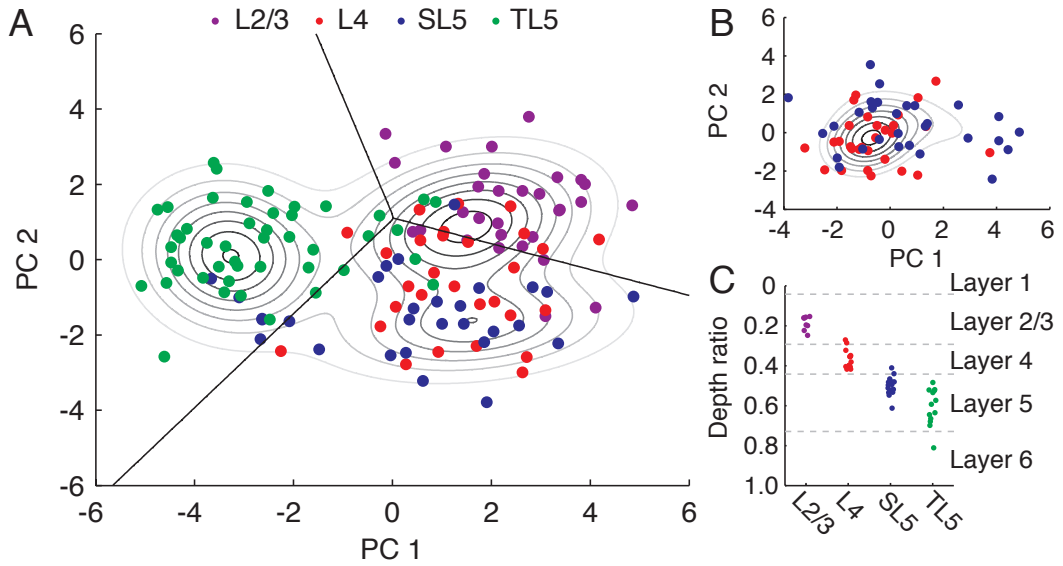

Figure 5.3: Layer 2/3 and thick-tufted layer 5 pyramidal cells separate well in principal component space, but layer 4 and slender-tufted layer 5 pyramidal cells do not. **A** Scatter plot of cell locations in PC1-PC2 space, where coloured points denote class. Contours denote a fitted three component bi-variate Gaussian mixture model, and black lines denote linear discriminate functions. **B** A fitted two-component bi-variate Gaussian mixture model in PC1-PC2 space of principal component analysis performed on layer 4 and slender-tufted layer 5 cells only. **C** Laminar location of a subset of cells from the dataset ($n = 84$) as a ratio of cortical depth. Layer boundaries obtained from Meyer *et al.* (2010).

Discrimination Using Random Decision Forests

Another commonly used machine learning tool for classification problems is a random forest (Breiman 2001), which is a non-parametric supervised learning method based on the theory of classification trees and bootstrap sampling (referred to as bagging). A complete description of random decision forests is given in Section 3.8, and will be briefly summarised here. A random decision forest comprises many individual classification trees that are each trained on a bootstrapped sample of the dataset. During classification each tree in the forest classifies the object independently, or 'votes' for the class. The forest output is then the class with the most votes. When training each tree the best split at a node is determined by minimising Gini's diversity index, given in equation (3.21), at each of the two child nodes. At each node a random subset of m parameters is used to calculate the best split. Here, since my dataset is relatively small, I trained a forest with m varying from 1 to 18 (all parameters), and found $m = 4$ gave the smallest forest error rate.

The objects (i.e. cells) not used for training a tree are referred to as out-of-bag

(OOB). These can be used to calculate an unbiased estimator of the forest error rate, the OOB error rate, as described in Section 3.8. Although cross-validation is not strictly required when constructing a random decision forest as one can measure the OOB error rate (Breiman 2001), this is standard practice in the field of machine learning and so will be performed here. For each model I grew 1000 independent random decision forests, each trained with a random 80% of the dataset. The error rate could then be calculated from the remaining 20% of data for each forest and averaged. I chose to grow 1000 forests since this was just past the point at which adding more forests did not decrease the variance in the error rate across the population.

Next, I compare the error rate calculated from cross-validation with the OOB error. Initially, after only a few trees have been grown the forest error rate is high, but eventually asymptotes to a minimum value after approximately 200 trees, after which point adding extra trees to the forest will not provide any further predictive power (Figure 5.4A, main). The mean cross-validation error rate from 1000 independently grown decision forests, each consisting of 200 trees was 0.34, which was not significantly different from the error predicted using the OOB error estimate ($p = 0.74$). Although this validates the use of the OOB error, since it is best practice in machine learning to use cross-validation, error rates quoted henceforth will be calculated in this manner.

To investigate the cause of this classification error I examined the error rate within each cell class. These error rates were 0.24, 0.69, 0.41, and 0.11 for L2/3, L4, SL5, and TL5 respectively (Figure 5.4A, inset), indicating the forest well classifies L2/3 and TL5 cells but fails to accurately distinguish between L4 and SL5. This is to be expected as pairwise significance tests showed only two parameters distinguished between the latter two classes (Figure 4.10) and they can be modelled by a single distribution (Figure 5.3). When L4 and SL5 cells were combined into a single class the mean error rate reduced to 0.17 (Figure 5.4B) and the new class error rates were 0.24, 0.15, and 0.10 for L2/3, L4/SL5, and TL5 cells, respectively (Figure 5.4C).

One useful feature of random forests is that they can be used to determine the parameters in the dataset most important for classification. Put simply, to calculate

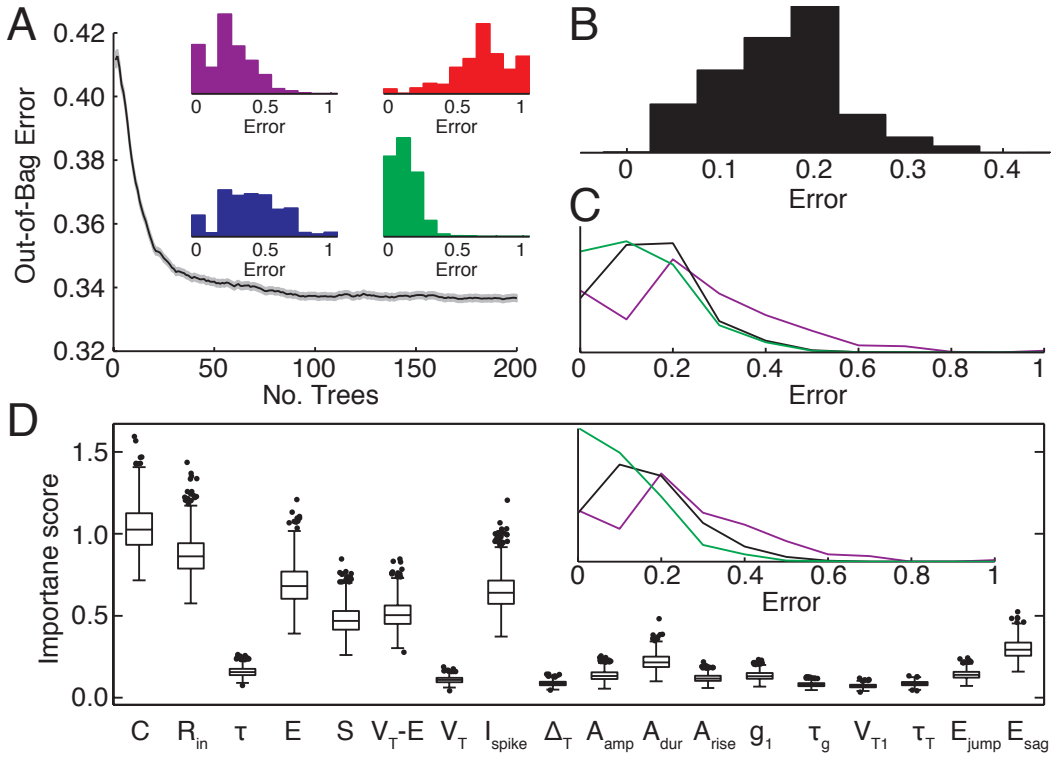

Figure 5.4: Random decision forests correctly predict cell class with 83% accuracy. **A** *Main:* Out-of-bag error rate as a function of the number of trees in the forest is an unbiased predictor of the true error rate. Mean out-of-bag error over 1000 independent random forests each consisting of 200 trees (black line) ± SEM (shaded region). *Inset:* Error rate distributions for (from top left to bottom right) layer 2/3 (L2/3, purple), layer 4 (L4, red), slender-tufted layer 5 (SL5, blue), and thick-tufted layer 5 (TL5, green) pyramidal cells, respectively. **B** Distribution of error rates after L4 and SL5 cells had been combined into a single class. (Mean error rate 0.17 and standard deviation 0.063). **C** Distributions of within-class error rates. Mean and standard deviation of error rates (μ, σ): (0.24, 0.18), (0.15, 0.11), and (0.13, 0.11) for L2/3 (purple), L4/SL5 (black), and TL5 (green) cells, respectively. **D** *Main:* Importance of each parameter used in the classification by measuring the importance score (see Section 3.8) after randomising each variable in turn and re-growing the forest. *Inset:* Distribution of error rates of 1000 independent decision forests comprising 200 trees grown using only the six most important parameters (C, R_{in}, E, S, $V_{\text{T}} - E$, and I_{spike}). Mean and standard deviation, (μ, σ), of the total error rate was (0.16, 0.066) and of each class was (0.25, 0.18), (0.16, 0.11), and (0.10, 0.11) for L2/3, L4/SL5, and TL5 cells respectively.

the importance of parameter k the error rate of the original forest is compared with that of a forest trained with parameter k randomly permuted. This process and the calculation of the importance score is explained in full in Section 3.8. Figure 5.4D shows the importance of each parameter across the dataset. There are six parameters that contribute significantly more to correct classification, which are the membrane capacitance, input resistance, resting potential, the sag response to a hyperpolarising current, the distance between rest and spike-onset threshold, and the spike initiation

current, in agreement with pairwise significance tests (Figure 4.10) and principal component analysis (Figure 5.1). However, if only these six parameters were used to grow and test the decision forest the error rate was not reduced. For L2/3 and L4/SL5 cells the error rate increased to 0.25 and 0.16, respectively, although these were non-significant increases at the 5% level. The error rate for TL5 cells decreased significantly ($p < 10^{-8}$) to 0.10.

5.2.3 Covariance of Neuronal Parameters

To examine important dependencies I calculated the covariance and Spearman's rank correlation coefficient [defined in equation (3.22)] for all parameter pairs in the dataset. Six parameter pairs displayed a significant correlation ($|\rho| > 0.75$), as illustrated in Figure 5.5A. The strongest correlation was between capacitance and input conductance (Figure 5.5B, $\rho = 0.93$), which was unsurprising since both are related to membrane surface area and are approximately proportional to the density of ion channels. There were two strong correlations between action potential shape parameters: amplitude and rate of rise (Figure 5.5C, $\rho = 0.83$), and duration and rate of rise (Figure 5.5G, $\rho = -0.77$). Strong correlations in these parameters are to be expected given their dependence on the spike generating sodium and rectifying potassium currents (Bean 2007). It is worth noting that the correlation between action potential duration and rate of rise is significantly weaker in L4 cells ($\rho = -0.33$) than in the other three classes ($\rho = -0.61$, -0.81, and -0.73 for L2/3, SL5, and TL5 cells, respectively).

The correlation between the spike initiation current (defined as $I_{\text{spike}} = (V_{\text{T}} - E)G_{\text{in}}$) and the input conductance (Figure 5.5D, $\rho = 0.82$) is less trivial as it suggests that the distance to spike-onset threshold from rest is not modified to compensate for cell size. The exception is TL5 cells, which display a comparable value of I_{spike} to L2/3 cells but at much higher conductances (*cf.* Figure 4.10B). The negative correlation between the distance to spike-onset threshold and resting potential (Figure 5.5E, $\rho = -0.80$) is a consequence of the weak variability in V_{T}, which has a variance of $16\,\text{mV}^2$ compared to resting potential variance of $34\,\text{mV}^2$. For the same reason the distance to spike-onset threshold also anti-correlates strongly with the sag

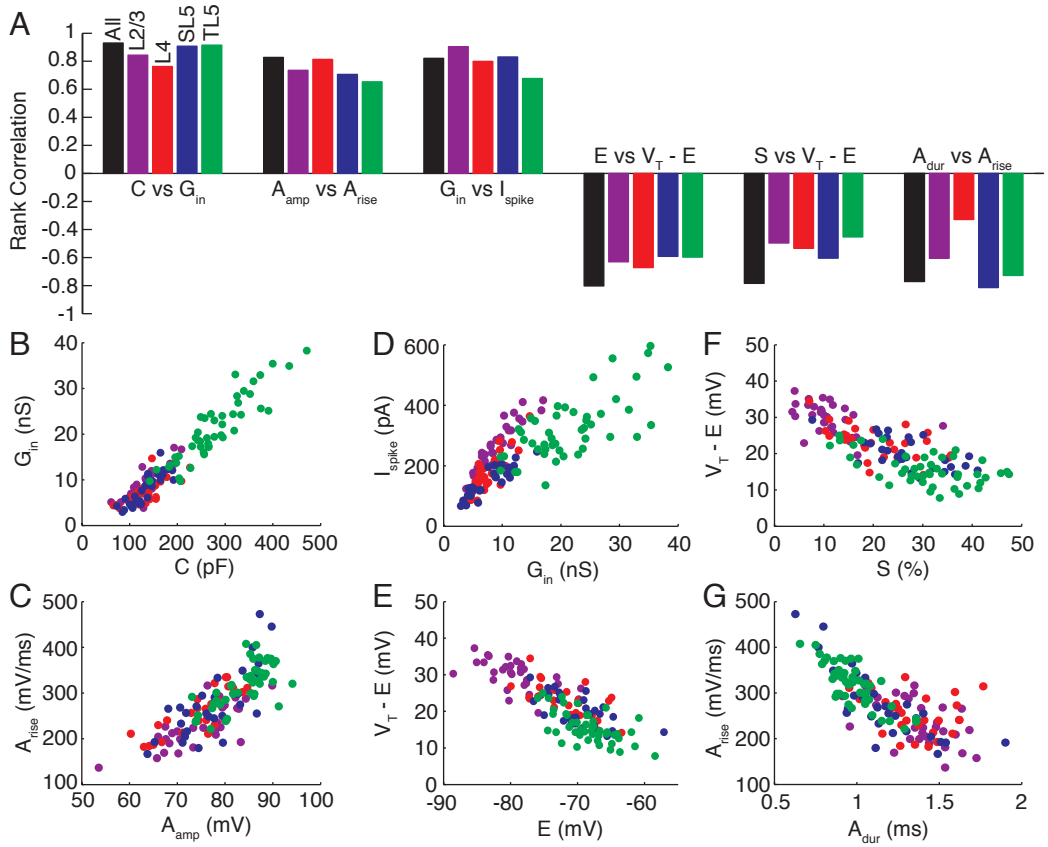

Figure 5.5: Correlations in electrophysiological parameters. **A** The most correlated ($|\rho| > 0.75$) pairs of parameters for all (black), layer 2/3 (purple), layer 4 (red), slender-tufted layer 5 (blue), and thick-tufted layer 5 (green) pyramidal cells. **B-G** Scatter plots of the most strongly correlated parameters shown in A.

percentage in response to a hyperpolarising current step (Figure 5.5F, $\rho = -0.78$). This is effectively a positive correlation with the resting potential - E and S have a correlation coefficient of 0.71 - consistent with the role of I_{h} channels in depolarising the resting potential and deepening the sag response. Notably, the correlation coefficients for each class separately of E vs. V_{T} (-0.63 -0.67 -0.59 -0.60 for L2/3, L4, SL5, and TL5 cells, respectively) and E vs. S (-0.50, -0.53, -0.60, -0.45 for L2/3, L4, SL5, and TL5 cells, respectively) were lower than that of the entire dataset (Figure 5.5A).

The covariance matrices of the standard EIF model parameters C, E, τ, Δ_{T}, and V_{T}, for each of the four cell classes are tabulated in Table 5.1, with the values for the full parameter set being contained in the model generation algorithms provided in Appendices B and C.

Table 5.1: Covariance matrices of exponential integrate-and-fire model parameters C (pF), τ (ms), E (mV), Δ_T (mV), and V_T (mV) for each of the four cell classes.

	Layer 2/3					**Layer 4**				
	C	τ	E	V_T	Δ_T	C	τ	E	V_T	Δ_T
C	1078	-27.9	-1.59	-75.6	-2.71	1346	38.1	37.5	-29.2	-1.77
τ	-27.9	6.38	-1.23	4.00	-0.560	38.1	17.4	5.16	-0.685	-0.0601
E	-1.59	-1.23	18.3	7.76	-0.0720	37.5	5.16	17.6	5.07	-0.485
V_T	-75.6	4.00	7.76	14.5	-0.380	-29.2	-0.685	5.07	12.5	-0.463
Δ_T	-2.71	-0.560	-0.0720	-0.380	0.302	-1.77	-0.0601	-0.485	-0.463	0.155

	Slender-tufted layer 5					**Thick-tufted layer 5**				
C	1017	59.3	57.5	-24.5	-3.86	6161	-7.44	37.6	-70.9	-8.07
τ	59.3	22.4	5.95	-0.715	-0.544	-7.44	17.9	0.383	-0.581	-0.413
E	57.5	5.95	17.5	5.91	-0.944	37.6	0.383	15.8	5.33	0.215
V_T	-24.5	-0.715	5.91	12.6	-0.334	-70.9	-0.581	5.33	12.9	0.198
Δ_T	-3.86	-0.544	-0.944	-0.334	0.274	-8.07	-0.413	0.215	0.198	0.229

5.2.4 Generation of EIF and rEIF Model Parameter Sets

The primary aim of this chapter was to provide an algorithm to generate a set of integrate-and-fire neurons that have experimentally verified marginal distributions and parameter covariance structure. I provide two algorithms, one to generate parameter sets for the standard EIF model (Fourcaud-Trocmé *et al.* 2003) comprising parameters C, E, τ, Δ_T, and V_T, and one to generate parameter sets for the rEIF model (Badel *et al.* 2008a), which has the additional parameters describing the refractory dynamics of E, $g = C/\tau$, and V_T (Figure 4.7).

Since most of the parameters required for the EIF and rEIF models did not have Gaussian marginal distributions (Figure 4.10) I had to use a method of fitting a multivariate distribution independent of the marginal form whilst maintaining the covariance structure. To do this I defined a Gaussian copula distribution $C(x_1, \ldots, x_n)$, which is a distribution describing the correlation structure in the data set. This is combined with the marginal distributions of each parameter x_i, given by $p(x_i)$, to define the multivariate probability distribution function in the entire parameter space:

$$p(x_1, \ldots, x_n) = C(x_1, \ldots, x_n) \prod_{i=1}^{n} p(x_i), \tag{5.1}$$

where n is the number of parameters in the model.

The process of fitting a copula distribution is as follows. First, the multivari-

ate dataset is transformed to the unit hypercube via the cumulative distribution functions of its marginal distributions. The transformed dataset now has uniformly distributed marginals but the correlation structure remains. Next, a Gaussian copula is fit to the transformed data, from which a random sample can be drawn. Finally, the random sample is transformed back to the scale of the original dataset via the inverse cumulative distribution functions of its marginals. The result is a random sample taken from the distribution $p(x_1, \ldots, x_n)$, as defined in equation (5.1), which has the marginal distributions and correlation structure of the original dataset.

The algorithm to generate a population of EIF neurons follows the above procedure on the five-dimensional space comprising parameters C, E, τ, Δ_{T}, and V_{T}. However, generating populations of rEIF models is more involved due to complications with including the post-spike dynamics of the resting potential. The parameters describing this post-spike response, E_{jump}, E_{sag}, t_0, and t_{sag} (Figure 4.9A), are insufficient if one wants to numerically simulate the response of the generated population; one requires the parameters of the double-exponential function describing the response. As I showed in Chapter 4, the fitted double-exponential parameters do not relate to cell class (Figure 4.8A). Furthermore, some cells display a post-spike sag whilst others do not, but rather are described by a mono exponential with parameters E_{mono} and τ_{mono} (Figure 4.11).

To deal with these complications I noted that E_{jump}, E_{sag}, t_0, t_{sag}, E_{mono}, and τ_{mono} do not correlate strongly with the other parameters required for the rEIF model, namely C, E, τ, Δ_{T}, V_{T}, g_1, τ_g, V_{T1}, and τ_{T}. This allows the latter parameters to be generated independently using the procedure outlined above, followed by independently generating the parameters describing the post-spike E dynamics. The algorithm proceeds as follows:

1. Generate parameter sets of the parameters C, E, τ, Δ_{T}, V_{T}, g_1, τ_g, V_{T1}, and τ_{T} using the copula method described above.
2. To each parameter set randomly assign a tag denoting 'sag' or 'no sag', adhering to the empirical probabilities in Figure 4.11A.
3. Let N denote the number of parameter sets tagged as 'sag', and M denote the number tagged with 'no sag'.

4. Generate M parameter sets of the parameters E_{mono} and τ_{mono} (whose marginal distributions are shown in Figure 4.11B) using the copula method described above.
5. Randomly assign these parameter sets to the 'no sag' group.
6. Generate N parameter sets of the parameters E_{jump}, E_{sag}, t_0, and t_{sag} (whose marginal distributions are shown in Figure 4.10D) using the copula method described above.
7. To each parameter set fit a double exponential function of the form

$$E(t) = -E_1 e^{-(t-t_{\text{ref}})/\tau_1} + E_2 e^{-(t-t_{\text{ref}})/\tau_2}, \tag{5.2}$$

where t_{ref} is the refractory period and t is the time since the spike peak, to the points $(0,\ E_{\text{jump}})$, $(t_0,\ 0)$, $(t_{\text{sag}},\ -E_{\text{sag}})$, as illustrated in Figure 5.6. This fit is subject to the following constraints:

$$E_2 > E_1, \tag{5.3a}$$

$$\tau_1 > \tau_2, \tag{5.3b}$$

$$\alpha < 1, \tag{5.3c}$$

$$\frac{E_1}{\tau_1^2}\alpha^{\frac{-\tau_2}{\tau_2-\tau_1}} < \frac{E_2}{\tau_2^2}\alpha^{\frac{-\tau_1}{\tau_2-\tau_1}}, \tag{5.3d}$$

$$E_{\text{jump}} = E_2 - E_1, \tag{5.3e}$$

$$E_{\text{sag}} = E_1\alpha^{\frac{-\tau_2}{\tau_2-\tau_1}} - E_2\alpha^{\frac{-\tau_1}{\tau_2-\tau_1}}, \tag{5.3f}$$

$$t_{\text{sag}} = \frac{\tau_1\tau_2 \ln\alpha}{\tau_2 - \tau_1}, \tag{5.3g}$$

where $\alpha = E_1\tau_2/E_2\tau_1$ is a non-dimensional parameter. Note that these relationships cannot be inverted to calculate E_1, τ_1, E_2, and τ_2 from E_{jump}, E_{sag}, t_0, and t_{sag}, necessitating a fitting approach.
8. Randomly assign these parameter sets to the 'sag' group.

In Figure 5.7 I demonstrate the algorithm by generating 1000 model cells of each class. The correlation structure in the simulated data set and the marginal

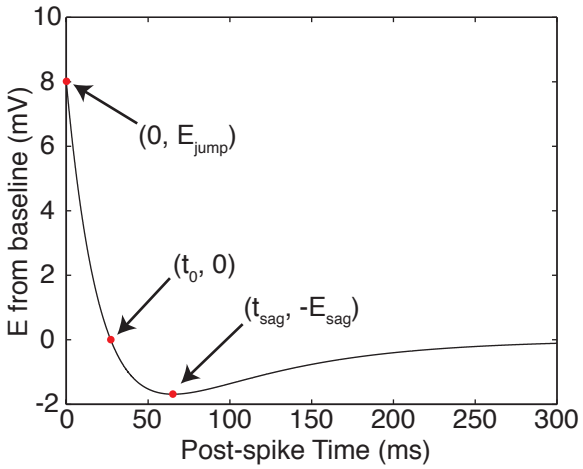

Figure 5.6: As part of the algorithm to generate parameter sets for the rEIF model, sets of the parameters describing the bi-exponential post-spike E dynamics (E_{jump}, E_{sag}, t_0, and t_{sag}) are first generated, then used to fit the double exponential parameters of equation (5.2) subject to the constraints in equations (5.3).

distributions were adhered to, for example in E vs. $V_{\text{T}} - E$ space (Figure 5.7A top) and C vs. $V_{\text{T}} - E$ space (Figure 5.7A bottom). Furthermore, the mean refractory response of g, V_{T}, and E were indistinguishable from the mean responses of the real cells in the dataset (Figure 5.7B). MATLAB code for the EIF and rEIF algorithms are provided in Appendices B and C, respectively. Note that these functions contain the necessary fitted marginal and copula distribution parameters and so are self-contained, without requiring my experimental dataset and can be freely distributed.

5.3 Discussion

In this chapter I extended my analysis of the dataset used in Chapter 4, determining sources of between- and within-class variability and examining the covariance structure of parameter space. Using PCA I determined the primary sources of between-class variability to be the steady-state parameters, namely the sub-threshold parameters, cell excitability at rest, and action potential shape; a significant contribution was also made by the post-spike sag in the resting potential (Figures 5.1B and C). The parameters contributing most to the within-class variation differed between cell classes, although the strongest contributors were generally the post-spike dynamics

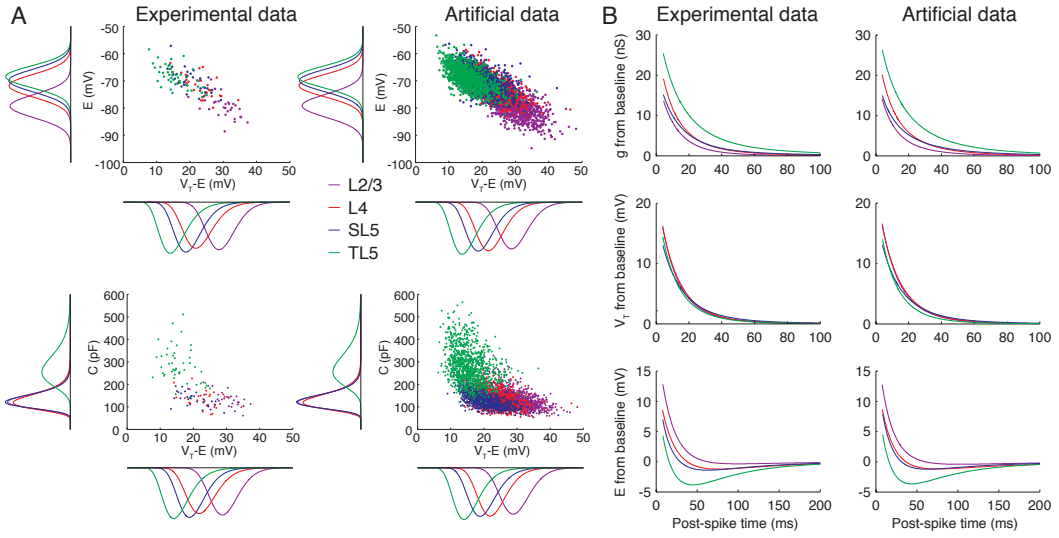

Figure 5.7: Output of the algorithm to simulate artificial pyramidal cells from neocortical layers 2/3, 4, and 5 that respect the marginal distributions and correlation structure of the experimental dataset. **A** Relationship between E and $V_{\mathrm{T}} - E$ (top), and C and $V_{\mathrm{T}} - E$ (bottom) in the experimental (left) and artificial (right) datasets. **B** Mean responses of the post-spike dynamics of g, V_{T}, and E in the experimental and artificial datasets. The simulated dataset consisted of 1000 cells in each of the four classes.

of the conductance, resting potential, and spike-onset threshold (Figure 5.2B). L2/3 and TL5 cells separated well in principal component space (Figure 5.3A); however, L4 and SL5 comprised a single distribution (Figure 5.3B) despite being located at different cortical depths (Thomson and Lamy 2007, Figure 5.3C), having distinct morphologies (Staiger 2004; Oberlaender *et al.* 2012), and receiving input from different locations (de Kock *et al.* 2007). Classifying cells using random decision forests supported these results, with the error rate reducing dramatically once L4 and SL5 cells were combined into a single class (Figure 5.4). On examination of the parameter covariation the main non-trivial correlations arose from effects common to the I_{h} current, such as a depolarised resting potential and strong sag response (Figure 5.5).

Finally, I provide a MATLAB implementation of algorithms to generate EIF and rEIF model parameter sets (Appendices B and C, respectively) for L2/3, L4, SL5, and TL5 pyramidal cells, adhering to the respective experimentally determined variance and covariance structure. This is a novel tool enabling further mathematical investigation into neocortical-network heterogeneity.

5.3.1 Variability in Cell Electrophysiology Across the Neocortex

I concluded Chapter 4 by investigating the between-class parameter variation, determining statistically significant differences between L2/3, L4, SL5, and TL5 pyramidal cells (Figure 4.10). In this chapter I used PCA to conduct a more in depth analysis of cell variability, investigating the parameters contributing most to the variance both between and within cell classes. In PC space it was TL5 cells that separated most decisively and to a lesser extent L2/3 cells, with significant overlap between L4 and SL5 cells (Figure 5.3B). I found that over the entire dataset most of the variance was explained by the steady-state parameters: the sub-threshold parameters, distance to spike-onset threshold, spike initiation current and action potential shape. Dynamic quantities also contributed to the overall variance, with a significant amount attributed to the post-spike sag in the resting potential, and a small amount to the refractory dynamics of the spike-onset threshold (Figure 5.1C).

To investigate the properties responsible for within-class variability I performed PCA on each class separately. Generally, the parameters contributing most to the variance in each class were those describing the post-spike behaviour, along with the action potential shape, albeit to a lesser degree (Figure 5.3E). Together, these results suggest that TL5 cells, and to a lesser extent L2/3 can be distinguished by their steady-state properties and resting potential dynamics, in agreement with pairwise significant tests (Figure 4.10) and previous findings from the medial prefrontal cortex (van Aerde and Feldmeyer 2013).

5.3.2 Layer 4 and Slender-tufted Layer 5 Cells Comprise a Single Electrophysiological Population

In Chapter 4 I found that only two parameters distinguished between L4 and SL5 cells: the sag response to a hyperpolarising current step and the action potential duration (Figure 4.10). To further investigate this finding I used a combination of Gaussian mixture modelling and linear discriminant analysis. In PC1-PC2 space L2/3 and TL5 cells were well captured by two components of a three-component Gaussian mixture model, with the latter class the most clearly separated (Fig-

ure 5.3A). However, L4 and SL5 cells were well modelled by a single component of the three-component model. Indeed, adding an extra component did not result in a clear additional peak, and when PCA was performed on L4 and SL5 only, a two-component bi-variate Gaussian showed only a single peak (Figure 5.3B). This result was confirmed by linear discriminant analysis, which well separated L2/3 and TL5 cells from the combined distribution of L4 and SL5 cells (Figure 5.3A).

To further investigate this finding I used random decision forests to perform a supervised classification on the dataset. Initially, keeping L4 and SL5 cells as separate classes during forest training the method performed poorly, with 33% of cells erroneously classified during testing. The majority of this error is a result of misclassification of L4 and SL5 cells (Figure 5.4A inset). Indeed, after grouping L4 and SL5 cells into a single class the overall performance improved dramatically, with 83% of cells correctly classified (Figure 5.4B). This was an unexpected result since L4 and SL5 cells make up distinct neuronal populations in terms of their location (Thomson and Lamy 2007, Figure 5.3C), morphology (Staiger 2004; Oberlaender *et al.* 2012), and their synaptic input (de Kock *et al.* 2007), suggesting that my dataset may not include the necessary parameters to distinguish between these cell classes. Furthermore, random forests allow for the determination of parameters most important for classification by re-training the forest with one parameter randomised and quantifying the resulting reduced classification ability. This procedure confirmed the results of pairwise significance tests (Figure 4.10) and PCA (Figure 5.1) that the primary determinants of neuronal class were the steady-state parameters and cell excitability, although the action potential shape was deemed far less important (Figure 5.4D).

5.3.3 Consequences for Modelling Populations of Neocortical Pyramidal Cells

Simulation studies have suggested that heterogeneity within neuronal populations is a necessary feature for biologically relevant network models (Maex and De Schutter 2003; Chelaru and Dragoi 2008), and including empirically determined variance and covariance of the relevant parameters is a prerequisite of this. Investigating the

strongest ($\rho > 0.75$) correlations in our dataset revealed some trivial relationships, such as that between the capacitance and input conductance, both of which are largely determined by membrane surface area and the spatial density of channel expression. There were two strong non-trivial relationships in the dataset, both of which were consequences of effects common to the I_{h} current. The first was between the spike-initiation current and input conductance (Figure 5.5D), which suggests that the distance to spike-onset threshold in neocortical pyramidal cells is not adjusted to compensate for cell size; the distance to spike-onset threshold is primarily determined by the resting potential, of which I_{h} current is a strong determinant, rather than the absolute spike-onset threshold value. The second was between the distance to spike-onset threshold and sag percentage (Figure 5.5F), which is effectively a correlation between the resting potential and sag strength, both of which correlate with I_{h} current (Momin *et al.* 2008; Biel *et al.* 2009).

Finally, the primary outcome of this chapter was to provide a tool to aid the exploration of heterogeneity in network models of neocortical microcircuits. The novel algorithm presented here for generating artificial datasets adheres to the experimentally determined marginal distributions and covariance structure of parameter space (Figure 5.7). Coupling this work with other studies quantifying synaptic connectivity and network topology will allow models to be constructed in which the within-class heterogeneities and layered structure of the neocortex are conserved. Such models will greatly contribute to our understanding of how network architecture affects how cortical microcircuits process information.

Chapter 6

Threshold Variability in Thick-tufted Layer 5 Pyramidal Cells

6.1 Introduction

Action potentials are triggered once a neuron has received sufficient synaptic input to be depolarised above threshold. However, this threshold is dynamic (Azouz and Gray 2000, 2003; de Polavieja 2005) and strongly correlated with the recent voltage history (Azouz and Gray 2000, 2003; Higgs and Spain 2011) and time since the last spike (Badel *et al.* 2008a,b). In Chapter 4 I showed that, in neocortical pyramidal cells, the spike-onset threshold can jump by approximately 15 mV after an action potential and subsequently decays back to its baseline value over a period of tens of milliseconds (Figure 4.7B). Furthermore, the threshold has been shown to accumulate as a result of increased recent spiking activity in pyramidal cells of the rodent hippocampus (Henze and Buzsáki 2001) and electrosensory lateral line lobe of the weakly electric fish (Chacron *et al.* 2007), and modelling studies have shown that a spike-triggered jump and subsequent threshold decay leads to experimentally observed computational properties, such as negative inter-spike interval (ISI) correlations (Chacron *et al.* 2001, 2003) and spike-frequency adaptation (Chacron *et al.*

2003). The simple monoexponential decay has also been extended to include multiple time scales (Kobayashi *et al.* 2009) and voltage dependence (Yamauchi *et al.* 2011), allowing the capture of more complicated firing patterns such as intrinsic bursting, chattering, and post-inhibitory rebound spiking.

In this chapter I investigate post-spike threshold dynamics focussing on the response of neocortical thick-tufted layer 5 pyramidal cells (TL5). I look at three extensions to the standard EIF model that attempt to capture experimentally observed post-spike threshold dynamics and compare their ability to mimic the response of TL5 pyramidal cells using the performance metrics introduced in Chapter 4. The first is the rEIF model introduced by Badel *et al.* (2008a), which well captures the response of pyramidal cells across the neocortex (Chapter 4). Although this model performs well it makes no attempt to capture the threshold accumulation seen in experiments (Henze and Buzsáki 2001; Chacron *et al.* 2007). To address this, I quantify the degree to which spike threshold accumulates as a function of the preceding inter-spike interval using experimental data. I use this to extend the rEIF model, leading to the Accumulating Threshold rEIF (ATrEIF) model. The third model is the Two-variable EIF (2vEIF) model, suggested by Badel *et al.* (2008b) due to its experimental relevance combined with its mathematical tractability. This is a two variable system consisting of the standard EIF model voltage dynamics coupled with the same refractory spike-onset threshold dynamics of the rEIF model. I compare the performance of the four models in replicating the response of the cell to novel stimuli not used for model fitting. I make two key findings: the addition of a non-renewal process accumulating threshold did not significantly improve the rEIF model; and the 2vEIF model performs worse than the rEIF and ETrEIF model, indicating the importance of the inclusion of a dynamic resting potential and membrane time constant, but performs significantly better than the standard EIF model with only a small increase in mathematical complexity.

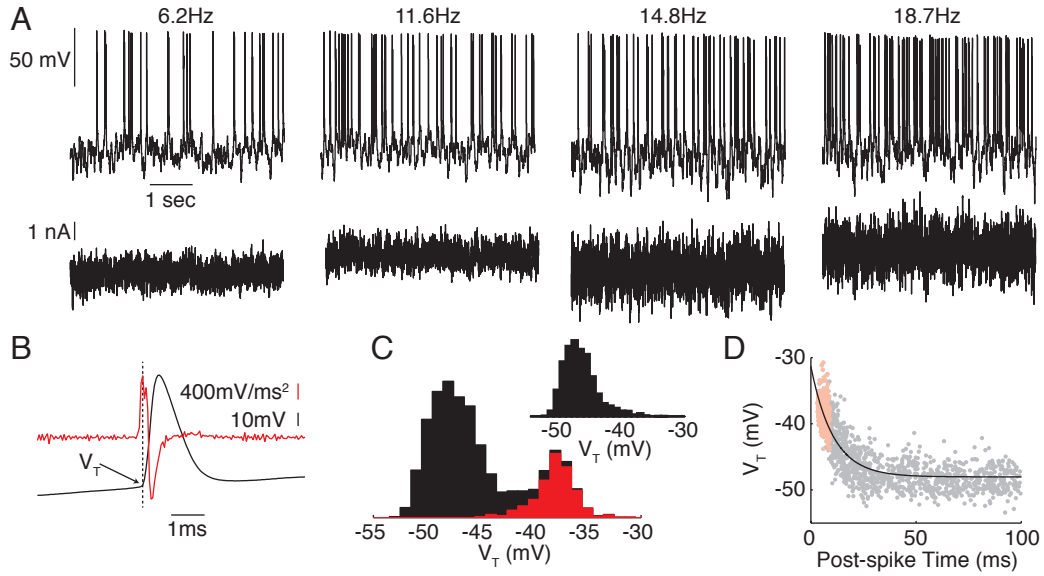

Figure 6.1: Quantification of spike-initiation threshold of a thick-tufted layer 5 pyramidal cell during naturalistic stimuli. **A** Responses of a thick-tufted layer 5 pyramidal cell (top) to four distinct naturalistic current injections (bottom), firing at 6-19Hz. **B** Second derivative threshold method used to determine spike-initiation threshold V_{T} for each spike (black: V, red: $\mathrm{d}^2V/\mathrm{d}t^2$). **C** *Main:* Histogram of V_{T} across four distinct recordings of naturalistic stimulation (2047 spikes). Black histogram is of all spikes, red histogram is burst spikes only, which were defined as those where the membrane potential after the preceding spike did not fall below the baseline threshold value, determined by fitting the pre-spike dynamic I-V curve, before spiking again *Inset:* Histogram of V_{T} with burst spikes removed (1603 spikes). This distribution fit to a skew-normal distribution with location parameter $\xi = -50.4\,\mathrm{mV}$, scale parameter $\omega = 4.44\,\mathrm{mV}$, and shape parameter $\alpha = 4.05$. **D** Spike-initiation threshold plotted against time since the last spike (points) including normal (grey) and burst (red) spikes, with a mono-exponential fit (line).

6.2 Results

The dynamic I-V method measures the average spike-onset threshold response during a naturalistic stimuli (Chapter 4). However, for a more detailed quantification I measured the threshold for individual spikes from a series of naturalistic stimuli at a range of firing rates (Figure 6.1A). To do this I use the second derivative method, which measures the peak in the voltage second derivative corresponding to the 'kink' in somatic voltage at spike-initiation (Figure 6.1B, Sekerli *et al.* 2004).

A histogram of spike-initiation threshold values displayed a bi-modal distribution with the right hand peak consisting mainly of burst spikes (Figure 6.1C main), which occur frequently in TL5 cells (Connors *et al.* 1982; Montoro *et al.* 1988; Chagnac-Amitai *et al.* 1990; Connors and Gutnick 1990). Removing burst spikes gives a skew-normal distribution skewed towards more depolarised threshold values (Figure 6.1C

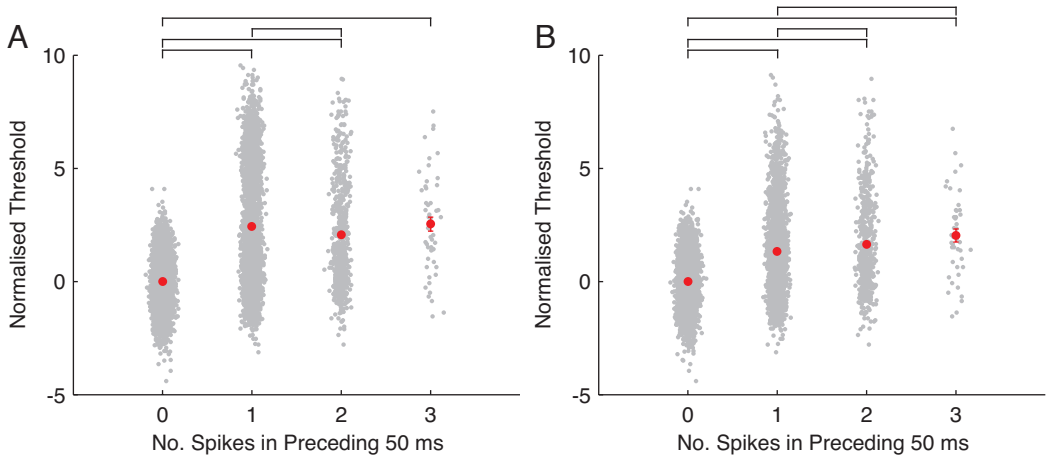

Figure 6.2: Variability in spike-initiation threshold due to an increasing number of spikes in the preceding 50 ms for thick-tufted layer 5 pyramidal cells **A** including (9821 spikes from 6 cells) and **B** excluding (8915 spikes from 6 cells) burst spikes. The normalised spike-initiation threshold was calculated from $V_{\mathrm{Tnorm}} = (V_{\mathrm{T}} - V_{\mathrm{Tbaseline}})/\sigma_{V_{\mathrm{T}}}$, where $V_{\mathrm{Tbaseline}}$ and $\sigma_{V_{\mathrm{T}}}$ are the mean and standard deviation of the threshold measured for those spikes with no spikes in the preceding 50ms, respectively. Bars denote statistical significance ($p < 0.014$).

inset). The spike-initiation threshold depends on the time since the last spike, displaying a post-spike jump followed by a mono-exponential decay (Figure 6.1D) of the form

$$V_{\mathrm{T}} = V_{\mathrm{T0}} + V_{\mathrm{T1}} e^{-t/\tau_{\mathrm{T}}}, \tag{6.1}$$

where t is the time since the last spike, V_{T0} the baseline threshold, V_{T1} the post-spike jump, and τ_{T} the decay time constant, which is of the same form measured from neocortical pyramidal cells using the dynamic I-V method (Chapter 4, Badel *et al.* 2008a,b).

To investigate how the spike-initiation threshold is affected by multiple spikes I measured its value for each spike and binned the results by the number of spikes in the preceding 50 ms. One spike in the preceding 50 ms gave a large increase in spike-initiation threshold; however, the relative threshold decreased again with an additional preceding spike. Three spikes in the preceding 50 ms was not significantly different from two spikes (Figure 6.2A). This appeared counter intuitive as one would expect the threshold to increase monotonically with the number of preceding spikes. This non-monotonic behaviour can be explained by the presence of burst spikes, which have a significantly higher threshold than non-burst spikes (Figure 6.1C) skewing the distribution. Removing burst spikes from the dataset led to a monotonic

increase (Figure 6.2B).

6.2.1 The rEIF Model with Threshold Accumulation

The rEIF model includes the post-spike response of the parameters in the EIF model (Badel *et al.* 2008a,b). These responses are modelled as a renewal process, so after each spike the spike-onset threshold increases to a fixed value above baseline before decaying exponentially. However, as discussed above the threshold accumulates with multiple spikes with short inter-spike intervals (Figure 6.2), a feature lacking from the rEIF model.

To include this behaviour into the rEIF model I first measured the spike-initiation threshold for individual spikes using the second derivative method (Figure 6.1B). I grouped each spike by its preceding inter-spike interval (t_{pre}) and measured how the subsequent spike's threshold depended on the inter-spike interval (t_{post}, Figure 6.3A). When spikes were grouped in this way the spike-initiation threshold depended exponentially on t_{post} (Figure 6.3B). Fitting an exponential of the form of equation (6.1) to the response of each of these groups determined the dynamics of the parameters V_{T0}, V_{T1}, and τ_{T} as a function of t_{pre}. The jump in threshold V_{T1} depended exponentially on t_{pre} (Figure 6.3C), although the baseline threshold and decay time constant showed no such dependence (Figures 6.3D-E).

The post-spike threshold dynamics can then be modelled by

$$\begin{aligned} V_{\mathrm{T}}(t_{\mathrm{post}}) &= V_{\mathrm{T0}} + V_{\mathrm{T1}}(t_{\mathrm{pre}})e^{-t_{\mathrm{post}}/\tau_{\mathrm{T1}}}, \\ V_{\mathrm{T1}}(t_{\mathrm{pre}}) &= \hat{V}_{\mathrm{T1}} + V_{\mathrm{T2}}e^{-t_{\mathrm{pre}}/\tau_{\mathrm{T2}}}, \end{aligned} \tag{6.2}$$

where V_{T0}, $\hat{V}_{\mathrm{T1}}$, and τ_{T1} are the original baseline, jump, and time constant, respectively, fitted using the dynamic I-V method, and V_{T2} and τ_{T2} are the spike-triggered increase and time constant of V_{T1}. I then define the accumulating threshold rEIF (ATrEIF) model as having these threshold dynamics coupled with the voltage dynamics of the EIF model, given by

$$\frac{\mathrm{d}V}{\mathrm{d}t} = \frac{1}{\tau}\left(E - V + \Delta_{\mathrm{T}}e^{(V-V_{\mathrm{T}})/\Delta_{\mathrm{T}}}\right) + \frac{I_{\mathrm{in}}(t)}{C}, \tag{6.3}$$

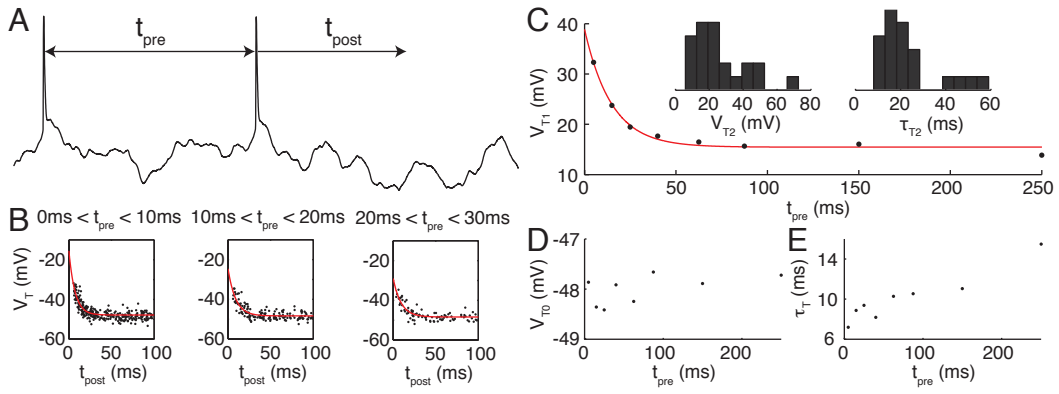

Figure 6.3: Fitting the refractory exponential integrate-and-fire model with threshold accumulation. **A** t_{pre} is the preceding inter-spike-interval and t_{post} is the post-spike time between a given action potential and the threshold measurement. **B** Spikes were binned by their t_{pre} time and a mono-exponential fitted to the spike-initiation threshold response. **C** *Main:* Threshold jump as a function of t_{pre} displays a mono-exponential response. *Inset:* Histograms of fitted values of the jump V_{T2} and decay time constant τ_{T2} of V_{T1} as a function of t_{pre} ($n = 22$). Parameters both fit a log-normal distributions. The mean and variance (μ, σ) of V_{T2} and τ_{T2} were (26 mV, 20 mV) and (23 mV, 14 mV), respectively. **D** The baseline threshold and **E** decay time constant displayed no dependance on t_{pre}.

where τ is the membrane time constant, E the resting potential, Δ_{T} the spike sharpness, and V_{T} the spike-onset threshold; and the post-spike E and g dynamics of the rEIF model, given by

$$g = g_0 + g_1 e^{-(t-t_{\text{ref}})/\tau_{\text{g}}}, \tag{6.4}$$

$$E = E_0 - E_1 e^{-(t-t_{\text{ref}})/\tau_1} + E_2 e^{-(t-t_{\text{ref}})/\tau_2}, \tag{6.5}$$

where t is the time since the peak of the previous spike; t_{ref} is the refractory period; g_0, and E_0 are baseline values calculated from the pre-spike dynamic I-V curve; g_1, E_1, and E_2 are constant exponential coefficients; and τ_{g}, τ_1, and τ_2 are the exponential time constants. Fitting the additional threshold parameters of equations (6.2) to 22 TL5 pyramidal cells showed that they follow log-normal distributions (Figure 6.3C inset), and that the spike-triggered jump in spike-onset threshold could increase by two or three times its baseline value after two very closely spaced spikes. The performance of the ATrEIF model, along with three other models will be assessed in Section 6.2.3.

6.2.2 Two-variable Exponential Integrate-and-Fire Model

The higher dimensionality of the ATrEIF model results in reduced mathematical tractability. To allow further theoretical analysis whilst retaining the experimental applicability I introduce an alternative extension to the standard EIF model, including the refractory properties of the spike-onset threshold and omitting the post-spike dynamics of E and τ that make up the rEIF model. This leads to the two-variable EIF (2vEIF) model, a mathematically tractable two variable system governed by

$$\begin{aligned} \tau \frac{\mathrm{d}V}{\mathrm{d}t} &= E - V(t) + \Delta_{\mathrm{T}} e^{(V(t)-V_{\mathrm{T}}(t))/\Delta_{\mathrm{T}}} + U(t), \\ V_{\mathrm{T}}(t) &= V_{\mathrm{T0}} - V_{\mathrm{T1}} e^{-t/\tau_{\mathrm{T}}}, \end{aligned} \tag{6.6}$$

where t is the time since the last spike, τ the membrane time constant, E the resting membrane potential, Δ_{T} the spike sharpness, V_T the spike-onset threshold, and $U(t)$ the input to the system.

One important point to note about this extension is that when the two time constants are equal ($\tau = \tau_{\mathrm{T}}$) the model reduces to the standard EIF model with a lower post-spike reset value. This can be seen by making the transformation

$$W(t) = V(t) - V_{\mathrm{T}}(t) + V_{\mathrm{T0}}, \tag{6.7}$$

which results in a single-variable system given by

$$\tau \frac{\mathrm{d}W}{\mathrm{d}t} = E - W + \psi(W, t) + U(t), \tag{6.8}$$

where the non-linear term is now defined as

$$\begin{aligned} \psi(W,t) \ &= \Delta_{\mathrm{T}} e^{(W-V_{\mathrm{T0}})/\Delta_{\mathrm{T}}} + \epsilon V_{\mathrm{T1}} e^{-t/\tau_{\mathrm{T}}} \\ &:= \psi_0(W) + \epsilon \psi_\epsilon(t;\epsilon), \end{aligned} \tag{6.9}$$

where $\epsilon = \tau/\tau_{\mathrm{T}} - 1$. The system now has a constant spike-onset threshold, a lower reset value of $W_{\mathrm{re}} = V_{\mathrm{re}} - V_{\mathrm{T1}}$, and an exponential drift current (Figure 6.4A), and the W distribution is skewed towards more sub-threshold voltages (Figure 6.4B). When

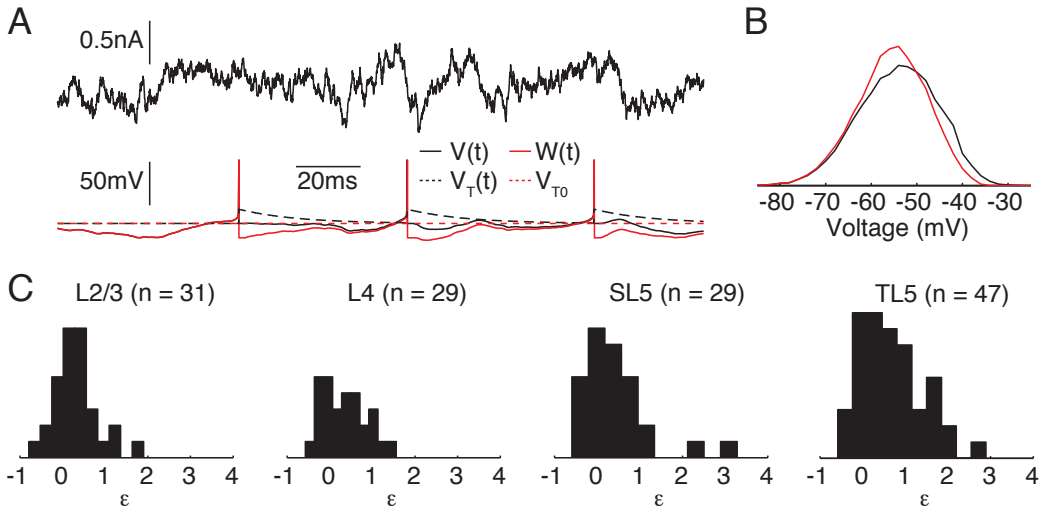

Figure 6.4: Reduction of the two variable exponential integrate-and-fire model. **A** Ornstein-Uhlenbeck process current injection (top) and simulated voltage response (bottom) of the two-variable [black, equation (6.6)] and single-variable [red, equation (6.8)] EIF models. Dotted lines indicate the spike-onset threshold dynamics in the two systems. **B** Sub-threshold voltage distributions with spikes omitted. Cell parameters used for simulation were measured from an example thick-tufted layer 5 pyramidal cell using the dynamic *I-V* curve method (Badel *et al.* 2008a,b, Chapter 4). These parameters were $C = 197\,\mathrm{pF}$, $\tau = 18\,\mathrm{ms}$, $E = -60.5\,\mathrm{mV}$, $V_{\mathrm{T0}} = -42.8\,\mathrm{mV}$, $V_{\mathrm{T1}} = 16.4\,\mathrm{mV}$, $\Delta_{\mathrm{T}} = 1.64\,\mathrm{mV}$, and $\tau_{\mathrm{T}} = 17.7\,\mathrm{ms}$, giving $\epsilon = 0.0169$. **C** Experimental histograms of ϵ $(= \tau/\tau_{\mathrm{T}} - 1)$ for (from left to right) neocortical layer 2/3, layer 4, slender-tufted layer 5, and thick-tufted layer 5 pyramidal cells, with means and standard errors $(\mu,\ \sigma)$: (0.31, 0.54), (0.36, 0.53), 0.40, 0.81), and (0.72, 0.77), respectively. The experimental dataset used in Chapters 4 and 5 was used to calculate these histograms.

the voltage and threshold timescales are equal the second term in equation (6.9) vanishes, yielding the standard EIF model with a lower reset. The parameter ϵ is seen to be small in neocortical pyramidal cells from layers 2/3-5 (Figure 6.4C), indicating that approximating these time constants as equal, or close to equal is experimentally valid.

6.2.3 Performance of the EIF Model Variants

I assessed the performance of the EIF model and its variants by simulating the response to a stimulus not used for fitting and comparing the result to the experimental trace. After an action potential pyramidal cells typically have a high reset above baseline threshold (Figure 4.4). However, since the standard EIF model includes no refractory mechanism this choice of reset will result in continual spiking. Since I was interested in how the presence or absence of various refractory mechanisms affect

model performance I avoided this by choosing a reset value of 2 mV below baseline threshold for all models. I set the refractory period to 2 ms as opposed to 4 ms in Chapters 4 and 5. This was for two reasons. Firstly, 2 ms is a more relevant duration for the refractory period in TL5 pyramidal cells as it is the approximate width of their action potential (Figure 4.10C); the high reset of the previous chapters necessitated a long refractory period. Secondly, this allow for more direct comparison to previous work (Richardson 2007; Badel *et al.* 2008a; Richardson 2008; Badel *et al.* 2008b).

Example simulations of the standard EIF (red), rEIF (green), ATrEIF (blue), and 2vEIF (purple) are shown in Figure 6.5A in comparison to the experimental trace (black). The sub-threshold response of all four models away from spikes appears to be similar. However, the EIF model fires at much too high a rate during periods when the cell fires multiple action potentials in quick succession. The remaining three models appear similar in terms of spiking precision, although the ATrEIF model better captures the pair of action potentials on the left of the trace.

I quantified the performance difference between models using the measures introduced in Chapter 4. The metric that displayed the largest difference between models was the mean firing rate (Figure 6.5B). The EIF model fired at almost three times that of the real cell on average. There was no significant difference between the experiment and the rEIF or ATrEIF models ($p = 0.0945$ and $p = 0.217$, respectively), although there was a small (0.28 Hz) but significant ($p = 1.27 \times 10^{-4}$) reduction in firing rate of the ATrEIF over the rEIF model.

Both the EIF and 2vEIF models matched a significantly higher percentage of spikes than the rEIF and ATrEIF models (Figure 6.5C). However, this is a misleading measure as both the EIF and 2vEIF models fired at a significantly higher rate than the cell leading to more spikes lying within the designated precision (5 ms), but also leading to a significantly greater number of false spikes (Figure 6.5D). This resulted in a significantly lower coincidence ratio of 0.575 and 0.625 for the EIF and 2vEIF models, respectively, compared to 0.770 and 0.772 for the rEIF and ATrEIF models, respectively (Figure 6.5E).

Finally, the differences in the sub-threshold deviation of the four models from

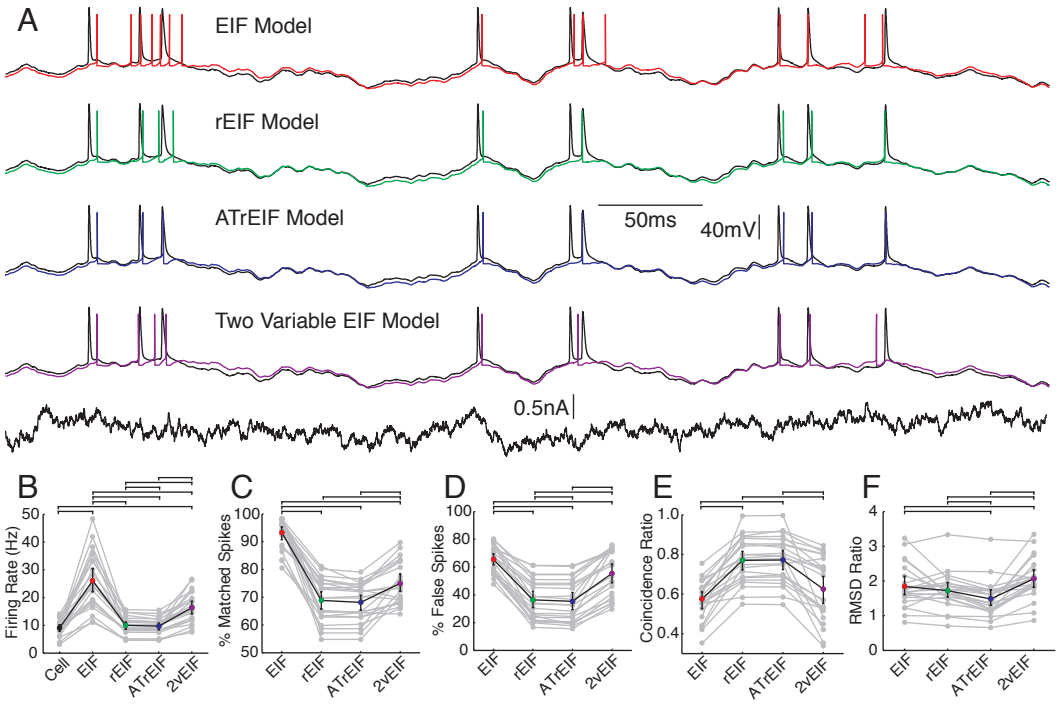

Figure 6.5: Spike-threshold adaptation mechanisms are essential for capturing spike-timing in thick-tufted layer 5 pyramidal cells. **A** Simulations of the four EIF model variants, the standard EIF (red), rEIF (green), ATrEIF (blue), and 2vEIF (purple) models, compared to the experimental trace (black). Bottom trace in the current stimuli. **B** Firing rate, **C** percentage of matched spikes, **D** percentage of false spikes, **E** coincidence ratio, and **F** root mean squared deviation ratio of the four models. Mean values indicated in colour and results for individual cells ($n = 22$) are indicated in grey. Error bars show the 95% bootstrap confidence interval calculated using 2000 bootstrap samples. Horizontal bars denote statistical significance between models calculated using the Wilcoxon ranked signed test for paired comparisons, with the application of the Bonferroni correction for multiple comparisons at the 5% confidence level.

that of the cell, measured as a ratio of the RMSD between the model and experiment to the RMSD between two repeat experiments, was less striking (Figure 6.5F). The best performance was by the ATrEIF model, which had an average sub-threshold deviation 48.3% higher than that of the repeat experiment, compared to a 84.4%, 72.0%, and 106% increase for the EIF, rEIF, and 2vEIF models, respectively.

6.3 Discussion

In this Chapter I investigated the consequences of the experimentally observed spike-triggered threshold dynamics in thick-tufted layer 5 neocortical pyramidal cells. This threshold is highly variable (Figure 6.1C) and displays a spike-triggered jump and subsequent decay over tens of milliseconds, measured either using the dynamic I-

V method (Badel *et al.* 2008a,b, Chapter 4), or by measuring the spike-initiation threshold for each spike individually (Figure 6.1D). Furthermore, the spike-initiation threshold accumulates as a result of increased recent spiking activity in TL5 pyramidal cells (Figure 6.2), as seen in previous studies (Henze and Buzsáki 2001; Chacron *et al.* 2007). Extending the rEIF model to capture this threshold accumulation resulted in a small yet significant improvement (Figure 6.5). The standard EIF model supplemented with only the threshold dynamics performed worse than models with additional parameter dynamics, but was still a significant improvement over non-dynamic parameters and is amenable to theoretical approaches.

6.3.1 Extensions to The Exponential Integrate-and-fire Model

I compared three extensions to the standard EIF model that incorporate the observed threshold dynamics. The first was the previously introduced rEIF model (Badel *et al.* 2008a,b), which I showed in Chapter 4 provided a good fit to pyramidal cells across the neocortex. This model not only captures the post-spike threshold dynamics, but also those observed in the conductance and resting potential (Figure 4.3D). One should note that this model is a renewal process and does not attempt to capture the experimentally observed threshold accumulation. Despite ignoring the non-renewal nature of real cells, the rEIF model matched 71% of spike times with an average coincidence ratio of 0.82. This is at worst comparable to alternative models and at best an improvement (Jolivet *et al.* 2006b, 2008; Kobayashi *et al.* 2009; Mensi *et al.* 2012, Section 4.2.2).

To address the non-renewal nature of the rEIF model, I introduced the Accumulating Threshold rEIF (ATrEIF) model, which is the rEIF model supplemented by an accumulation in spike-onset threshold. I included this threshold accumulation by fitting the dynamics described by equation (6.2), as illustrated in Figure 6.3. The increase in the post-spike threshold jump, V_{T2}, depended exponentially on the preceding inter-spike interval (Figure 6.3C). Non-renewal threshold dynamics such as this have been shown to result in experimentally observed response properties, such as negative inter-spike interval correlations (Chacron *et al.* 2001, 2003) and spike-frequency adaptation (Chacron *et al.* 2003). The ATrEIF model produced a very

small, but statistically significant improvement over the rEIF model (Figure 6.5).

The final model considered was the Two-variable EIF (2vEIF) model suggested by (Badel *et al.* 2008b), defined by the system in equation (6.6). This is the standard EIF model supplemented by the post-spike threshold dynamics determined using the dynamic I-V method, and sits between the EIF and rEIF models in terms of complexity. Although the performance of the 2vEIF model was worse than both the rEIF and the ATrEIF models, it was still a significant improvement over the standard EIF model (Figure 6.5) and has the advantage that it is relatively simple to analyse, amenable to theoretical approaches. Furthermore, the fact that ϵ is small has the important consequence that a low post-spike reset value with a constant spike-onset threshold is equivalent to the more experimentally relevant situation of a high reset (Figure 4.4) with a spike-triggered threshold increase.

Chapter 7

Population Response of Two Variable EIF Models

7.1 Introduction

Coupling reduced models of neuron voltage dynamics to models describing fluctuating synaptic drive (Stein 1965) provides a mathematically tractable description of the firing rate response of neurons subject to *in vivo*-like stimuli. These methods have been used extensively in the past half-century (Lindner *et al.* 2004; Burkitt 2006a,b); both the leaky (Rauch *et al.* 2003; Paninski *et al.* 2004; Jolivet *et al.* 2006b) and exponential (Badel *et al.* 2008a,b) integrate-and-fire models have been shown to well match the mean firing rate and spike arrival times of neocortical pyramidal cells. The stochastic voltage dynamics induced by fluctuating stimuli require a probabilistic interpretation where the distributions of the variables of interest are considered, an approach that enables the description of populations of neurons and their network states (Brunel 2000; Gerstner 2000).

The diffusion approximation is a standard technique for treating fluctuating synaptic drive that approximates the Poissonian distribution of discrete synaptic inputs as a Gaussian process; however, this is only valid in the limit of high arrival rates. Under this approximation the time-dependent dynamics of the voltage probability distribution can be described by the Fokker-Planck equation (Risken 1996). This provides a framework that has enabled the inclusion of further biological real-

ism into populations of simple reduced neuron models, such as synaptic correlations (Moreno *et al.* 2002), filtering (Brunel *et al.* 2001), or conductance (Moreno-Bote and Parga 2005).

In Chapter 6 I discussed the threshold variability of thick-tufted layer 5 pyramidal cells, and in particular the post-spike threshold response. I demonstrated the importance of including refractory parameter dynamics in the construction of a realistic model. In particular, including the observed spike-triggered threshold dynamics in the standard EIF model results in a significant improvement without a great increase in mathematical complexity (Figure 6.5); this two-variable EIF (2vEIF) model, defined by equations 6.6, is amenable to further analytical study.

Analytical expressions for the response properties of LIF neurons with an exponentially decaying threshold have been calculated (Lindner and Longtin 2005), but restrict the post-spike jump to be small (less than 20% of the potential difference between rest and the baseline threshold). In this chapter I extend this work to an arbitrary jump in threshold, calculating the response properties of populations of the more experimentally relevant EIF model neurons (Badel *et al.* 2008a,b). Utilising two key facts: that the membrane to threshold time constant ratio is close to one (Figure 6.4); and that the 2vEIF model [equation (6.6)] can be reduced to a single variable [equations (6.8) and (6.9)], I take a perturbative approach to solving the Fokker-Planck equation corresponding to a population of 2vEIF neuron models. To do this I use the threshold integration method, a convenient numerical scheme previously applied to populations of LIF and EIF neurons (Richardson 2007, 2008). I find that this approach yields results in excellent agreement with simulations of the first passage time density, spike-triggered rate density, and spike-train spectrum in both low noise/high firing rate and high noise/low firing rate regimes. Furthermore, results agree with the population response over the physiological range of the membrane to threshold time constant ratio.

7.2 Results

I showed in Section 6.2.2 that the two-variable EIF (2vEIF) model can be transformed to a single variable model, governed by equations (6.8) and (6.9), and in the case of equal voltage and threshold timescales is equivalent to the standard EIF model with a lower rest value (Figure 6.4A).

In neocortical pyramidal cells, these two timescales are similar (Figure 6.4C), affording the use of a perturbative approach for solving the corresponding Fokker-Planck equation, which is defined by

$$\frac{\partial P}{\partial t} + \frac{\partial J}{\partial W} = \text{initial} + \text{boundary conditions}, \tag{7.1}$$

where $P(W,t)$ is the probability density and $J(W,t)$ probability flux. I solved the system under delta-correlated Gaussian white noise $\xi(t)$, so that the full system is now

$$\tau \frac{\mathrm{d}W}{\mathrm{d}t} = E - W + \psi(W,t) + \sigma\sqrt{2\tau}\xi(t), \tag{7.2}$$

where t is the time since the last spike, τ is the membrane time constant, E the resting membrane potential, σ is the noise strength in mV, and the non-linear term $\psi(W,t)$ is defined as

$$\begin{aligned} \psi(W,t) &= \Delta_{\mathrm{T}} e^{(W-V_{\mathrm{T0}})/\Delta_{\mathrm{T}}} + \epsilon V_{\mathrm{T1}} e^{-t/\tau_{\mathrm{T}}} \\ &:= \psi_0(W) + \epsilon\psi_\epsilon(t;\epsilon), \end{aligned} \tag{7.3}$$

where Δ_{T} is the spike sharpness, V_T the spike-onset threshold, and $\epsilon = \tau/\tau_{\mathrm{T}} - 1$. The initial conditions are $V(0) = V_{\mathrm{re}}$ and $V_{\mathrm{T}}(0) = V_{\mathrm{T1}}$, where V_{re} is the post-spike reset potential. Note the implicit dependence of ψ_ϵ on ϵ (since $\tau_T = \tau_T(\epsilon)$ from the definition of ϵ). This allowed for two solutions: a strict first order solution, where $\epsilon = 0$ and $\psi_\epsilon \approx V_{T1}e^{-t/\tau}$, or an uncontrolled solution where ψ_ϵ remains exact.

The case of constant spike-onset threshold without time dependent drift has previously been investigated by Richardson (2007, 2008), and it was using these methods that I analysed the perturbed system. For the system in equations (7.2)

and (7.3), equation (7.1) can be written as two coupled partial differential equations:

$$-\frac{\partial J}{\partial W} = \frac{\partial P}{\partial t} + f(t)\delta(W - W_{\text{th}}) - \delta(t - t_{\text{ref}})\delta(W - W_{\text{re}}), \tag{7.4a}$$

$$-\frac{\partial P}{\partial W} = \frac{1}{\sigma^2}\left(\tau J + (W - E - \psi)P\right), \tag{7.4b}$$

where $f(t)$ is the first passage time (FPT) density, and the absorbing boundary at the absolute spike threshold ($W = W_{\text{th}}$) and an initial delta pulse distribution at $t = t'$ and $W = W'$ are included in equation (7.4a). The natural choice for the initial distribution is $t' = t_{\text{ref}}$ and $W' = W_{\text{re}}$, corresponding to a spike at $t = 0$ followed by a refractory period of t_{ref} at a reset voltage of W_{re}. For completeness, I shall next outline the strategy for numerically integrating these equations.

7.2.1 The Threshold Integration Method

The threshold integration method (Richardson 2007, 2008) involves integrating backwards from threshold W_{th} to a lower bound W_{lb}. The voltage is discretised into $n+1$ steps, so that $W^{(k)} = W_{\text{lb}} + k\Delta$, where $k = 0, 1, \ldots, n$ and Δ is the voltage step size (0.01 mV). The J equation [equation (7.4a)] and the P equation [equation (7.4b)] must be solved simultaneously; however, a different numerical scheme is used for each.

The J equations can be integrated using a standard Euler scheme. However, this scheme would be unstable if used to integrate the P equations due to the large values that ψ can take. The P equations are of the general form

$$-\left(\frac{dP}{dt} + G(W)P(W)\right) = H(W), \tag{7.5}$$

where in this case $G(W)$ contains the ohmic and non-linear terms of the EIF model. Equation (7.5) can then be integrated directly to get

$$P^{(k-1)} = P^{(k)} e^{\left(\int_{W^{(k-1)}}^{W^{(k)}} G(W')dW'\right)} + \int_{W^{(k-1)}}^{W^{(k)}} H(W') e^{\left(\int_{W^{(k-1)}}^{W'} G(W'')dW''\right)} dW', \tag{7.6}$$

which can be approximated as

$$P^{(k-1)} \approx P^{(k)} e^{\Delta G^{(k)}} + \int_{W^{(k-1)}}^{W^{(k)}} H^{(k)} e^{\Delta G^{(k)}(W' - W^{(k-1)})} dW' \tag{7.7}$$

$$\approx P^{(k)} e^{\Delta G^{(k)}} + H^{(k)} \left(\frac{e^{\Delta G^{(k)}} - 1}{G^{(k)}} \right), \tag{7.8}$$

with the initial condition $P^{(n)} = 0$.

Note also that in the following text the convention for the Fourier transform of a function $F(t)$ is $\tilde{F}(\omega) = \int_{-\infty}^{\infty} e^{-i\omega t} F(t) \mathrm{d}t$, with inverse $F(t) = \frac{1}{2\pi} \int_{-\infty}^{\infty} e^{i\omega t} \tilde{F}(\omega) \mathrm{d}t$. The convolution convention is $F(x) * G(x) = \int_{-\infty}^{\infty} F(x-y) G(y) \mathrm{d}y$.

7.2.2 Population Response Properties

To solve the system in equation (7.4) I first expanded to first order in ϵ:

$$J = J_0 + \epsilon J_\epsilon, \quad P = P_0 + \epsilon P_\epsilon, \quad f = f_0 + \epsilon f_\epsilon. \tag{7.9}$$

This expansion yielded two sets of partial differential equations, one for the unperturbed system:

$$-\frac{\partial J_0}{\partial W} = \frac{\partial P_0}{\partial t} + f_0 \delta(W - W_{\mathrm{th}}) - \delta(t - t_{\mathrm{ref}}) \delta(W - W_{\mathrm{re}}), \tag{7.10a}$$

$$-\frac{\partial P_0}{\partial W} = \frac{1}{\sigma^2} \left(\tau J_0 + (W - E - \psi_0) P_0 \right), \tag{7.10b}$$

as solved by Richardson (2008), and a second for the perturbation:

$$-\frac{\partial J_\epsilon}{\partial W} = \frac{\partial P_\epsilon}{\partial t} + f_\epsilon \delta(W - W_{\mathrm{th}}), \tag{7.11a}$$

$$-\frac{\partial P_\epsilon}{\partial W} = \frac{1}{\sigma^2} \left(\tau J \epsilon + (W - E - \psi_0) P_\epsilon - \psi_\epsilon P_0 \right). \tag{7.11b}$$

To solve the perturbed system I proceeded as for the unperturbed case solved by Richardson (2008). I first calculated the Fourier transform to remove the time

derivative:

$$-\frac{\partial \tilde{J}_\epsilon}{\partial W} = i\omega \tilde{P}_\epsilon + \tilde{f}_\epsilon \delta(W - W_{\text{th}}), \tag{7.12a}$$

$$-\frac{\partial \tilde{P}_\epsilon}{\partial W} = \frac{1}{\sigma^2}\left(\tau \tilde{J}_\epsilon + (W - E - \psi_0)\tilde{P}_\epsilon - C(W,\omega)\right), \tag{7.12b}$$

where $C(W,\omega) = \frac{1}{2\pi}\left(\tilde{\psi}_\epsilon * \tilde{P}_0\right)$, which could be evaluated numerically. The inhomogeneous terms in equations (7.12) can be separated by defining

$$\tilde{J}_\epsilon = \tilde{f}_\epsilon \tilde{j}_{f_\epsilon} + \tilde{j}_C, \quad \tilde{P}_\epsilon = \tilde{f}_\epsilon \tilde{p}_{f_\epsilon} + \tilde{p}_C, \tag{7.13}$$

leading to

$$-\frac{\partial \tilde{j}_{f_\epsilon}}{\partial W} = i\omega \tilde{p}_{f_\epsilon} + \delta(W - W_{\text{th}}), \tag{7.14a}$$

$$-\frac{\partial \tilde{p}_{f_\epsilon}}{\partial W} = \frac{1}{\sigma^2}\left(\tau \tilde{j}_{f_\epsilon} + (W - E - \psi_0)\tilde{p}_{f_\epsilon}\right), \tag{7.14b}$$

and

$$-\frac{\partial \tilde{j}_C}{\partial W} = i\omega \tilde{p}_C, \tag{7.15a}$$

$$-\frac{\partial \tilde{p}_C}{\partial W} = \frac{1}{\sigma^2}\left(\tau \tilde{j}_C + (W - E - \psi_0)\tilde{p}_C - C(W,\omega)\right). \tag{7.15b}$$

Then using the zero flux condition at the lower bound voltage, the Fourier transform of the first order FPT density is given by

$$\tilde{f}_\epsilon(\omega) = -\frac{\tilde{j}_C(W_{\text{lb}})}{\tilde{j}_{f_\epsilon}(W_{\text{lb}})}. \tag{7.16}$$

which can be inverted to give the first order correction to the FPT density. After applying the inverse Fourier transform the FPT density could be recovered from equation (7.9).

The steady state firing rate can be calculated from the moments of the FPT,

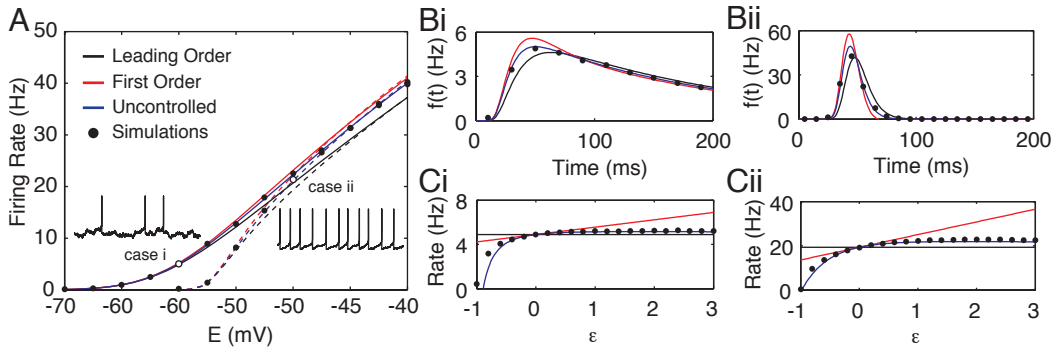

Figure 7.1: Uncontrolled perturbative solution captures the firing rate and first passage time of an uncoupled population of EIF neurons. **A** Firing rate as a function of resting potential at two noise intensities [$\sigma = 2\,\mathrm{mV}$ (dashed lines) and $\sigma = 6\,\mathrm{mV}$ (solid lines), $\epsilon = 0.5$], compared to simulations of the two variable system (dots). **B** First passage time of two regimes: sub-threshold noise driven firing (case i, $\sigma = 6\,\mathrm{mV}$ and $E = -60\,\mathrm{mV}$) and supra-threshold quasi-deterministic firing (case ii, $\sigma = 2\,\mathrm{mV}$ and $E = -50\,\mathrm{mV}$). **C** Firing rate as a function of ϵ in the two regimes. Parameters used were $\tau = 20\,\mathrm{ms}$, $\Delta_\mathrm{T} = 3\,\mathrm{mV}$, $V_{\mathrm{T}0} = -53\,\mathrm{mV}$, $V_{\mathrm{T}1} = 20\,\mathrm{mV}$, $W_\mathrm{th} = 0\,\mathrm{mV}$, $t_\mathrm{ref} = 2\,\mathrm{ms}$, and $V_\mathrm{re} = -60\,\mathrm{mV}$.

defined by

$$\langle T^n \rangle = \int_0^\infty t^n f(t) dt, \tag{7.17}$$

where T is the inter-spike interval. This relates to $\tilde{f}(\omega)$ using the definition of the Fourier transform:

$$\langle T^n \rangle = i^n \frac{d^n \tilde{f}}{d\omega^n}\bigg|_{\omega=0}. \tag{7.18}$$

The firing rate was then given by

$$r = \left(i \frac{d\tilde{f}}{d\omega}\bigg|_{\omega=0} \right)^{-1}, \tag{7.19}$$

which is shown in Figure 7.1A as a function of the membrane resting potential E for two different noise intensities: $\sigma = 2\,\mathrm{mV}$ (dashed lines) and $\sigma = 6\,\mathrm{mV}$ (solid lines). These results were compared with simulations of the 2vEIF model defined by equation (6.6). These simulations were performed using the same methods as in Chapter 6, but with the parameters give in the legend to Figure 7.1.

The uncontrolled solution agreed well with simulations for both values of σ. Two example parameter sets were chosen, one resulting in sub-threshold noise driven firing (case i, $\sigma = 6\,\mathrm{mV}$ and $E = -60\,\mathrm{mV}$) and the other resulting in supra-threshold quasi-deterministic firing (case ii, $\sigma = 2\,\mathrm{mV}$ and $E = -50\,\mathrm{mV}$), as illustrated in the

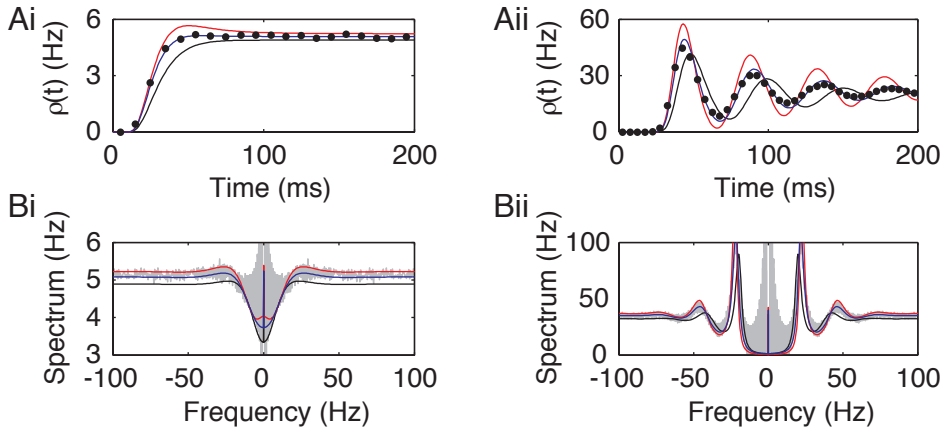

Figure 7.2: Leading order (black), first order (red), and uncontrolled (blue) solutions of the **A** spike-triggered rate density and **B** spike-train spectrum in the two regimes illustrated in Figure 7.1 (cases i and ii). Parameter values for simulations were as stated in Figure 7.1.

insets to Figure 7.1A. The uncontrolled solution for the FPT density (Figure 7.1B) was in good agreement with simulations for both example parameter sets. Furthermore, the uncontrolled solution for the firing rate matched simulations over the entire physiological range of the parameter ϵ (Figure 7.1C).

From the FPT density I calculated further computational quantities of experimental relevance. The spike-triggered rate (STR) density $\rho(t)$ is the time-dependent firing rate of the population incorporating the full reset and refractory period, starting from some initial distribution. For a renewal process this can be calculated from the Fourier transform of the FPT density (Gerstner and Kistler 2002):

$$\tilde{\rho}(\omega) = \frac{\tilde{f}(\omega)}{1 - \tilde{f}(\omega)}, \tag{7.20}$$

for $\omega \neq 0$ and $\tilde{\rho}(0) = \pi r_0 \delta(\omega)$. This is shown for the two example cases in Figure 7.2A with an initial spike at $t = 0$, as for the FPT density. Again, the uncontrolled solution agreed well with simulations.

The auto-correlation function $A(T) = \langle S(t)S(t+T)\rangle$ of a spike train $S(t) = \sum_{\{t_i\}} \delta(t - t_i)$ measures the probability of finding two spikes separated by a time interval T, and is directly related to ρ via

$$A(T) = r\delta(T) + r\rho(|T|), \tag{7.21}$$

(Gerstner and Kistler 2002). The spike-train power spectrum, which is a good measure of spike-train coherence resonance (Lindner *et al.* 2002), can then be calculated as

$$\tilde{A}(\omega) = r(1 + 2\mathbb{R}[\tilde{\rho}(\omega)]), \tag{7.22}$$

which matches simulations for the two example cases (Figure 7.2B).

7.3 Discussion

The focus of this chapter was to analyse the response of populations of the mathematically tractable two-variable EIF (2vEIF) model. As I showed in Chapter 6, despite the model not offering the same performance as the refractory and accumulating threshold variants, it was still a significant improvement over, and provides a mathematically tractable extension to the standard EIF model (Figure 6.5). Indeed, the model can be transformed to a single variable system (Figure 6.4) and a perturbative approach taken for the solution, which captured the population response over the full physiological range of the membrane to threshold timescale ratio (Figure 7.1).

It was noted by Badel *et al.* (2008b) that in the case of the membrane and threshold timescales being equal the two-variable model is equivalent to the standard EIF model with a lower post-spike reset, seen by making the transformation given in equation (6.7). I extend this idea to the case where the two time constants are not equal by introducing a parameter $\epsilon = \tau/\tau_{\mathrm{T}} - 1$, which was seen to be small in neocortical pyramidal cells in layers 2/3-5 (Figure 6.4C). The aforementioned transformation then leads to a system described by the standard EIF model supplemented by a lower reset value and with the addition of an exponential, ϵ dependent drift current [equations (7.2) and (7.3)]. A similar transformation has been made for the leaky integrate-and-fire model supplemented by a spike-triggered exponentially decaying threshold, from which analytical solutions for the statistics of the inter-spike interval were derived (Lindner and Longtin 2005). However, these results relied on the post-spike threshold jump being small, whereas the results presented here make no such assumption.

In this chapter I took a perturbative approach to solve the Fokker-Planck equation corresponding to populations of neurons described by equations (7.2) and (7.3), using the threshold integration method (Richardson 2007, 2008). Although white noise is not a biophysically relevant input current, the population response under this input is not significantly different to that under the more realistic Ornstein-Uhlenbeck process used for the experiments in this work (Alijani and Richardson 2011). I identified two perturbative solutions: a strict first order solution in which the drift term in equation (7.3) is expanded around $\epsilon = 0$, and an uncontrolled solution where it is not. At high firing rates (>10 Hz) the first order solution provided significant correction to the leading order solution for small ϵ in both the sub- and supra-threshold regimes, and the uncontrolled solution a further small correction (Figure 7.1A).

To investigate this further I chose two firing regimes: sub-threshold noise driven firing (case i); and supra-threshold quasi-deterministic firing (case ii), which typify quiescent and active population states, respectively. Whilst the first order solution is only valid for small ϵ, the uncontrolled solution performed well over the entire physiological range of ϵ in both regimes (Figure 7.1C). Finally, from the first passage time I calculated two further relevant time-dependent quantities: the spike-triggered rate (STR) density (Figure 7.2A), the time-dependent firing rate of the population including the full voltage dynamics and post-spike reset; and the spike-train power spectrum (Figure 7.2B), which describes the power of the spike-train as a function of firing frequency and is an important measure of the steady-state population structure. Both of these quantities can be calculated from the FTP density (Gerstner and Kistler 2002, equations (7.20) and (7.22)), and agree well with simulations; the uncontrolled solution again provided a small yet significant correction to the strict first order solution.

The power spectrum is a useful tool that allows us to investigate resonances in a system. Coherence resonance in particular is the effect of noise-enhanced regularity in the neuron's output, and has been observed in both in experimental systems (Liu and Liu 1995; Postnov *et al.* 1999; Giacomelli *et al.* 2000) and mathematical models (Gang *et al.* 1993; Longtin 1997; Pikovsky and Kurths 1997). The noise driven firing

displays little coherence resonance, with only a small broad peak at approximately 20 Hz (Figure 7.2Bi). On the other hand, the quasi-deterministic firing displayed a strong coherence resonance, with a large narrow peak at 20 Hz and a smaller peak at 50 Hz (Figure 7.2Bii), in agreement with previous work suggesting that coherence resonance is maximised for this regime at weak noise levels (Lindner *et al.* 2002).

Chapter 8

The Role of Slow Sodium-Channel Inactivation in Threshold Variability

8.1 Introduction

In Chapter 6 I showed that the spike-initiation threshold in thick-tufted layer 5 pyramidal cells is highly variable, and accumulates as a result of several closely spaced spikes. A number of mechanisms have been shown to modulate this variability via adaptation to the membrane potential through sodium channel inactivation (Fleidervish *et al.* 1996; Fleidervish and Gutnick 1996; Fricker *et al.* 1999; Azouz and Gray 2003; Arganda *et al.* 2007), potassium channel activation (Chi and Nicol 2007; Guan *et al.* 2007; Shu *et al.* 2007b; Goldberg *et al.* 2008), and an increase in inhibitory conductances (Coombs *et al.* 1955; Monsivais and Rubel 2001). In particular, recent modelling studies have focussed on the impact of fast sodium channel inactivation (Platkiewicz and Brette 2010, 2011; Fontaine *et al.* 2014), which returns to its baseline state within a few milliseconds post-spike. However, a slow component of sodium channel inactivation is also known to be present in neocortical cells (Fleidervish *et al.* 1996; Toib *et al.* 1998; Goldin 2003) with a time constant – of the order of tens of milliseconds (Toib *et al.* 1998; Soudry and Meir 2012) – that is

similar to the experimentally measured threshold decay.

In this chapter I quantify the effect of slow-sodium channel inactivation on the spike-onset threshold dynamics. To do this I introduce the slow sodium inactivation (SSI) model, which consists of an existing spiking-neuron model (Wang and Buzsáki 1996) with the addition of a slow inactivation gating variable to the spike-generating sodium current, with dynamics based on previous experimental (Fleidervish *et al.* 1996; Gal *et al.* 2010) and theoretical (Soudry and Meir 2012) results. I find that the inclusion of this extra gating variable results in a post-spike threshold response not present in the original model that is similar to the dynamics seen experimentally. Furthermore, reducing the slow-sodium inactivation variable to a spike-triggered renewal process has minimal impact on the model's voltage or threshold dynamics. Including this reduced form into the EIF model leads to a threshold decay that, to first order, is of the same exponential form observed in neocortical pyramidal cells. Furthermore, the exact form of this decay implies a large spike-triggered jump followed by a steep non-exponential decay over the first few milliseconds post-spike. However, a response of this form did not fit experimental data, suggesting that slow-sodium channel inactivation is likely supplemented by additional conductances.

8.2 Results

8.2.1 Slow Sodium Inactivation Model

To model the influence slow sodium-channel inactivation has on spike-onset threshold I added a slow sodium inactivation variable to the Wang-Buzsáki model (Wang and Buzsáki 1996), an existing spiking-neuron model with Hodgkin-Huxley type channel kinetics, yielding the Slow Sodium Inactivation (SSI) model. This model takes the form

$$C\frac{\mathrm{d}V}{\mathrm{d}t} + g_{\mathrm{L}}(V - E_{\mathrm{L}}) + I_{\mathrm{spike}} = I, \tag{8.1}$$

where V is the membrane potential, C the capacitance, g_{L} the leak conductance, E_{L} the leak reversal potential, I the driving current, and the spike-generating current

Table 8.1: Parameters for the Slow Sodium Inactivation model.

α_m	$\frac{-0.1(V+35)}{e^{-(V+35)/10}-1}$	g_{L}	0.3 μS/cm^2
β_m	$4e^{-(V+60)/18}$	E_{L}	-68 mV
α_h	$0.07e^{-(V+58)/20}$	g_{Na}	120 μS/cm^2
β_h	$\frac{1}{1+e^{-(V+28)/10}}$	E_{Na}	55 mV
α_n	$\frac{-(V+34)/100}{e^{-(V+34)/10}-1}$	g_{K}	36 μS/cm^2
β_n	$0.125e^{-(V+44)/80}$	E_{K}	-72 mV

I_{spike} is given by

$$I_{\mathrm{spike}} = \bar{g}_{\mathrm{Na}} m_\infty^3 hs(V - E_{\mathrm{Na}}) + \bar{g}_{\mathrm{K}} n^4 (V - E_{\mathrm{K}}), \tag{8.2}$$

where the $\bar{g}_i$ are the maximal ionic conductances, the E_i are the ionic reversal potentials, m_∞ is the instantaneous sodium activation variable, h the fast sodium inactivation variable, s the slow sodium inactivation variable, and n the potassium activation variable. The dynamics of the slow sodium inactivation variable s are those used by Soudry and Meir (2012), which are based on the experimental results of Fleidervish *et al.* (1996) and Gal *et al.* (2010). The Wang-Buzsáki model is recovered when $s = 1$.

The gating variables $x \in \{h, s, n\}$ are governed by

$$\tau_x(V)\frac{\mathrm{d}x}{\mathrm{d}t} = x_\infty(V) - x, \tag{8.3}$$

where the voltage dependent steady state (in)activation curves $x_\infty(V)$ (Figure 8.1A) and time constant $\tau_x(V)$ (Figure 8.1B) are given in terms of the channel opening and closing rates $\alpha_x(V)$ and $\beta_x(V)$ respectively:

$$x_\infty(V) = \frac{\alpha_x}{\alpha_x + \beta_x}, \tag{8.4a}$$

$$\tau_x(V) = \frac{1}{\phi(\alpha_x + \beta_x)}, \tag{8.4b}$$

where ϕ is a temperature dependent factor ($\phi = 5$). The parameter values common

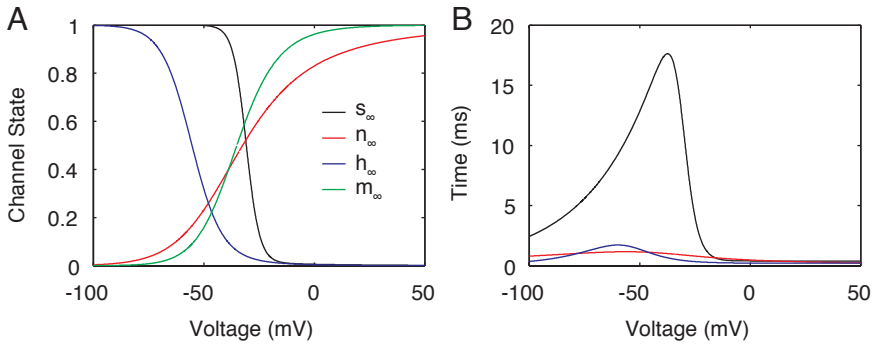

Figure 8.1: Voltage dependent parameters of the SSI model gating variables governed by equation (8.3). **A** Steady-state voltage dependent gating variable (in)activation curves and **B** voltage dependent time constants, defined in terms of the channel opening and closing rates (equations (8.4a) and (8.4a), respectively).

to the original and SSI models are displayed in Table 8.1. The s channel opening and closing rates are given by

$$\alpha_s(V) = \alpha_1 e^{-(v+85)/30}, \tag{8.5a}$$

$$\beta_s(V) = \frac{\beta_1}{e^{-0.3(v+17)} + 1}, \tag{8.5b}$$

where α_1 and β_1 are constants that were varied around their default values (0.05 and 0.51 respectively) to give a range of s channel dynamics.

The inclusion of the slow inactivation variable has a negligible effect on the model spike (Figure 8.2A). However, this additional term gave rise to a post-spike jump in spike-onset threshold followed by a decay that could be well fit by a single exponential (Figure 8.2B) similar to experimental observations (Badel *et al.* 2008a,b, Chapter 4); no such decay was present in the absence of slow sodium-channel inactivation. Furthermore, the computational properties of the model cell were altered, causing a downwards shift in the input-output relationship at medium to high firing rates (>15 Hz, Figure 8.2C).

8.2.2 Simplification of the SSI Model

The dynamics of the s variable can be captured by two parameters: δ_s, the total drop in s over the course of the action potential; and τ_s, the time constant of an exponential fit to the post-spike relaxation of s (Figure 8.3A main). During

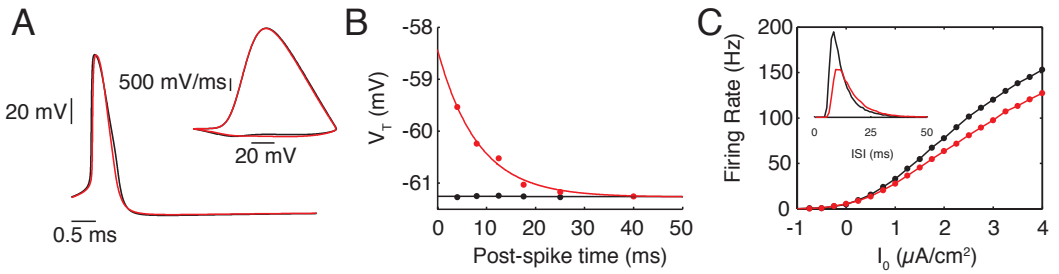

Figure 8.2: Slow sodium-channel inactivation leads to threshold jump and relaxation. **A** Spike shape (main) and phase plane (inset) of the original (black) and augmented (red) conductance based models in response to a current pulse. **B** Post-spike threshold dynamics measured using the dynamic *I-V* curve method (Badel *et al.* 2008a,b, Chapter 4). Points are direct measurements and solid lines are fits to a exponential function. **C** *Main:* Firing rate response to a constant input current (See section 8.2.1). *Inset:* Inter-spike-interval (ISI) distribution for $I_0 = 2\mu\text{A/cm}^2$.

the response of the SSI model to a naturalistic current injection, δ_s and τ_s varied between spikes but their distributions were narrow (Figure 8.3A inset). As a result I approximated the dynamics of s as a renewal process with a spike-triggered response of the form

$$s = 1 - \delta_s e^{-t/\tau_s}, \tag{8.6}$$

where t is the time since the last spike. Simulations of the SSI model with these simplified renewal process dynamics resulted in an almost identical response to the full dynamics (Figure 8.3B), with a similar post-spike threshold behaviour (Figure 8.3C).

To relate δ_s and τ_s to the underlying channel states, one should first note that the steady-state channel inactivation curve s_∞ has a narrow inactivation width compared to the other three gating variables (Figure 8.1A). This leads to the consideration of two regimes: during a spike when $s_\infty = 0$, and away from spikes when $s_\infty = 1$. Furthermore, β_s has a similarly sharp activation curve, and so during a spike $\beta_s = \beta_1$, and away from spikes $\beta_s = 0$. The in-spike approximation then determines the value of δ_s, and the approximation away from spikes determines τ_s.

Considering first the case of during a spike. Since $s_\infty = 0$, solving equation (8.3) yields an exponential decay in s:

$$s = Se^{-t/\tau_s}, \tag{8.7}$$

where S is a constant. The total amount of inactivation achieved during the spike

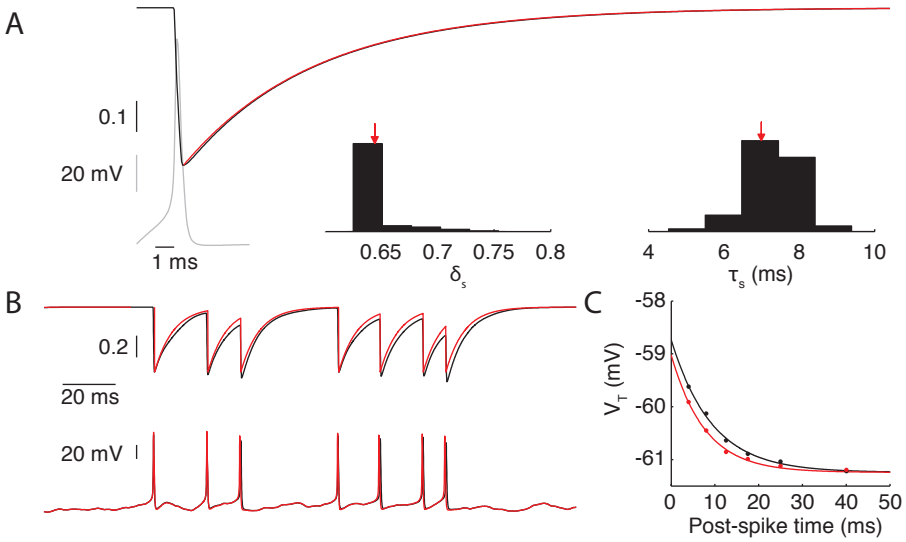

Figure 8.3: Two voltage independent parameters fully capture the dynamics of slow sodium-channel inactivation. **A** *Main:* The post-spike dynamics of s in response to a current pulse (black line) can be described by two voltage independent parameters: δ_s, the total drop in s; and τ_s, the time constant of an exponential fit to the tail of the decay of s back to its baseline value (red line). *Inset:* During a noisy current injection into the SSI model the distributions of these two parameters were narrow with their peak at the single spike value ($\langle\delta_s\rangle = 0.63$, $\langle\tau_s\rangle = 7\,\text{ms}$, 1000 spikes). **B** Response of the s variable (top) and the membrane potential (bottom) of the full (black) and simplified (red) SSI models subject to an Ornstein-Uhlenbeck process current input. **C** The post-spike threshold response measured with the dynamic I-V method is very similar between the two models.

depends on the time constant τ_s - also approximated as a constant during the spike - which in turn depends on the value of β_1 (from equation (8.4b) with $\beta_s = \beta_1$). Since β_1 is in general much larger than α_s, from equation (8.4b) the time constant can be approximated as $\tau_s = 1/\beta_1$. Then δ_s depends on the value of β_1 with the following relation:

$$\delta_s = 1 - Se^{-\hat{t}\beta_1}, \tag{8.8}$$

where $\hat{t}$ is the time after the spike at which s reaches its minimum value (see Figure 8.4B for the empirical fit to this function). If β_1 is large enough the time constant will be small enough so that s will reach its steady state value of 0 (i.e. $\delta_s = 1$) over the course of the spike. The values of α_1 and β_1 used in Figure 8.3A give $\tau_s \approx 2\,\text{ms}$, which is almost fast enough for s to reach equilibrium ($\delta_s \approx 0.7$).

After the spike, the channel properties return to their sub-threshold values: $s_\infty = 1$ and $\beta_s = 0$. By again solving equation (8.3), the post-spike s dynamics are

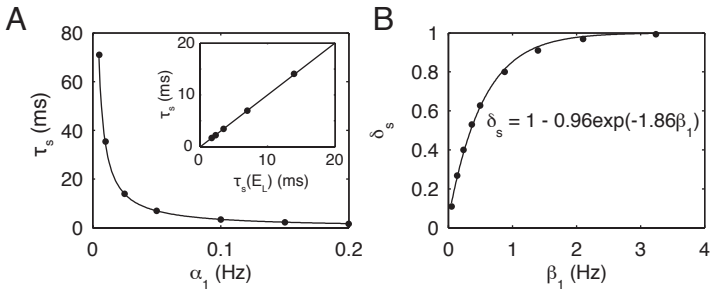

Figure 8.4: The s channel parameters are directly related to the underlying channel opening and closing rates. **A** The value of τ_s measured from a current pulse is equal to the s channel time constant τ_s evaluated at the resting potential (inset), which is inversely proportional to the s channel opening rate (main). **B** δ_s is related to the s channel closing rate by equation (8.8). Points are measured values and lines are fitted functions.

described by

$$s = 1 - \delta_s e^{-t/\tau_s}, \tag{8.9}$$

where t is the time since the minimum value of s and now $\tau_s = 1/\alpha_s$ is 1-2 orders of magnitude larger than the in-spike time constant. The fitted time constant is equal to τ_s evaluated at the resting potential (Figure 8.4A inset). From equation (8.5a) the relationship between τ_s and α_1 is then given by

$$\tau_s = \frac{e^{(E_\mathrm{L}+85)/30}}{\phi\alpha_1}, \tag{8.10}$$

where E_L is the leak conductance reversal potential, as shown in Figure 8.4A.

8.2.3 EIF Model with Slow Sodium-channel Inactivation

The EIF model, which reduces the spike generating sodium current to a voltage dependent exponential, can be written in the form

$$\tau\frac{\mathrm{d}V}{\mathrm{d}t} = E - V + \psi(V) + U(t), \tag{8.11}$$

where τ is the membrane time constant, E the resting potential, $U(t)$ the input to the cell, and $\psi(V)$ the non-linear spike generating term derived from the fast activation of sodium channels, given by

$$\psi(V) = \Delta_\mathrm{T} e^{(V-V_\mathrm{T})/\Delta_\mathrm{T}}, \tag{8.12}$$

where Δ_{T} is the spike sharpness, and V_{T} the spike-onset threshold. This model provides a good fit to the pre- and post-spike instantaneous current-voltage relationship of pyramidal neurons in layers 2/3-5 of the neocortex (Badel *et al.* 2008a,b, Chapter 4), and has been extended to include other mechanisms such as a spike-triggered adaptation current (Brette and Gerstner 2005) and fast sodium-channel inactivation (Platkiewicz and Brette 2010, 2011; Fontaine *et al.* 2014).

The spike generating term ψ is derived with the sodium-channel inactivation terms omitted. Including the slow sodium-channel inactivation term given in equation (8.6) into ψ yields

$$\psi(V,t) = (1 - \delta_s e^{-t/\tau_s})\Delta_{\mathrm{T}} e^{(V-V_{\mathrm{T}})/\Delta_{\mathrm{T}}}. \tag{8.13}$$

Absorbing the s variable into the exponential leads to a non-linear term as in equation (8.12), but with a time-dependent spike-onset threshold given by

$$V_{\mathrm{T}}(t) = V_{T0} - \Delta_{\mathrm{T}} \log(1 - \delta_s e^{-t/\tau_s}), \tag{8.14}$$

where V_{T0} is the baseline threshold. A first order expansion of the logarithmic term in equation (8.14) results in a spike-onset threshold of the form

$$V_{\mathrm{T}} = V_{\mathrm{T0}} + V_{\mathrm{T1}} e^{-t/\tau_{\mathrm{T}}}, \tag{8.15}$$

where t is the time since the last spike, V_{T0} the baseline threshold, V_{T1} the post-spike jump, and τ_{T} the decay time constant. The threshold jump is then given by $V_{\mathrm{T1}} = \Delta_{\mathrm{T}}\delta_s$ and a decay time constant by $\tau_{\mathrm{T}} = \tau_s$. This is directly comparable to the form of the threshold decay measured from neocortical pyramidal neurons *in vitro* (Badel *et al.* 2008a,b, Chapter 4).

This first order approximation implies a small jump in threshold $\sim \mathcal{O}(\Delta_{\mathrm{T}})$. However, experiments show that this is not the case in neocortical pyramidal cells (Badel *et al.* 2008a,b, Chapter 4). The full logarithmic form given in equation (8.14) suggests a steep non-exponential decay in the first $\sim 10\,\mathrm{ms}$ after a spike. This steep jump is not seen when measuring the threshold using either the second derivative

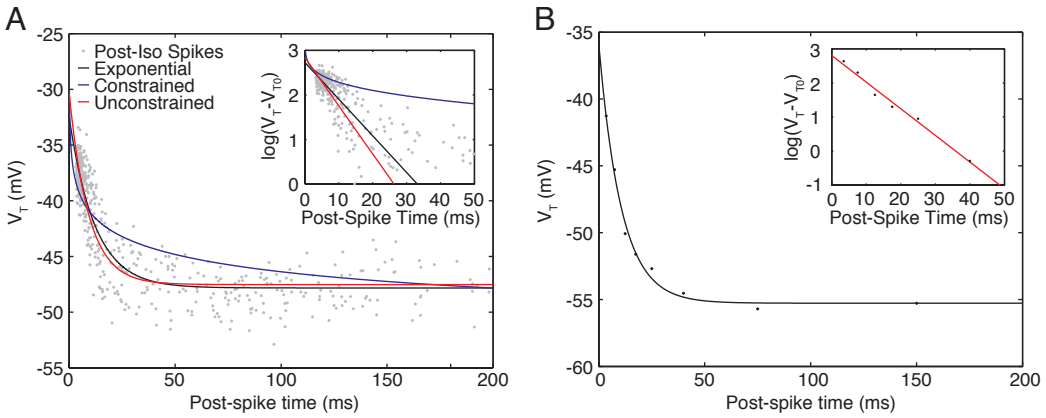

Figure 8.5: Post-spike threshold decay follows a mono-exponential, not the logarithmic form expected from the inclusion of slow sodium-channel inactivation when threshold is measured by either **A** the second derivative method or **B** the dynamic I-V method.

(Figure 8.5A) or the dynamic I-V method (Figure 8.5B). A mono-exponential of the form of equation (8.15), or a logarithmic fit of the form of equation (8.14) with unconstrained parameters both well fit the post-spike threshold response. However, constraining the parameters from the latter to biologically realistic values significantly reduces the fit quality (Figure 8.5A). Furthermore, plotting the threshold response measured using the dynamic I-V method on a logarithmic scale shows a clear linear trend (Figure 8.5B inset), suggesting a mono-exponential decay.

8.3 Discussion

In this Chapter I examined the effect slow sodium-channel inactivation has on the form of the spike-triggered threshold in an attempt to understand the observed dynamics. To do this I first included a slow-inactivation variable into the sodium current of the Wang-Buzsáki model, an existing Hodgkin-Huxley type model that approximates the fast-activation of the spike-generating sodium current as instantaneous. The original model has a constant spike-onset threshold with no spike-triggered dynamics (Figure 8.2B, black), and only a fast component of sodium channel inactivation. Including a slow inactivation into the spike-generating sodium current had little effect on the spike shape (Figure 8.2A) but resulted in a spike-triggered threshold increase and subsequent decay of the form seen in neocortical pyramidal cells (Figure 8.2B, red *cf.* Figure 4.7B). The time constant of this thresh-

old decay was similar to experimental values (9.6 ms), but the spike-triggered jump was an order of magnitude smaller (2.2 mV).

The dynamics of the slow variable could be captured by two parameters (Figure 8.3A), which allowed considerable simplification of the dynamics without impacting the voltage (Figure 8.3B) or spike-onset threshold (Figure 8.3C) responses. Furthermore, these phenomenological parameters have a defined relationship with the channel opening and closing rates (Figure 8.4), ultimately allowing us to relate the threshold dynamics to the underlying channel states.

The non-linear exponential term in the EIF model, given in equation (8.12), is derived from the fast dynamics of sodium channel activation, but omits any form of sodium-channel inactivation (Fourcaud-Trocmé *et al.* 2003). By including the simplified form of the slow inactivation variable I derived a spike-triggered time-dependent threshold given by equation (8.14). The full logarithmic form of the threshold implied an infinite post-spike jump preceding a rapid decay phase lasting $\sim \mathcal{O}(\tau_s)$, followed by a slower mono-exponential-like decay back to baseline.

Expanding this logarithmic form of the threshold response to first order resulted in the exponential form seen experimentally, given by equation (8.15). However, this implied a maximum post-spike jump equal to Δ_{T}, which in neocortical pyramidal cell is $\sim$1 mV compared to the measured jump of $\sim$15 mV (Badel *et al.* 2008a,b, Chapter 4). Furthermore, the spike-onset threshold of an example TL5 pyramidal cell showed a mono-exponential decay even when measurements were taken only a few milliseconds after the peak of the preceding spike, measured using either the second derivative (Figure 8.5A) or dynamic *I-V* (Figure 8.5B) method. Although a threshold response of the form of equation (8.14) did fit experimental data (Figure 8.5A, red line), it only did so with grossly unrealistic parameter values. When parameters were restricted to realistic values a response of this form was completely incorrect (Figure 8.5A, blue line).

Slow sodium-channel inactivation is known to reduce membrane excitability (Vilin and Ruben 2001), although it works via a different molecular mechanism to that of fast-inactivation (Goldin 2003) which affects threshold variability via adaptation to the membrane potential (Platkiewicz and Brette 2010, 2011). Since the

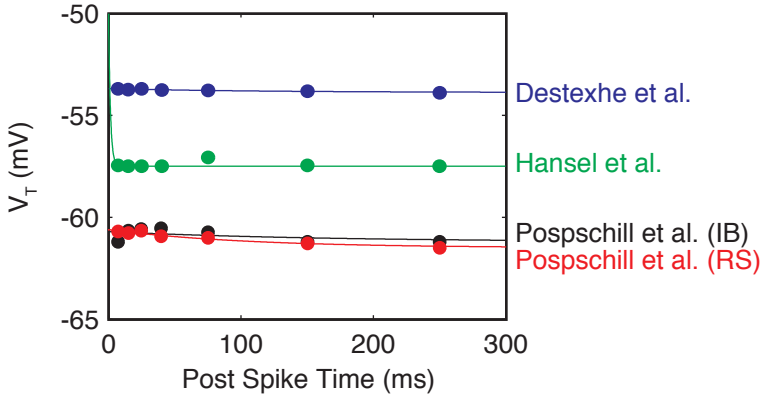

Figure 8.6: Post-spike dynamics of the spike-onset threshold of several continuous single-compartment biophysically detailed models does not match those obsevered experimentally. Models were proposed by Destexhe *et al.* (2001, blue), Hansel and van Vreeswijk (2002, green), and Pospischil *et al.* (2008, black: intrinsically bursting, and red: regular spiking). Models were integrated using the methods described in Section 3.7 with the parameters as described in the respective publications, and analysed using the dynamic I-V method introduced in Section 3.2.

inclusion of slow sodium-channel inactivation resulted in a threshold response that did not match that of experiments (Figure 8.5) additional conductances must be involved that were not accounted for in this model. The primary candidate for this is potassium-channel activation, which has been shown to mediate threshold variability in cortical pyramidal cells (Higgs and Spain 2011). The future direction of this work should be to include a model of this phenomenon alongside slow sodium-channel inactivation into the EIF model.

Finally, it should be noted that there have been many attempts at constructing continuous biophysically detailed models of neocortical pyramidal cells (Destexhe *et al.* 2001; Hansel and van Vreeswijk 2002; Pospischil *et al.* 2008; Hay *et al.* 2011, 2013), each including a multitude of conductances. However, these do not generally display the observed post-spike threshold dynamics, as illustrated for several single-compartment continuous models in Figure 8.6 (*cf.* Figure 4.7B); indeed no biophysical model that I have tested displays this response. Therefore, it is unlikely that simply including the (possibly simplified) channel dynamics from such a model would help elucidate the mechanism behind the observed threshold behaviour.

Chapter 9

Conclusions

Reduced neuron models are essential tools in computational neuroscience for investigating a wide range of phenomena, from the response properties of large neuronal-networks to the mechanisms underlying how single neurons process synaptic input. These models do not capture the full action potential dynamics, and in their simplest form are one-dimensional with a forcing function dependent only on membrane potential. In this thesis I have addressed two key challenges in the field of reduced neuron modelling. In Chapters 4 and 5 I have addressed the issue of including within- and between-population physiological heterogeneity into neocortical-network models, an aspect that is often overlooked due to the lack of sufficiently constrained parameter variance and covariance. In Chapters 6 and 8 I analysed threshold variability in thick-tufted layer 5 pyramidal cells, attempting to extend current reduced neuron models to better capture this phenomenon, and also to better understand the biological mechanism underlying the observed dynamics.

9.1 Heterogeneity in Neocortical Pyramidal Cells

Pyramidal neurons are the most abundant cortical excitatory cell and play a central computational role within the neocortical microcircuit (Figure 1.2). Although they share many key features, such as their pyramid-like cell body and spatially-extended apical dendrite, there is significant heterogeneity in their electrophysiology (Nowak *et al.* 2003; Zaitsev *et al.* 2012; van Aerde and Feldmeyer 2013; Marx and

Feldmeyer 2013). This physiological heterogeneity leads to significant differences in network synchronisation properties (Maex and De Schutter 2003) and coding efficiencies (Chelaru and Dragoi 2008) over homogeneous networks, but is often poorly captured in simulation and theoretical studies due in part to the lack of experimental data describing the variance and covariance of cellular properties. In Chapters 4 and 5 I attempted to address this issue. I measured a range of electrophysiological properties from pyramidal cell populations in neocortical layers 2/3-5 using a combination of standard and dynamic *I-V* (Badel *et al.* 2008a,b) stimulation protocols during whole-cell patch clamp recordings. I systematically analysed their variance and covariance, as well as investigating the major sources of variability.

Dynamic *I-V* curves provide a general method of fitting the voltage dependent forcing term of single-variable reduced neuron models, allowing accurate reproduction of the voltage time-course (Figure 4.5). Previously demonstrated for thick-tufted layer 5 pyramidal cells (Badel *et al.* 2008a), GABAergic neocortical interneurons (Badel *et al.* 2008b), and striatal neurons (Dorst 2013) in Chapter 4 I found that layer 2/3, layer 4, and slender-tufted layer 5 pyramidal cells also fit a forcing term of the exponential integrate-and-fire (EIF, Fourcaud-Trocmé *et al.* 2003) form, extending the scope of applicability of the model.

Going forward, the dynamic *I-V* method could be systematically applied to excitatory and inhibitory cells from across the brain to construct reduced neuron models without *a-priori* assumptions on the form of the forcing function. This opens up the possibility for theoretical studies and large-scale network simulations to be performed with computational efficiency, using mathematically tractable, experimentally verified models. More specifically, an obvious extension of the work presented in Chapters 4 and 5 would be to examine the heterogeneity display by pyramidal cells in neocortical layer 6. This layer comprises three primary pyramidal cell classes, based on their projection targets (Thomson 2010), which can be further divided into distinct morphological and physiological subgroups (Marx and Feldmeyer 2013). Distinction between layer 6 pyramidal cell classes is less straightforward than in the upper layers; this greater heterogeneity requires a clearer description of the cell's morphology and projection targets to be sure of correct classification. As such,

the methods used here applied to this layer could allow the development of an on-line tool for rapid cell classification.

Another possible direction for future work is the inclusion of additional mechanisms to the rEIF model. In particular, in Chapter 4 I note two aspects where the model performs poorly: the precise timing of bursts of action potentials (Figure 4.12A), a result of the model ignoring the dendritic extent of the cell; and the membrane response during a period of strong hyperpolarising stimuli (Figure 4.12B), due to there being no I_{h} current in the model. To improve the model's ability to capture bursts a dendritic compartment could be added to the rEIF model of the perisomatic region, as has previously been attempted for the adaptive EIF model (Clopath *et al.* 2007). If one recorded from the apical dendrite (Davie *et al.* 2006) and soma simultaneously the dynamic I-V method could be used to fit a model of both compartments; presumably the dendritic compartment would require an alternative model due to the different ionic channels expressed there in comparison to the soma. To capture the I_{h}-dependent response of the neuron the most straightforward method would be to redefine the EIF model forcing function [equation (4.4)] to capture the curvature in the I-V relationship at negative membrane potentials (Figure 4.12B main).

The key contribution I presented in Chapter 5 are algorithms to generate experimentally verified EIF and refractory EIF (rEIF) model parameter sets that adhere to the empirical marginal distributions and covariance structure (Figure 5.7). These algorithms provide a novel tool to investigate heterogeneity in neocortical networks. Furthermore, I have made all the data collected over the course of this study available along with our manuscript (accepted for publication in PLoS Computational Biology) in a freely downloadable form in the hope that other research groups can use this information to further advance our current modelling capability.

9.2 Post-spike Threshold Dynamics of Thick-tufted Layer 5 Pyramidal Cells

Action potential threshold is a dynamic property that depends on the recent voltage history (Azouz and Gray 2000, 2003; Higgs and Spain 2011), time since the last spike (Badel *et al.* 2008a,b), and recent spiking activity (Henze and Buzsáki 2001; Chacron *et al.* 2007). The threshold dynamics heavily influence precise spike timing and have implications for the cell's input-output relationship. As such, numerous works have studied these dynamics, investigating baseline fluctuations (Platkiewicz and Brette 2010; Higgs and Spain 2011; Platkiewicz and Brette 2011; Fontaine *et al.* 2014), spike-triggered response (Lindner and Longtin 2005), and spike-frequency adaptation (Benda and Herz 2003).

In Chapter 6 I looked at several extensions to the standard EIF model. The rEIF model is the standard EIF model [equation (4.4)] coupled with the renewal process dynamics of the membrane conductance, spike-onset threshold and resting potential [equations (4.5)-(4.7)], and performs significantly better than the standard EIF model (Badel *et al.* 2008a,b, Figure 6.5). The performance gain on extending the rEIF model (Badel *et al.* 2008a) from a renewal process to include threshold accumulation was, although statistically significant, only very small (Figure 6.5). A two variable model of the form of equation (6.6) was a vast improvement over the standard EIF model, although it did not perform as well as the other two extensions, which both included the additional refractory dynamics of the conductance and resting potential (Figure 6.5). These results suggest that a simple renewal process model is good enough to capture the majority of the cells' responses, although by definition a renewal process will not exhibit experimentally observed inter-spike interval correlations (Chacron *et al.* 2001; Schwalger and Lindner 2013).

Reduced neuron models have the advantage of being relatively simple to analyse. Indeed, the two variable model can be reduced to a single dimension, taking the same form as the standard EIF model with an additional exponential drift current [equations (6.8) and (6.9)]. As noted by Badel *et al.* (2008b), when the membrane and threshold timescales are equal this model becomes mathematically equivalent

to the standard EIF model but with a lower reset. My experimental results show that these timescales are indeed similar (Figure 6.4C), suggesting that a low reset is equivalent to the experimentally observed spike-triggered threshold jump and subsequent decay (Figures 4.7 and 6.1). This perhaps explains the success of simple reduced neuron models in capturing experimental responses; the reset in these models is typically around the resting potential (Burkitt 2006a,b), tens of millivolts lower than the typical reset of a thick-tufted layer 5 pyramidal cell (Figure 4.4).

In Chapter 7 I examined the population response properties of the two variable EIF model utilising the previously introduced threshold integration scheme (Richardson 2007), extending previous analysis of the leaky integrate-and-fire model (Lindner and Longtin 2005) to include an arbitrary threshold jump size. I found that, by taking a perturbative approach to solving the corresponding Fokker-Planck equation, I could predict the population response across the entire physiological range of the membrane to threshold timescale ratio in both sub-threshold noise driven and supra-threshold quasi-deterministic firing regimes (Figure 7.1C). Furthermore, the spike-train power spectrum revealed that in a sub-threshold noise driven firing regime populations of 2vEIF neurons displayed little coherence resonance, whereas during a supra-threshold quasi-deterministic firing regime a strong coherence resonance was apparent at approximately 20 and 50 Hz.

Extending the work of Richardson (2007, 2008) and Lindner and Longtin (2005) to analyse populations of EIF neurons with an arbitrary post-spike jump in threshold involved only a small increase in mathematical compliexity. The next obvious extension is to also include the post-spike dynamics of the membrane conductance (Figure 4.7A) and resting potential (Figure 4.7C), since these additions greatly improve the fit quality of the model (Figure 6.5). However, this will greatly increase the complexity of the Fokker-Planck equation [equation (7.1)] by adding two extra dimensions. Finally, investigating the effect of parameter modulation and connectivity within the population, as done by Richardson (2007, 2008), would also be advantageous, as would the inclusion of the heterogeneity investigated in Chapters 4 and 5.

Sodium-channel inactivation has been shown to modulate spike threshold (Flei-

dervish *et al.* 1996; Fleidervish and Gutnick 1996; Fricker *et al.* 1999; Azouz and Gray 2003; Arganda *et al.* 2007). The slow component of inactivation has a timescale similar to that of the empirical spike-triggered threshold decay (Toib *et al.* 1998; Soudry and Meir 2012). In Chapter 8 I examined the effect of slow sodium-channel inactivation on threshold dynamics by including it first into an existing spiking-neuron model (Wang and Buzsáki 1996), followed by the EIF model. Including this mechanism resulted in, to first order, a threshold of the same mono-exponential form of that observed experimentally but with a post-spike jump restricted to $\sim \mathcal{O}(\Delta_{\mathrm{T}})$, an order of magnitude smaller than the empirical measurement (Figure 4.10D). Furthermore, the full logarithmic form derived from the channel's inclusion [equation (8.14)] did not fit experimental measurements when restricted to biophysically realistic parameter ranges (Figure 8.5). Since slow inactivation of voltage-gated sodium channels is known to reduce membrane excitability (Vilin and Ruben 2001) it must be supplemented by additional mechanisms to yield the observed response. A prime candidate for this is potassium-channel activation; the blockade of Kv1 channels has been shown to reduce threshold variability in cortical neurons (Higgs and Spain 2011). Including a model of this mechanism alongside slow sodium-channel inactivation into the EIF model would prove useful for better understanding the experimentally observed threshold response.

Bibliography

van Aerde KI and Feldmeyer D (2013). Morphological and Physiological Characterization of Pyramidal Neuron Subtypes in Rat Medial Prefrontal Cortex. *Cerebral Cortex*. **25**: 788–805.

Alijani AK and Richardson MJE (2011). Rate response of neurons subject to fast or frozen noise: From stochastic and homogeneous to deterministic and heterogeneous populations. *Physical Review E*. **84**: 011919.

Arganda S, Guantes R, and de Polavieja GG (2007). Sodium pumps adapt spike bursting to stimulus statistics. *Nature Neuroscience*. **10**: 1467–1473.

Azouz R and Gray CM (2000). Dynamic spike threshold reveals a mechanism for synaptic coincidence detection in cortical neurons in vivo. *Proceedings of the National Academy of Sciences*. **97**: 8110–8115.

— (2003). Adaptive coincidence detection and dynamic gain control in visual cortical neurons in vivo. *Neuron*. **37**: 513–523.

Badel L, Lefort S, Brette R, Petersen CCH, Gerstner W, and Richardson MJE (2008a). Dynamic I-V Curves Are Reliable Predictors of Naturalistic Pyramidal-Neuron Voltage Traces. *Journal of Neurophysiology*. **99**: 656–666.

Badel L, Lefort S, Berger TK, Petersen CCH, Gerstner W, and Richardson MJE (2008b). Extracting non-linear integrate-and-fire models from experimental data using dynamic I-V curves. *Biological Cybernetics*. **99**: 361–370.

Bean BP (2007). The action potential in mammalian central neurons. *Nature Reviews Neuroscience*. **8**: 451–465.

Benda J and Herz AV (2003). A universal model for spike-frequency adaptation. *Neural computation*. **15**: 2523–2564.

Biel M, Wahl-Schott C, Michalakis S, and Zong X (2009). Hyperpolarization-Activated Cation Channels: From Genes to Function. *Physiological reviews*. **89**: 847–885.

Brecht M and Sakmann B (2002). Dynamic representation of whisker deflection by synaptic potentials in spiny stellate and pyramidal cells in the barrels and septa of layer 4 rat somatosensory cortex. *The Journal of Physiology*. **543**: 49–70.

Breiman L (2001). Random forests. *Machine learning*. **45**: 5–32.

Brette R (2013). Sharpness of spike initiation in neurons explained by compartmentalization. *PLoS Computational Biology*. **9**: e1003338.

Brette R and Gerstner W (2005). Adaptive exponential integrate-and-fire model as an effective description of neuronal activity. *Journal of Neurophysiology*. **94**: 3637–3642.

Brette R, Piwkowska Z, Monier C, Rudolph-Lilith M, Fournier J, Levy M, Frégnac Y, Bal T, and Destexhe A (2008). High-Resolution Intracellular Recordings Using a Real-Time Computational Model of the Electrode. *Neuron*. **59**: 379–391.

Brette R, Piwkowska Z, Rudolph M, Bal T, and Destexhe A (2007). A non-parametric electrode model for intracellular recording. *Neurocomputing*. **70**: 1597–1601.

Brunel N (2000). Dynamics of sparsely connected networks of excitatory and inhibitory spiking neurons. *Journal of Computational Neuroscience*. **8**: 183–208.

Brunel N and Hakim V (1999). Fast global oscillations in networks of integrate-and-fire neurons with low firing rates. *Neural computation*. **11**: 1621–1671.

Brunel N, Chance F, Fourcaud N, and Abbott L (2001). Effects of Synaptic Noise and Filtering on the Frequency Response of Spiking Neurons. *Physical Review Letters*. **86**: 2186–2189.

Brunel N, Hakim V, and Richardson MJE (2003). Firing-rate resonance in a generalized integrate-and-fire neuron with subthreshold resonance. *Physical Review E*. **67**: 051916.

Bugbee NM and Goldman-Rakic PS (1983). Columnar organization of corticocortical projections in squirrel and rhesus monkeys: similarity of column width in species differing in cortical volume. *The Journal of Comparative Neurology*. **220**: 355–364.

Burkitt AN (2006a). A Review of the Integrate-and-fire Neuron Model: I. Homogeneous Synaptic Input. *Biological Cybernetics*. **95**: 1–19.

— (2006b). A review of the integrate-and-fire neuron model: II. Inhomogeneous synaptic input and network properties. *Biological Cybernetics*. **95**: 97–112.

Buxhoeveden DP and Casanova MF (2002). The minicolumn hypothesis in neuroscience. *Brain*. **125**: 935–951.

Buzsáki G and Mizuseki K (2014). The log-dynamic brain: how skewed distributions affect network operations. *Nature Reviews Neuroscience*. **15**: 264–278.

Buzsáki G and Wang XJ (2012). Mechanisms of Gamma Oscillations. *Annual Review of Neuroscience*. **35**: 203–225.

Câteau H and Reyes A (2006). Relation between Single Neuron and Population Spiking Statistics and Effects on Network Activity. *Physical Review Letters*. **96**: 058101.

Cauller L (1995). Layer I of primary sensory neocortex: where top-down converges upon bottom-up. *Behavioural brain research*. **71**: 163–170.

Cauller LJ and Connors BW (1994). Synaptic physiology of horizontal afferents to layer I in slices of rat SI neocortex. *The Journal of neuroscience*. **14**: 751–762.

Chacron MJ, Lindner B, and Longtin A (2007). Threshold fatigue and information transfer. *Journal of Computational Neuroscience*. **23**: 301–311.

Chacron MJ, Longtin A, and Maler L (2001). Negative interspike interval correlations increase the neuronal capacity for encoding time-dependent stimuli. *Journal of Neuroscience*. **21**: 5328–5343.

Chacron MJ, Pakdaman K, and Longtin A (2003). Interspike interval correlations, memory, adaptation, and refractoriness in a leaky integrate-and-fire model with threshold fatigue. *Neural computation*. **15**: 253–278.

Chadderton P, Schaefer AT, Williams SR, and Margrie TW (2014). Sensory-evoked synaptic integration in cerebellar and cerebral cortical neurons. *Nature Publishing Group*. **15**: 71–83.

Chagnac-Amitai Y, Luhmann HJ, and Prince DA (1990). Burst generating and regular spiking layer 5 pyramidal neurons of rat neocortex have different morphological features. *The Journal of Comparative Neurology*. **296**: 598–613.

Chelaru MI and Dragoi V (2008). Efficient coding in heterogeneous neuronal populations. *Proceedings of the National Academy of Sciences of the United States of America*. **105**: 16344–16349.

Chi XX and Nicol GD (2007). Manipulation of the Potassium Channel Kv1.1 and Its Effect on Neuronal Excitability in Rat Sensory Neurons. *Journal of Neurophysiology*. **98**: 2683–2692.

Clopath C, Jolivet R, Rauch A, Lüscher HR, and Gerstner W (2007). Predicting neuronal activity with simple models of the threshold type: Adaptive Exponential Integrate-and-Fire model with two compartments. *Neurocomputing*. **70**: 1668–1673.

Connors BW, Gutnick MJ, and Prince DA (1982). Electrophysiological properties of neocortical neurons in vitro. *Journal of Neurophysiology*. **48**: 1302–1320.

Connors BW and Gutnick MJ (1990). Intrinsic firing patterns of diverse neocortical neurons. *Trends in Neurosciences*. **13**: 99–104.

Constantinople CM and Bruno RM (2013). Deep Cortical Layers Are Activated Directly by Thalamus. *Science*. **340**: 1591–1594.

Coombs JS, Eccles JC, and Fatt P (1955). The inhibitory suppression of reflex discharges from motoneurones. *The Journal of Physiology*. **130**: 396.

Cruikshank SJ, Lewis TJ, and Connors BW (2007). Synaptic basis for intense thalamocortical activation of feedforward inhibitory cells in neocortex. *Nature Neuroscience*.

Cutsuridis V, Cobb S, and Graham BP (2009a). Encoding and retrieval in a model of the hippocampal CA1 microcircuit. *Hippocampus*: NA–NA.

Cutsuridis V, Wennekers T, Graham BP, Vida I, and Taylor JG (2009b). Microcircuits–their structure, dynamics and role for brain function. *Neural networks : the official journal of the International Neural Network Society*. **22**: 1037–1038.

Davie JT, Kole MHP, Letzkus JJ, Rancz EA, Spruston N, Stuart GJ, and Häusser M (2006). Dendritic patch-clamp recording. *Nature Protocols*. **1**: 1235–1247.

De Kock CPJ, Bruno RM, Spors H, and Sakmann B (2007). Layer- and cell-type-specific suprathreshold stimulus representation in rat primary somatosensory cortex. *The Journal of Physiology*. **581**: 139–154.

De Polavieja GG (2005). Stimulus History Reliably Shapes Action Potential Waveforms of Cortical Neurons. *Journal of Neuroscience*. **25**: 5657–5665.

Dean P, Porrill J, Ekerot CF, and Jörntell H (2009). The cerebellar microcircuit as anadaptive filter: experimental andcomputational evidence. *Nature Publishing Group*. **11**: 30–43.

Deco G, Jirsa VK, Robinson PA, Breakspear M, and Friston K (2008). The dynamic brain: from spiking neurons to neural masses and cortical fields. *PLoS Computational Biology*. **4**: e1000092.

DeFelipe J (1997). Types of neurons, synaptic connections and chemical characteristics of cells immunoreactive for calbindin-D28K, parvalbumin and calretinin in the neocortex. *Journal of chemical neuroanatomy*. **14**: 1–19.

DeFelipe J and Fariñas I (1992). The pyramidal neuron of the cerebral cortex: morphological and chemical characteristics of the synaptic inputs. *Progress in neurobiology*. **39**: 563–607.

Dempster AP, Laird NM, and Rubin DB (1977). Maximum Likelihood from Incomplete Data via the EM Algorithm. *Journal of the Royal Statistical Society. Series B*. **39**: 1–38.

Destexhe A, Rudolph M, Fellous JM, and Sejnowski TJ (2001). Fluctuating synaptic conductances recreate in vivo-like activity in neocortical neurons. *NSC*. **107**: 13–24.

Dorst M (2013). Electrophysiological characterization of striatal neurons through dynamic I-V curves. *Masters Thesis, Royal Institute of Technology and the Karolinska Institute, Sweden*: 1–64.

Douglas RJ and Martin KAC (2004). Neuronal Circuits of the Neocortex. *Annual Review of Neuroscience*. **27**: 419–451.

Druckmann S, Banitt Y, Gidon A, Schürmann F, Markram H, and Segev I (2007). A novel multiple objective optimization framework for constraining conductance-based neuron models by experimental data. *Frontiers in neuroscience*. **1**: 7–18.

Eliasmith C, Stewart TC, Choo X, Bekolay T, DeWolf T, Tang Y, and Rasmussen D (2012). A Large-Scale Model of the Functioning Brain. *Science*. **338**: 1202–1205.

Feldmeyer D (2012). Excitatory neuronal connectivity in the barrel cortex. *Frontiers in Neuroanatomy*. **6**: 24.

Feldmeyer D, Lübke J, Angus Silver R, and Sakmann B (2002). Synaptic connections between layer 4 spiny neurone-layer 2/3 pyramidal cell pairs in juvenile rat barrel cortex: physiology and anatomy of interlaminar signalling within a cortical column. *The Journal of Physiology*. **538**: 803–822.

Felleman DJ and Van Essen DC (1991). Distributed hierarchical processing in the primate cerebral cortex. *Cerebral cortex (New York, N.Y. : 1991)*. **1**: 1–47.

FitzHugh R (1955). Mathematical models of threshold phenomena in the nerve membrane. *The bulletin of mathematical biophysics*. **17**: 257–278.

— (1961). Impulses and Physiological States in Theoretical Models of Nerve Membrane. *Biophysical Journal*. **1**: 445–466.

Fleidervish IA, Friedman A, and Gutnick MJ (1996). Slow inactivation of Na^+ current and slow cumulative spike adaptation in mouse and guinea-pig neocortical neurones in slices. *The Journal of Physiology*. **493**: 83–97.

Fleidervish IA and Gutnick MJ (1996). Kinetics of slow inactivation of persistent sodium current in layer V neurons of mouse neocortical slices. *Journal of Neurophysiology*. **76**: 2125–2130.

Fontaine B, Peña JL, and Brette R (2014). Spike-threshold adaptation predicted by membrane potential dynamics in vivo. *PLoS Computational Biology*. **10**: e1003560.

Fourcaud-Trocmé N, Hansel D, van Vreeswijk C, and Brunel N (2003). How spike generation mechanisms determine the neuronal response to fluctuating inputs. *Journal of Neuroscience*. **23**: 11628–11640.

Fricker D, Verheugen JA, and Miles R (1999). Cell-attached measurements of the firing threshold of rat hippocampal neurones. *The Journal of Physiology*. **517 (Pt 3)**: 791–804.

Gal A, Eytan D, Wallach A, Sandler M, Schiller J, and Marom S (2010). Dynamics of Excitability over Extended Timescales in Cultured Cortical Neurons. *Journal of Neuroscience*. **30**: 16332–16342.

Gang H, Ditzinger T, Ning C, and Haken H (1993). Stochastic resonance without external periodic force. *Physical Review Letters*. **71**: 807–810.

Gao WJ and Zheng ZH (2004). Target-specific differences in somatodendritic morphology of layer V pyramidal neurons in rat motor cortex. *The Journal of Comparative Neurology*. **476**: 174–185.

Gasparini S (2004). On the Initiation and Propagation of Dendritic Spikes in CA1 Pyramidal Neurons. *Journal of Neuroscience*. **24**: 11046–11056.

Gentet LJ, Kremer Y, Taniguchi H, Huang ZJ, Staiger JF, and Petersen CCH (2012). Unique functional properties of somatostatin-expressing GABAergic neurons in mouse barrel cortex. *Nature Publishing Group*. **15**: 607–612.

Gerstner W (2000). Population dynamics of spiking neurons: fast transients, asynchronous states, and locking. *Neural computation*. **12**: 43–89.

Gerstner W and Naud R (2009). How Good Are Neuron Models? *Science*. **326**: 379–380.

Gerstner W and Kistler WM (2002). Spiking neuron models: Single neurons, populations, plasticity. Cambridge university press.

Giacomelli G, Giudici M, Balle S, and Tredicce J (2000). Experimental evidence of coherence resonance in an optical system. *Physical Review Letters*. **84**: 3298–3301.

Goldberg EM, Clark BD, Zagha E, Nahmani M, Erisir A, and Rudy B (2008). K+ Channels at the Axon Initial Segment Dampen Near-Threshold Excitability of Neocortical Fast-Spiking GABAergic Interneurons. *Neuron*. **58**: 387–400.

Goldin AL (2003). Mechanisms of sodium channel inactivation. *Current Opinion in Neurobiology*. **13**: 284–290.

Grillner S and Graybiel AM (2006). Microcircuits. The Interface Between Neurons and Global Brain Function. MIT Press.

Grubb MS, Shu Y, Kuba H, Rasband MN, Wimmer VC, and Bender KJ (2011). Short- and long-term plasticity at the axon initial segment. *Journal of Neuroscience*. **31**: 16049–16055.

Guan D, Lee JCF, Higgs MH, Spain WJ, and Foehring RC (2007). Functional Roles of Kv1 Channels in Neocortical Pyramidal Neurons. *Journal of Neurophysiology*. **97**: 1931–1940.

Gupta A, Wang Y, and Markram H (2000). Organizing principles for a diversity of GABAergic interneurons and synapses in the neocortex. *Science*. **287**: 273–278.

Gur M and Snodderly DM (2008). Physiological differences between neurons in layer 2 and layer 3 of primary visual cortex (V1) of alert macaque monkeys. *The Journal of Physiology*. **586**: 2293–2306.

Hansel D and van Vreeswijk C (2002). How noise contributes to contrast invariance of orientation tuning in cat visual cortex. *Journal of Neuroscience*. **22**: 5118–5128.

Harris KD and Mrsic-Flogel TD (2013). Cortical connectivity and sensory coding. *Nature*. **503**: 51–58.

Harris NC and Constanti A (1995). Mechanism of block by ZD 7288 of the hyperpolarization-activated inward rectifying current in guinea pig substantia nigra neurons in vitro. *Journal of Neurophysiology*. **74**: 2366–2378.

Hay E, Hill S, Schürmann F, Markram H, and Segev I (2011). Models of Neocortical Layer 5b Pyramidal Cells Capturing a Wide Range of Dendritic and Perisomatic Active Properties. *PLoS Computational Biology*. **7**: e1002107.

Hay E, Schurmann F, Markram H, and Segev I (2013). Preserving axosomatic spiking features despite diverse dendritic morphology. *Journal of Neurophysiology*. **109**: 2972–2981.

Helmstaedter M, de Kock CPJ, Feldmeyer D, Bruno RM, and Sakmann B (2007). Reconstruction of an average cortical column in silico. *Brain Research Reviews*. **55**: 193–203.

Henze DA and Buzsáki G (2001). Action potential threshold of hippocampal pyramidal cells in vivo is increased by recent spiking activity. *NSC*. **105**: 121–130.

Herculano-Houzel S, Collins CE, Wong P, Kaas JH, and Lent R (2008). The basic nonuniformity of the cerebral cortex. *Proceedings of the National Academy of Sciences of the United States of America*. **105**: 12593–12598.

Hestrin S and Armstrong WE (1996). Morphology and physiology of cortical neurons in layer I. *The Journal of neuroscience*. **16**: 5290–5300.

Higgs MH and Spain WJ (2011). Kv1 channels control spike threshold dynamics and spike timing in cortical pyramidal neurones. *The Journal of Physiology*: no–no.

Hines ML and Carnevale NT (1997). The NEURON simulation environment. *Neural computation*. **9**: 1179–1209.

Hodgkin AL and Huxley AF (1952a). A quantitative description of membrane current and its application to conduction and excitation in nerve. *The Journal of Physiology*. **117**: 500–544.

— (1952b). Currents carried by sodium and potassium ions through the membrane of the giant axon of Loligo. *The Journal of Physiology*. **116**: 449–472.

— (1952c). The components of membrane conductance in the giant axon of Loligo. *The Journal of Physiology*. **116**: 473–496.

Hodgkin AL and Huxley AF (1952d). The dual effect of membrane potential on sodium conductance in the giant axon of Loligo. *The Journal of Physiology*. **116**: 497–506.

Hooks BM, Hires SA, Zhang YX, Huber D, Petreanu L, Svoboda K, and Shepherd GMG (2011). Laminar analysis of excitatory local circuits in vibrissal motor and sensory cortical areas. *PLoS Biology*. **9**: e1000572.

Horton JC and Adams DL (2005). The cortical column: a structure without a function. *Philosophical transactions of the Royal Society of London. Series B, Biological sciences*. **360**: 837–862.

Howard A, Tamás G, and Soltesz I (2005). Lighting the chandelier: new vistas for axo-axonic cells. *Trends in Neurosciences*. **28**: 310–316.

Hubel DH and Wiesel TN (1962). Receptive fields, binocular interaction and functional architecture in the cat's visual cortex. *The Journal of Physiology*. **160**: 106–154.

Hunsberger E, Scott M, and Eliasmith C (2014). The competing benefits of noise and heterogeneity in neural coding. *Neural computation*. **26**: 1600–1623.

Huys QJMQ, Ahrens MBM, and Paninski L (2006). Efficient estimation of detailed single-neuron models. *Journal of Neurophysiology*. **96**: 872–890.

Huys QJM and Paninski L (2009). Smoothing of, and parameter estimation from, noisy biophysical recordings. *PLoS Computational Biology*. **5**: e1000379.

Izhikevich EM (2003). Simple model of spiking neurons. *IEEE Transactions on Neural Networks*. **14**: 1569–1572.

— (2010). Hybrid spiking models. *Philosophical Transactions of the Royal Society A: Mathematical, Physical and Engineering Sciences*. **368**: 5061–5070.

Izhikevich EM (2007). Dynamical Systems in Neuroscience. MIT Press.

Izhikevich EM and Edelman GM (2008). Large-scale model of mammalian thalamocortical systems. *Proceedings of the National Academy of Sciences of the United States of America*. **105**: 3593–3598.

Jolivet R, Lewis TJ, and Gerstner W (2004). Generalized integrate-and-fire models of neuronal activity approximate spike trains of a detailed model to a high degree of accuracy. *Journal of Neurophysiology*. **92**: 959–976.

Jolivet R, Rauch A, Lüscher HR, and Gerstner W (2006a). Integrate-and-Fire models with adaptation are good enough: predicting spike times under random current injection. *Advances in Neural Information Processing Systems*. **18**: 595–602.

— (2006b). Predicting spike timing of neocortical pyramidal neurons by simple threshold models. *Journal of Computational Neuroscience*. **21**: 35–49.

Jolivet R, Schürmann F, Berger TK, Naud R, Gerstner W, and Roth A (2008). The quantitative single-neuron modeling competition. *Biological Cybernetics*. **99**: 417–426.

Jones EG (1999). Making brain connections: neuroanatomy and the work of TPS Powell, 1923-1996. Vol. 22. Department of Anatomy and Neurobiology, University of California, Irvine 92697-1280, USA. ejones@ucdavis.edu.

— (2000). Microcolumns in the cerebral cortex. *Proceedings of the National Academy of Sciences*. **97**: 5019–5021.

Kandel ER, Schwartz JH, and Jessell TM (2000). Principles of neural science. 4th ed. McGraw-Hill New York.

Kerr MI, Wall MJ, and Richardson MJE (2013). Adenosine A 1-receptor activation mediates the developmental shift at layer-5 pyramidal-cell synapses and is a determinant of mature synaptic strength. *The Journal of Physiology*: 3371–3380.

Kim HG and Connors BW (1993). Apical dendrites of the neocortex: correlation between sodium-and calcium-dependent spiking and pyramidal cell morphology. *The Journal of neuroscience*. **13**: 5301–5311.

Kim J, Matney CJ, Blankenship A, Hestrin S, and Brown SP (2014). Layer 6 corticothalamic neurons activate a cortical output layer, layer 5a. *Journal of Neuroscience*. **34**: 9656–9664.

Kistler WM, Gerstner W, and van Hemmen JL (1997). Reduction of the Hodgkin-Huxley equations to a single-variable threshold model. *Neural computation*. **9**: 1015–1045.

Kobayashi R, Tsubo Y, and Shinomoto S (2009). Made-to-order spiking neuron model equipped with a multi-timescale adaptive threshold. *Frontiers in Computational Neuroscience*. **3**: 9–9.

Kozloski J, Hamzei-Sichani F, and Yuste R (2001). Stereotyped position of local synaptic targets in neocortex. *Science*. **293**: 868–872.

Lapicque L (1907). Recherches quantitatives sur l'excitation électrique des nerfs traitée comme une polarisation. *Journal de Physiologie et de Pathologie Générale*. **9**: 620–635.

Laramee ME, Rockland KS, Prince S, Bronchti G, and Boire D (2013). Principal Component and Cluster Analysis of Layer V Pyramidal Cells in Visual and Non-Visual Cortical Areas Projecting to the Primary Visual Cortex of the Mouse. *Cerebral Cortex*. **23**: 714–728.

Larkman AU (1991). Dendritic morphology of pyramidal neurones of the visual cortex of the rat: I. Branching patterns. *The Journal of Comparative Neurology*. **306**: 307–319.

Larkum ME (2004). Top-down Dendritic Input Increases the Gain of Layer 5 Pyramidal Neurons. *Cerebral Cortex*. **14**: 1059–1070.

Larkum ME, Nevian T, Sandler M, Polsky A, and Schiller J (2009). Synaptic Integration in Tuft Dendrites of Layer 5 Pyramidal Neurons: A New Unifying Principle. *Science*. **325**: 756–760.

Larkum ME, Zhu JJ, and Sakmann B (1999). A new cellular mechanism for coupling inputs arriving at different cortical layers. *Nature*. **398**: 338–341.

Ledoux E and Brunel N (2011). Dynamics of networks of excitatory and inhibitory neurons in response to time-dependent inputs. *Frontiers in Computational Neuroscience*. **5**: 25.

Lee CC and Sherman SM (2009). Glutamatergic inhibition in sensory neocortex. *Cerebral Cortex*. **19**: 2281–2289.

Lee S, Kruglikov I, Huang ZJ, Fishell G, and Rudy B (2013). A disinhibitory circuit mediates motor integration in the somatosensory cortex. *Nature Publishing Group*. **16**: 1662–1670.

Letinic K, Zoncu R, and Rakic P (2002). Origin of GABAergic neurons in the human neocortex. *Nature*. **417**: 645–649.

Lindner B, Garcia-Lazaro JA, Neiman A, and Schimansky-Geier L (2004). Effects of noise in excitable systems. *Physics Reports*. **392**: 321–424.

Lindner B and Longtin A (2005). Effect of an exponentially decaying threshold on the firing statistics of a stochastic integrate-and-fire neuron. *Journal of Theoretical Biology*. **232**: 505–521.

Lindner B, Schimansky-Geier L, and Longtin A (2002). Maximizing spike train coherence or incoherence in the leaky integrate-and-fire model. *Physical Review E*. **66**: 031916.

Liu LI and Liu JM (1995). Experimental observation of stochastic resonancelike behavior of autonomous motion in weakly ionized rf magnetoplasmas. *Physical Review Letters*. **74**: 3161–3164.

Longtin A (1997). Autonomous stochastic resonance in bursting neurons. *Physical Review E*. **55**: 868.

Losonczy A and Magee JC (2006). Integrative Properties of Radial Oblique Dendrites in Hippocampal CA1 Pyramidal Neurons. *Neuron*. **50**: 291–307.

Luccioli S and Politi A (2010). Irregular Collective Behavior of Heterogeneous Neural Networks. *Physical Review Letters*. **105**: 158104.

Lui JH, Hansen DV, and Kriegstein AR (2011). Development and Evolution of the Human Neocortex. *Cell*. **146**: 18–36.

Lumer ED, Edelman GM, and Tononi G (1997). Neural dynamics in a model of the thalamocortical system. I. Layers, loops and the emergence of fast synchronous rhythms. *Cerebral cortex (New York, N.Y. : 1991)*. **7**: 207–227.

Maex R and De Schutter E (2003). Resonant synchronization in heterogeneous networks of inhibitory neurons. *Journal of Neuroscience*. **23**: 10503–10514.

Markram H (2006). The blue brain project. *Nature Reviews Neuroscience*. **7**: 153–160.

Markram H, Gerstner W, and Sjöström PJ (2011). A history of spike-timing-dependent plasticity. *Frontiers in synaptic neuroscience*. **3**: 4.

Markram H, Toledo-Rodriguez M, Wang Y, Gupta A, Silberberg G, and Wu C (2004). Interneurons of the neocortical inhibitory system. *Nature Reviews Neuroscience*. **5**: 793–807.

Marx M and Feldmeyer D (2013). Morphology and Physiology of Excitatory Neurons in Layer 6b of the Somatosensory Rat Barrel Cortex. *Cerebral Cortex*. **23**: 2803–2817.

McCormick DA, Shu Y, and Yu Y (2007). Neurophysiology: Hodgkin and Huxley model — still standing? *Nature*. **445**: E1–E2.

Mejias JF and Longtin A (2014). Differential effects of excitatory and inhibitory heterogeneity on the gain and asynchronous state of sparse cortical networks. *Frontiers in Computational Neuroscience*. **8**: 107.

Mensi S, Naud R, Pozzorini C, Avermann M, Petersen CCH, and Gerstner W (2012). Parameter extraction and classification of three cortical neuron types reveals two distinct adaptation mechanisms. *Journal of Neurophysiology*. **107**: 1756–1775.

Meyer HS, Wimmer VC, Oberlaender M, de Kock CPJ, Sakmann B, and Helmstaedter M (2010). Number and laminar distribution of neurons in a thalamocortical projection column of rat vibrissal cortex. *Cerebral Cortex*. **20**: 2277–2286.

Momin A, Cadiou H, Mason A, and McNaughton PA (2008). Role of the hyperpolarization-activated current Ih in somatosensory neurons. *The Journal of Physiology*. **586**: 5911–5929.

Monsivais P and Rubel EW (2001). Accommodation enhances depolarizing inhibition in central neurons. *Journal of Neuroscience*. **21**: 7823–7830.

Montoro RJ, López-Barneo J, and Jassik-Gerschenfeld D (1988). Differential burst firing modes in neurons of the mammalian visual cortex in vitro. *Brain research*. **460**: 168–172.

Moreno R, de la Rocha J, Renart A, and Parga N (2002). Response of Spiking Neurons to Correlated Inputs. *Physical Review Letters*. **89**: 288101.

Moreno-Bote R and Parga N (2005). Membrane Potential and Response Properties of Populations of Cortical Neurons in the High Conductance State. *Physical Review Letters*. **94**: 088103.

Morris C and Lecar H (1981). Voltage oscillations in the barnacle giant muscle fiber. *Biophysical Journal*. **35**: 193–213.

Mountcastle VB, Davies PW, and Berman AL (1957). Response properties of neurons of cat's somatic sensory cortex to peripheral stimuli. *Journal of Neurophysiology*. **20**: 374–407.

Nagumo J, Arimoto S, and Yoshizawa S (1962). An Active Pulse Transmission Line Simulating Nerve Axon. *Proceedings of the IRE*. **50**: 2061–2070.

Naundorf B, Wolf F, and Volgushev M (2006). Unique features of action potential initiation in cortical neurons. *Nature*. **440**: 1060–1063.

Nevian T, Larkum ME, Polsky A, and Schiller J (2007). Properties of basal dendrites of layer 5 pyramidal neurons: a direct patch-clamp recording study. *Nature Neuroscience*. **10**: 206–214.

Nicola W and Campbell SA (2013). Mean-field models for heterogeneous networks of two-dimensional integrate and fire neurons. *Frontiers in Computational Neuroscience*. **7**: 184.

Nowak LG, Azouz R, Sanchez-Vives MV, Gray CM, and McCormick DA (2003). Electrophysiological classes of cat primary visual cortical neurons in vivo as revealed by quantitative analyses. *Journal of Neurophysiology*. **89**: 1541–1566.

Oberlaender M, de Kock CPJ, Bruno RM, Ramirez A, Meyer HS, Dercksen VJ, Helmstaedter M, and Sakmann B (2012). Cell Type-Specific Three-Dimensional Structure of Thalamocortical Circuits in a Column of Rat Vibrissal Cortex. *Cerebral Cortex*. **22**: 2375–2391.

Oláh S, Füle M, Komlósi G, Varga C, Báldi R, Barzó P, and Tamás G (2009). Regulation of cortical microcircuits by unitary GABA-mediated volume transmission. *Nature*. **461**: 1278–1281.

Olsen SR, Bortone DS, Adesnik H, and Scanziani M (2012). Gain control by layer six in corticalcircuits of vision. *Nature*. **482**: 47–52.

Oswald MJ, Tantirigama MLS, Sonntag I, Hughes SM, and Empson RM (2013). Diversity of layer 5 projection neurons in the mouse motor cortex. *Frontiers in cellular neuroscience*. **7**: 174.

Padmanabhan K and Urban NN (2010). Intrinsic biophysical diversity decorrelates neuronal firing while increasing information content. *Nature Publishing Group*. **13**: 1276–1282.

Palmer LM, Shai AS, Reeve JE, Anderson HL, Paulsen O, and Larkum ME (2014). NMDA spikes enhance action potential generation during sensory input. *Nature Publishing Group*. **17**: 383–390.

Palmer LM and Stuart GJ (2006). Site of action potential initiation in layer 5 pyramidal neurons. *Journal of Neuroscience*. **26**: 1854–1863.

Paninski L, Pillow JW, and Simoncelli EP (2004). Maximum likelihood estimation of a stochastic integrate-and-fire neural encoding model. *Neural computation*. **16**: 2533–2561.

Paninski L, Pillow J, and Simoncelli EP (2005). Comparing integrate-and-fire models estimated using intracellular and extracellular data. *Neurocomputing*. **65-66**: 379–385.

Petreanu L, Gutnisky DA, Huber D, Xu NL, O'Connor DH, Tian L, Looger L, and Svoboda K (2013). Activity in motor–sensory projections reveals distributed coding in somatosensation. *Nature*. **489**: 299–303.

Pikovsky AS and Kurths J (1997). Coherence Resonance in a Noise-Driven Excitable System. *Physical Review Letters*. **78**: 775–778.

Platkiewicz J and Brette R (2010). A Threshold Equation for Action Potential Initiation. *PLoS Computational Biology*. **6**: e1000850.

— (2011). Impact of Fast Sodium Channel Inactivation on Spike Threshold Dynamics and Synaptic Integration. *PLoS Computational Biology*. **7**: e1001129.

Plesser HE and Gerstner W (2000). Escape rate models for noisy integrate-and-free neurons. *Neurocomputing*. **32**: 219–224.

Pospischil M, Toledo-Rodriguez M, Monier C, Piwkowska Z, Bal T, Frégnac Y, Markram H, and Destexhe A (2008). Minimal Hodgkin–Huxley type models for different classes of cortical and thalamic neurons. *Biological Cybernetics*. **99**: 427–441.

Postnov DE, Han SK, Yim TG, and Sosnovtseva OV (1999). Experimental observation of coherence resonance in cascaded excitable systems. *Physical Review Letters*. **59**: 3791–3794.

Prescott SA, De Koninck Y, and Sejnowski TJ (2008). Biophysical basis for three distinct dynamical mechanisms of action potential initiation. *PLoS Computational Biology*. **4**: e1000198.

Rakic P (2008). Confusing cortical columns. *Proceedings of the National Academy of Sciences of the United States of America*. **105**: 12099–12100.

Ramón y Cajal S (1909). Histologie du système nerveux de l'homme & des vertébrés. Maloine.

Rauch A, La Camera G, Lüscher HR, Senn W, and Fusi S (2003). Neocortical pyramidal cells respond as integrate-and-fire neurons to in vivo-like input currents. *Journal of Neurophysiology*. **90**: 1598–1612.

Richardson MJE (2007). Firing-rate response of linear and nonlinear integrate-and-fire neurons to modulated current-based and conductance-based synaptic drive. *Physical Review E.* **76**: 021919.

— (2008). Spike-train spectra and network response functions for non-linear integrate-and-fire neurons. *Biological Cybernetics.* **99**: 381–392.

— (2009). Dynamics of populations and networks of neurons with voltage-activated and calcium-activated currents. *Physical Review E.* **80**: 021928.

Richardson MJE, Brunel N, and Hakim V (2003). From subthreshold to firing-rate resonance. *Journal of Neurophysiology.* **89**: 2538–2554.

Richert M, Nageswaran JM, Dutt N, and Krichmar JL (2011). An efficient simulation environment for modeling large-scale cortical processing. *Frontiers in neuroinformatics.* **5**: 19.

Risken H (1996). The Fokker-Planck Equation: Methods of Solution and Applications. 2nd ed. Springer.

Romand S, Wang Y, Toledo-Rodriguez M, and Markram H (2011). Morphological Development of Thick-Tufted Layer V Pyramidal Cells in the Rat Somatosensory Cortex. *Frontiers in Neuroanatomy.* **5**.

Rossant C, Goodman DFM, Fontaine B, Platkiewicz J, Magnusson AK, and Brette R (2011). Fitting neuron models to spike trains. *Frontiers in neuroscience.* **5**: 9.

Rossant C, Goodman DFM, Platkiewicz J, and Brette R (2010). Automatic fitting of spiking neuron models to electrophysiological recordings. *Frontiers in neuroinformatics.* **4**: 2.

Rudy B, Fishell G, Lee S, and Hjerling-Leffler J (2010). Three groups of interneurons account for nearly 100% of neocortical GABAergic neurons. *Developmental Neurobiology.* **71**: 45–61.

Schiller J, Major G, Koester HJ, and Schiller Y (2000). NMDA spikes in basal dendrites of cortical pyramidal neurons. *Nature.* **404**: 285–289.

Schiller J, Schiller Y, Stuart G, and Sakmann B (1997). Calcium action potentials restricted to distal apical dendrites of rat neocortical pyramidal neurons. *The Journal of Physiology.* **505 (Pt 3)**: 605–616.

Schubert D, Kötter R, and Staiger JF (2007). Mapping functional connectivity in barrel-related columns reveals layer- and cell type-specific microcircuits. *Brain Structure and Function.* **212**: 107–119.

Schwalger T, Fisch K, Benda J, and Lindner B (2010). How Noisy Adaptation of Neurons Shapes Interspike Interval Histograms and Correlations. *PLoS Computational Biology.* **6**: e1001026.

Schwalger T and Lindner B (2013). Patterns of interval correlations in neural oscillators with adaptation. *Frontiers in Computational Neuroscience*. **7**: 164.

Sekerli M, Del Negro CA, Lee RH, and Butera RJ (2004). Estimating action potential thresholds from neuronal time-series: new metrics and evaluation of methodologies. *IEEE transactions on bio-medical engineering*. **51**: 1665–1672.

Shamir M and Sompolinsky H (2006). Implications of neuronal diversity on population coding. *Neural computation*. **18**: 1951–1986.

Shepherd GMG (2009). Intracortical cartography in an agranular area. *Frontiers in neuroscience*. **3**: 337–343.

Sherman SM (2012). Thalamocortical interactions. *Current Opinion in Neurobiology*. **22**: 575–579.

Shu Y, Duque A, Yu Y, Haider B, and McCormick DA (2007a). Properties of Action-Potential Initiation in Neocortical Pyramidal Cells: Evidence From Whole Cell Axon Recordings. *Journal of Neurophysiology*. **97**: 746–760.

Shu Y, Yu Y, Yang J, and McCormick DA (2007b). Selective control of cortical axonal spikes by a slowly inactivating K+ current. *Proceedings of the National Academy of Sciences*. **104**: 11453–11458.

Silberberg G, Gupta A, and Markram H (2002). Stereotypy in neocortical microcircuits. *Trends in Neurosciences*. **25**: 227–230.

Silberberg G and Markram H (2007). Disynaptic Inhibition between Neocortical Pyramidal Cells Mediated by Martinotti Cells. *Neuron*. **53**: 735–746.

Skinner FK, Turrigiano GG, and Marder E (1993). Frequency and burst duration in oscillating neurons and two-cell networks. *Biological Cybernetics*. **69**: 375–383.

Somogyi P, Tamas G, Lujan R, and Buhl EH (1998). Salient features of synaptic organisation in the cerebral cortex. *Brain research. Brain research reviews*. **26**: 113–135.

Soudry D and Meir R (2012). Conductance-based neuron models and the slow dynamics of excitability. *Frontiers in Computational Neuroscience*. **6**: 4.

Spain WJ, Schwindt PC, and Crill WE (1987). Anomalous rectification in neurons from cat sensorimotor cortex in vitro. *Journal of Neurophysiology*. **57**: 1555–1576.

Sporns O (2014). Contributions and challenges for networkmodels in cognitive neuroscience. *Nature Publishing Group*. **17**: 652–660.

Spruston N (2008). Pyramidal neurons: dendritic structure and synaptic integration. *Nature Reviews Neuroscience*. **9**: 206–221.

Staiger JF (2004). Functional Diversity of Layer IV Spiny Neurons in Rat Somatosensory Cortex: Quantitative Morphology of Electrophysiologically Characterized and Biocytin Labeled Cells. *Cerebral Cortex*. **14**: 690–701.

Stein RB (1965). A Theoretical Analysis of Neuronal Variability. *Biophysical Journal*. **5**: 173–194.

Sterratt D, Graham B, Gillies A, and Willshaw D (2011). Principles of Computational Modelling in Neuroscience. Cambridge University Press.

Stuart G, Schiller J, and Sakmann B (1997). Action potential initiation and propagation in rat neocortical pyramidal neurons. *The Journal of Physiology*. **505 (Pt 3)**: 617–632.

Swadlow HA (1989). Efferent neurons and suspected interneurons in S-1 vibrissa cortex of the awake rabbit: receptive fields and axonal properties. *Journal of Neurophysiology*. **62**: 288–308.

Thomson AM (2010). Neocortical layer 6, a review. *Frontiers in Neuroanatomy*. **4**: 1–14.

Thomson AM and Lamy C (2007). Functional maps of neocortical local circuitry. *Frontiers in neuroscience*. **1**: 19–42.

Toib A, Lyakhov V, and Marom S (1998). Interaction between duration of activity and time course of recovery from slow inactivation in mammalian brain Na^+ channels. *The Journal of neuroscience*. **18**: 1893–1903.

Tsodyks M, Pawelzik K, and Markram H (1998). Neural networks with dynamic synapses. *Neural computation*. **10**: 821–835.

Uhlenbeck GE and Ornstein LS (1930). On the theory of the Brownian motion. *Physical Review*. **36**: 823.

Vilin YY and Ruben PC (2001). Slow inactivation in voltage-gated sodium channels: molecular substrates and contributions to channelopathies. *Cell biochemistry and biophysics*. **35**: 171–190.

Wang XJ and Buzsáki G (1996). Gamma oscillation by synaptic inhibition in a hippocampal interneuronal network model. *The Journal of neuroscience*. **16**: 6402–6413.

Wang Y, Gupta A, Toledo-Rodriguez M, Wu CZ, and Markram H (2002). Anatomical, physiological, molecular and circuit properties of nest basket cells in the developing somatosensory cortex. *Cerebral Cortex*. **12**: 395–410.

Wang Y, Markram H, Goodman PH, Berger TK, Ma J, and Goldman-Rakic PS (2006). Heterogeneity in the pyramidal network of the medial prefrontal cortex. *Nature Neuroscience*. **9**: 534–542.

Watakabe A, Hirokawa J, Ichinohe N, Ohsawa S, Kaneko T, Rockland KS, and Yamamori T (2012). Area-specific substratification of deep layer neurons in the rat cortex. *The Journal of Comparative Neurology*. **520**: 3553–3573.

White JA, Rubinstein JT, and Kay AR (2000). Channel noise in neurons. *Trends in Neurosciences*. **23**: 131–137.

Woodruff AR, McGarry LM, Vogels TP, Inan M, Anderson SA, and Yuste R (2011). State-Dependent Function of Neocortical Chandelier Cells. *Journal of Neuroscience*. **31**: 17872–17886.

Woodruff A (2009). Depolarizing effect of neocortical chandelier neurons. *Frontiers in Neural Circuits*. **3**.

Woodruff AR, Anderson SA, and Yuste R (2010). The enigmatic function of chandelier cells. *Frontiers in neuroscience*. **4**: 201.

Woolsey TA and Van der Loos H (1970). The structural organization of layer IV in the somatosensory region (SI) of mouse cerebral cortex. The description of a cortical field composed of discrete cytoarchitectonic units. *Brain research*. **17**: 205–242.

Yamauchi S, Kim H, and Shinomoto S (2011). Elemental spiking neuron model for reproducing diverse firing patterns and predicting precise firing times. *Frontiers in Computational Neuroscience*. **5**: 42.

Yim M, Aertsen A, and Rotter S (2013). Impact of intrinsic biophysical diversity on the activity of spiking neurons. *Physical review. E, Statistical, nonlinear, and soft matter physics*. **87**: 032710.

Yu Y, Shu Y, and McCormick DA (2008). Cortical Action Potential Backpropagation Explains Spike Threshold Variability and Rapid-Onset Kinetics. *Journal of Neuroscience*. **28**: 7260–7272.

Yu Y, Hill AP, and McCormick DA (2012). Warm Body Temperature Facilitates Energy Efficient Cortical Action Potentials. *PLoS Computational Biology*. **8**: e1002456.

Zaitsev AV, Povysheva NV, Gonzalez-Burgos G, and Lewis DA (2012). Electrophysiological classes of layer 2/3 pyramidal cells in monkey prefrontal cortex. *Journal of Neurophysiology*. **108**: 595–609.

Appendix A

Dynamic I-V Analysis MATLAB Toolbox

A.1 Electrode Filter Function

```
function [ V,filter ] = ElecFilter(Iin,Vrec,dt,correct)
%ElecFilter Function to compensate for electrode capacitance in strong,
%high-frequency single electrode recordings. Based on the method of Badel
%et al. , J. Neurophysiol., 99: 656-666 (2008).
%Inputs:
%   Iin - Input current
%   Vrec - Recorded voltage
%   dt - Time step
%   correct - Points after maximum from which to fit exponential to filter
%           function
%Outputs:
%   V - Filtered voltage
%   filter - Electrode filter function

%% Define Constants

options = optimset('TolFun',1e-10,'Display','off');
a=find(Iin,1,'first'); b=find(Iin,1,'last'); scrsz = get(0,'ScreenSize');
dvrecdt=[diff(Vrec); Vrec(end)-Vrec(end-1)]/dt;
dIdt=[diff(Iin);Iin(end)-Iin(end-1)]/dt;
delta=1;
```

```
Erest=mean(Vrec(1:a-1));
vthresh=-20; vth=30;
vmin=-85;vmax=-30;
vbin=(vmin:delta:vmax)'; vfit=(vmin:0.1*delta:vmax)';

%% Locate Spikes

dvrecdtleft=[dvrecdt(1);dvrecdt(1:end-1)];
kspikerec=find(dvrecdtleft>=0 & dvrecdt<0 & Vrec>=vthresh);
nkspike=numel(kspikerec);
rate=nkspike/40;
disp(['Mean Firing Rate = ',num2str(rate),' Hz'])
% figure,plot(time,vrec,time(kspikerec),vrec(kspikerec),'bx')

%% Select Data >200ms post spike

if isempty(kspikerec) == 0
    [k200rec] = SelectData(Vrec,dt,kspikerec,200);
else
    k200rec = 1:length(Vrec);
end

%% Electrode Filter

flen=20;M=flen/dt;ftime=(0:dt:flen)';
[f,ffit,fbeta,filter] = FilterFunc(Iin(a:b),Vrec(a:b),dvrecdt(a:b),dIdt(a:b),...
    k200rec,Erest,correct);
disp(['Electrode Filter Fit Parameters:',10,...
    'A1 = ',num2str(fbeta(1)),' 1/pA',10,...
    'tau1 = ',num2str(fbeta(2)),' ms',10,...
    'A2 = ',num2str(fbeta(3)),' 1/pA',10,...
    'tau2 = ',num2str(fbeta(4)),' ms',10])

figure,plot(ftime,f,ftime,ffit,'--',ftime,filter,'--');
xlabel('Time (ms)'),ylabel('Filter f(t) (1/pF)'),title('Electrode Filter')
xlim([0 5])

If=conv(filter,Iin);If=If(1:length(Iin));
```

```
V=Vrec-If;

%% Functions

    function [f,ffit,fbeta,ffit2] = FilterFunc(I, v, dvdt, dIdt, k200, Erest, correct)
        L = Erest - delta/2; U = Erest + delta/2;
        ind2=find(v>=L & v<U);ind=intersect(ind2,k200);
        I=I(ind);dvdt=dvdt(ind);N=length(ind);

        dIdt2=[dIdt(ind),zeros(N,M)];
        dIdt=[zeros(M,1);dIdt];

        for k=1:M
            dIdttemp=dIdt(M+1-k:end-k);
            dIdt2(:,k+1)=dIdttemp(ind);
        end

        dIdt=dIdt2;

        %Calculate filter
        sigmaI=I'*I/N - (sum(I)/N)^2;
        S=I'*dIdt(:,2:end)/N - sum(I)*sum(dIdt(:,2:end))/(N^2);
        X=dIdt(:,2:end)'*dIdt(:,2:end)/N - ...
            sum(dIdt(:,2:end))'*sum(dIdt(:,2:end))/(N^2);
        A=X-S'*S/sigmaI;
        sigmadvdtI=dvdt'*I/N - sum(dvdt)*sum(I)/(N^2);
        H=dvdt-(sigmadvdtI/sigmaI)*I;
        B=(H'*dIdt(:,2:end)/N - sum(H)*sum(dIdt(:,2:end))/(N^2))';

        f=[0;A\B];

        %Fit to filter tail
        fmax=find(f==max(f))+correct;fbeta0=[1e-2,1,1e-2,20];
        lb=[-Inf,0,-Inf,0];ub=[Inf,Inf,Inf,Inf];
        fbeta = lsqcurvefit(@FilterFit,fbeta0,ftime(fmax+1:end),...
            f(fmax+1:end),lb,ub,options);
        ffit = FilterFit(fbeta,ftime(fmax+1:end));
        ffit=[f(1:fmax);ffit];
```

```
        taumin=find(fbeta==min(fbeta(2),fbeta(4)));
        fbeta2=[fbeta(taumin-1),fbeta(taumin)];
        ffit2 = FilterFit2(fbeta2,ftime(fmax+1:end));
        ffit2=[f(1:fmax);ffit2];
    end

end

function [ffit] = FilterFit(beta,x)
    ffit = beta(1)*exp(-x/beta(2)) + beta(3)*exp(-x/beta(4));
end

function [ffit] = FilterFit2(beta,x)
    ffit = beta(1)*exp(-x/beta(2));
end
```

A.2 Dynamic I-V Analysis Main Function

```
function [ C,beta0,betaTAU,betaE,DT,betaVT ] = DynIVAnalysis( I,V,dt,tbin )
%DYNIVANALYSIS Implementation of the Dynamic I-V Curve method (Badel et
%al., J. Neurophysiol., 99: 656-666, 2008). Can accept a single sweep or
%multiple sweeps to average.
%Inputs:
%   I - Input current. Matrix of size (no. time steps x no. sweeps).
%       Must have a null period (I=0) at the beginning of each sweep so the
%       resing potential can be estimated.
%   V - Recorded voltage. Matrix of the same size as I. If recording
%       from a single electode then the voltage must be filtered. See
%       appendix B of Badel et al. (2008) for details of the electrode
%       filter, and function ElecFilter.m.
%   dt - Time step size.
%   tbin - Lower bounds of the time bins for the post-spike fit. If left
%       empty (i.e. tbin=[]) then the default is used, which is
%       tbin=[5 10 20 30 50 100].
%Outputs:
%   C - Membrane capacitance
%   beta0 - Vector of pre-spike fit parameters: 1/beta0(1)=tau,
%       beta0(2)=E, beta0(3)=DT, and beta0(4)=VT.
```

```
%   betaTAU - Vector of post-spike fit parameters for 1/tau.
%       betaTAU(1)=1/tau=beta0(1), betaTAU(2)=A1, and betaTAU(3)=tau1. Use
%       SingleExp.m to plot.
%   betaE - Vector of post-spike fit parameters for E.
%       betaE(1)=E=beta0(2), betaE(2)=E1, betaE(3)=tauE1, betaE(4)=E2, and
%       betaE(5)=tauE2. Use DoubleExp.m to plot.
%   DT - Mean value of the spike width over the pre- and post-spike fits.
%       Note that this parameter follows no specific post-spike dynamics.
%   betaVT(1)=VT=beta0(4), betavT(2)=VT1, and betavT(3)=tauT. Use
%       SingleExp.m to plot.
%       N.B. See Figure 3B from Badel et al. (2008) for post-spike fits.

scrsz=get(0,'screensize');
scrhalf=[1 scrsz(4)/2 scrsz(3) scrsz(4)/2];

a=find(I(:,1),1,'first');%Find end of null period
Vmin=floor(mean(V(1:a-1,1)))-3;%Miniumum voltage for fit
delta=1;Vmax=-10;Vbin=(Vmin:delta:Vmax)';%Binned voltage
vfit=(Vbin(1):.1*delta:Vbin(end))';%Voltage for fit
RefTime=200;%Post-spike time to remove for pre-spike fit

%Default post-spike time bins
if isempty(tbin)
    tmin = [5 10 20 30 50 100];
    tmax = [10 20 30 50 100 200];
else
    tmin = tbin;
    tmax=[tmin(2:end) tmin(end)+100];
end

nsweeps=size(I,2);%No. sweeps to analyse

%Allocate memory
C=zeros(1,nsweeps);
TAUpoints=zeros(nsweeps,length(tmin)+1);
Epoints=zeros(nsweeps,length(tmin)+1);
DTpoints=zeros(nsweeps,length(tmin)+1);
VTpoints=zeros(nsweeps,length(tmin)+1);
```

```
F0=zeros(length(Vbin),nsweeps);F0SE=zeros(length(Vbin),nsweeps);
F0fit=zeros(length(vfit),nsweeps);beta0=zeros(4,nsweeps);
hDIVFig=zeros(1,nsweeps);
hrefDIVFig=zeros(1,nsweeps);

Fval=10;
Vval=Vbin(end);

%Analyse each sweep
for k=1:nsweeps
    if nsweeps>1
        disp(['Analysis Sweep Number ',num2str(k)])
    end

    %Locate spikes
    kSpike=LocateSpikes(V(:,k),dt,-30);
    tDiff=dt*[kSpike(1);diff(kSpike)];

    %Capacitance
    C(k)=Capacitance(I(:,k),V(:,k),dt,Vbin,RefTime);
    disp([' C = ',num2str(C(k)),' pF',10])

    %Pre-spike fit
    disp(' Pre-spike Fit')
    [F0(:,k),F0SE(:,k),F0fit(:,k),beta0(:,k)] = EIFfit(I(:,k),V(:,k),...
        C(k),dt,kSpike,Vbin,RefTime,Fval,Vval);
    disp([' Sub-Threshold Parameters',10,...
        '  tau = ',num2str(1/beta0(1,k)),' ms',10,...
        '  E = ',num2str(beta0(2,k)),' mV',10,...
        '  DT = ',num2str(beta0(3,k)),' mV',10,...
        '  V_T = ',num2str(beta0(4,k)),' mV',10])

    %Plot pre-spike fit
    hDIVFig(k)=figure;
    hold on
    plot(vfit,F0fit(:,k),'r')
    errorbar(Vbin,F0(:,k),F0SE(:,k),'.')
    set(gca,'xlim',[Vbin(1) ceil(min(Vbin(F0(:,k)>=10))/5)*5],'ylim',...
```

```
        [floor(min(F0(:,k))) 10])
    xlabel('Voltage (mV)'),ylabel('F(V) (mV/ms)')

    %Post-spike Fit
    disp(' Refractory Fit')
    [ TAUpoints(k,:),Epoints(k,:),DTpoints(k,:),VTpoints(k,:),F,FSE,Ffit ] ...
        = rEIFfit( I(:,k),V(:,k),dt,kSpike,kSpike(tDiff>=RefTime),C(k),...
        beta0(:,k),tmin,tmax,Vbin,Fval,Vval);

    %Plot post-spike fits
    hrefDIVFig(k)=figure('position',scrhalf);
    for kk=1:numel(tmin)
        subplot(ceil(numel(tmin)/3),3,kk)
        hold on
        plot([Vbin(1) Vbin(end)],[0 0],'--','color',[.7 .7 .7])
        plot(vfit,F0fit(:,k),'k')
        plot(vfit,Ffit(:,kk),'r')
        errorbar(Vbin,F(:,kk),FSE(:,kk),'.')
        set(gca,'xlim',[Vbin(1) Vbin(end)],'ylim',[floor(min(min(F))) 10])
        xlabel('Voltage (mV)'),ylabel('F(V) (mV/ms)')
        title([num2str(tmin(kk)),'ms<t<',num2str(tmax(kk)),'ms'])
    end
end

%Fit post-spike parameter behaviour
tPost=[(tmin+tmax)/2 (tmax(end)+50)];
if nsweeps>1
    C=mean(C);
    TAUmean=mean(TAUpoints);TAUse=std(TAUpoints)/sqrt(size(TAUpoints,1));
    Emean=mean(Epoints);Ese=std(Epoints)/sqrt(size(Epoints,1));
    DTmean=mean(DTpoints);DTse=std(DTpoints)/sqrt(size(DTpoints,1));
    vTmean=mean(VTpoints);vTse=std(VTpoints)/sqrt(size(VTpoints,1));

    [ betaTAU,betaE,betaVT,tPostFit,TAUfit,Efit,vTfit ] = ...
        Paramfit( TAUmean,Emean,vTmean,tPost,2 );
    DT=mean(DTmean);

    figure
```

```
    subplot(221),hold on
    plot(tPostFit,TAUfit,'r')
    errorbar(tPost,TAUmean,TAUse,'k.')
    xlabel('Post Spike Time (ms)'); ylabel('1/\tau_m (ms^{-1})');
    subplot(222),hold on
    plot(tPostFit,Efit,'r')
    errorbar(tPost,Emean,Ese,'k.')
    xlabel('Post Spike Time (ms)'); ylabel('E_m (mV)');
    subplot(223),hold on
    plot([0 tPost(end)],[DT DT],'r')
    errorbar(tPost,DTmean,DTse,'k.')
    xlabel('Post Spike Time (ms)'); ylabel('\Delta_T (mV)');
    subplot(224),hold on
    plot(tPostFit,vTfit,'r')
    errorbar(tPost,vTmean,vTse,'k.')
    xlabel('Post Spike Time (ms)'); ylabel('V_T (mV)');
else
    [ betaTAU,betaE,betaVT,tPostFit,TAUfit,Efit,vTfit ] = ...
        Paramfit( TAUpoints,Epoints,VTpoints,tPost,2 );

    figure
    subplot(221)
    plot(tPostFit,TAUfit,'r',tPost,TAUpoints,'k.')
    xlabel('Post Spike Time (ms)'); ylabel('1/\tau_m (ms^{-1})');
    subplot(222)
    plot(tPostFit,Efit,'r',tPost,Epoints,'k.')
    xlabel('Post Spike Time (ms)'); ylabel('E_m (mV)');
    subplot(223)
    plot([0 tPost(end)],[mean(DTpoints) mean(DTpoints)],'r',tPost,DTpoints,'k.')
    xlabel('Post Spike Time (ms)'); ylabel('\Delta_T (mV)');
    subplot(224)
    plot(tPostFit,vTfit,'r',tPost,VTpoints,'k.')
    xlabel('Post Spike Time (ms)'); ylabel('V_T (mV)');

    DT=mean(DTpoints);
end

disp(['1/tau Refractory Parameters:',10,...
```

```
'    A1 = ',num2str(betaTAU(2)),' ms',10,...
'    tau1 = ',num2str(betaTAU(3)),' ms',10,...
'E Refractory Parameters:',10,...
'    E1 = ',num2str(betaE(2)),' mV',10,...
'    tauE1 = ',num2str(betaE(3)),' ms',10,...
'    E2 = ',num2str(betaE(4)),' mV',10,...
'    tauE2 = ',num2str(betaE(5)),' ms',10,...
'vT Refractory Parameters:',10,...
'    VT1 = ',num2str(betaVT(2)),' mV',10,...
'    tauT = ',num2str(betaVT(3)),' ms',10,...
'mean DT = ',num2str(DT),' mV',10])
end
```

A.3 Membrane Capacitance Calculation Function

```
function [ C ] = Capacitance( I,V,dt,Vbin,RefTime )
%CAPACITANCE Calculate the membrane capacitance. Details of method in Badel
%et al., J. Neurophysiol., 99: 656-666 (2008).
%   Inputs
%       I: Input Current
%       V: Voltage response
%       dt: Time step
%       Vbin: Binned voltage vector
%   Outputs
%       C: Capacitance

%% Define Constants
a=find(I,1,'first');b=find(I,1,'last');%Find start and end of current input
Erest=mean(V(1:a-1));%Estimate resting potential from initial null period
delta=Vbin(2)-Vbin(1);%Voltage bin size

%% Locate Spikes
kspike=LocateSpikes(V,dt,-20);

%% Select Data
%Remove data RefTime after spikes so parameters are in their baseline state.
dvdt=[diff(V);V(end)-V(end-1)]/dt;
if isempty(kspike) == 0
```

```
    kData=SelectData(V,dt,kspike,RefTime);
else
    kData=1:length(V);
end
kData=intersect(kData,a:b);
IData=I(kData);vData=V(kData);dvdtData=dvdt(kData);

%% Calculate Capacitance via minimisation procedure
temp=vbin-Erest;
krest=find(abs(temp)==min(abs(temp)));
Ce=1:1000;
L = Vbin(krest) - delta/2; U = Vbin(krest) + delta/2;
Ibin = IData(vData>=L & vData<U);
dvdtbin = dvdtData(vData>=L & vData<U);
varbin = var(Ibin*(1./Ce) - repmat(dvdtbin,1,numel(Ce)));
C = Ce(varbin == min(varbin));

figure
loglog(Ce,varbin,C,min(varbin),'.','markersize',15)
xlabel('C_e (pF)')
ylabel('var(I_{in}-C_edV/dt)')
xlim([1 1000])
end
```

A.4 Pre-spike Dynamic I-V Curve Fitting Function

```
function [F,FSE,Ffit,beta0] = EIFfit(I,V,C,dt,kSpike,Vbin,RefTime,Fval,Vval)
%EIFFIT Fit Sub-Threshold Dynamic IV Curve. Details of method in Badel
%et al., J. Neurophysiol., 99: 656-666 (2008).
%Inputs:
%   I - Input current
%   V - Recorded voltage
%   C - Membrane capacitance
%   dt - Time step
%   kSpike - Indices of spike times
%   Vbin - Binned voltage vector
%   RefTime - Post-spike time to remove for pre-spike fit
%   Fval - Maximum F value to fit
```

```
%   Vval - Maximum V value
%Outputs:
%   F - Fitted dynamic IV curve points
%   FSE - Fitted dynamic IV curve standard error of points
%   Ffit - Fitted dynamic IV curve
%   beta0 - Fitted parameters. 1/beta0(1)=tau, beta0(2)=E, beta0(3)=DT,
%           and beta0(4)=VT.

options = optimset('TolFun',1e-10,'Display','off','MaxIter',1000);
a=find(I,1,'first');b=find(I,1,'last');%Find start and end of current input
Erest=mean(V(1:a-1));%Estimate resting potential from initial null period
delta=Vbin(2)-Vbin(1);%Voltage bin size

dvdt=[diff(V);V(end)-V(end-1)]/dt;

%% Select Data
%Remove data RefTime after spikes so parameters are in their baseline state.
kData=SelectData(V,dt,kSpike,RefTime);
kData=intersect(kData,a:b);
IData=I(kData);vData=V(kData);dvdtData=dvdt(kData);

%% Bin membrane current to calculate F(v)
Id = zeros(size(Vbin)); IdSE = zeros(size(Vbin));
Iion = IData - C*dvdtData;

for k = 1:numel(Vbin)
    L = Vbin(k) - delta/2; U = Vbin(k) + delta/2;
    Iionbin = Iion(vData>=L & vData<U);
    Id(k) = mean(Iionbin);
    IdSE(k) = std(Iionbin)/sqrt(numel(Iionbin));
end

F=-Id/C;FSE=IdSE/C;

figure
hold on
plot(vData,Iion/1000,'.','color',[.7 .7 .7])
errorbar(Vbin,Id/1000,IdSE/1000,'r.-')
```

```
set(gca,'ylim',[-2*ceil(max(Iion)/1000) ceil(max(Iion)/1000)],'xlim',[Vbin(1) Vbin(end)])
xlabel('Voltage (mV)'),ylabel('I_{ion} (nA)')

%% Fit IV Curve
vfit=(Vbin(1):0.1*delta:Vbin(end))';
betainitial = [0.05 Erest 1 Erest+20];
lb = [0 Erest-2 0 Erest]; ub = [5 Erest+2 10 0];
beta0 = lsqcurvefit(@EIF,betainitial,Vbin(F<=Fval&Vbin<=Vval),...
    F(F<=Fval&Vbin<=Vval),lb,ub,options);
Ffit = EIF(beta0,vfit);

end
```

A.5 Post-spike Dynamic I-V Curve Fitting Function

```
function [ TAUpoints,Epoints,DTpoints,VTpoints,F,FSE,Ffit ] ...
    = rEIFfit( I,V,dt,kSpike,kSpikeFit,C,beta0,tmin,tmax,Vbin,Fval,Vval )
%REIFFIT2 Fit post-spike dynamic IV curves
%Inputs:
%   I - Input current
%   V - Recorded voltage
%   dt - Time step
%   kSpike - Indices of spike times
%   kspikeFit - Indices of spikes used for fit
%   C - Membrane capacitance
%   beta0 - Fitted parameters of the pre-spike dynamic IV curve.
%           1/beta0(1)=tau, beta0(2)=E, beta0(3)=DT, and beta0(4)=VT.
%   tmin - Lower time bin bounds
%   tmax - Upper time bin bounds
%   Vbin - Binned voltage vector
%   Fval - Maximum F value to fit
%   Vval - Maximum V value
%Outputs:
%   TAUpoints - Points for dynamics of 1/tau
%   Epoints - Points for dynamics of E
%   DTpoints - Points for dynamics of DT
%   VTpoints - Points for dynamics of VT
%   F - Fitted dynamic IV curve points for each time bin
```

```
%   FSE - Fitted dynamic IV curve standard error of points for each time bin
%   Ffit - Fitted dynamic IV curve for each time bin

options = optimset('TolFun',1e-10,'Display','off');

%% Define Constants
t=(0:numel(I)-1)'*dt;
dvdt=[diff(V);V(end)-V(end-1)]/dt;
delta=Vbin(2)-Vbin(1);%Voltage bin size

%% Allocate Memory
vfit=(Vbin(1):0.1*delta:Vbin(end))';
TAUpoints = [zeros(1,numel(tmin)) beta0(1)];
Epoints = [zeros(1,numel(tmin)) beta0(2)];
DTpoints = [zeros(1,numel(tmin)) beta0(3)];
VTpoints = [zeros(1,numel(tmin)) beta0(4)];
F = zeros(numel(Vbin),numel(tmin));
FSE = zeros(numel(Vbin),numel(tmin));
Ffit = zeros(numel(vfit),numel(tmin));

%% Fit Dynamic IV Curves

[~,SpikeFitNo,~]=intersect(kSpike,kSpikeFit);

ntmin=round(tmin/dt);ntmax=round(tmax/dt);ntdiff=ntmax-ntmin;
b=find(I,1,'last');
for k=1:numel(tmin)
    kspikediff2=[diff(kSpike)-ntmin(k);b-kSpike(end)-ntmin(k)];
    mindiff=min(kspikediff2,ntdiff(k));
    vtemp=zeros(size(V));dvdttemp=zeros(size(dvdt));
    Itemp=zeros(size(I));ttemp=zeros(size(I));
    s=1;count=0;
    for j=1:numel(kSpikeFit)
        if mindiff(SpikeFitNo(j))>=0
        vtemp(s:s+mindiff(SpikeFitNo(j)))...
         =V(kSpikeFit(j)+ntmin(k):kSpikeFit(j)+ntmin(k)+mindiff(SpikeFitNo(j)));
        dvdttemp(s:s+mindiff(SpikeFitNo(j)))...
         =dvdt(kSpikeFit(j)+ntmin(k):kSpikeFit(j)+ntmin(k)+mindiff(SpikeFitNo(j)));
```

```
        Itemp(s:s+mindiff(SpikeFitNo(j)))...
         =I(kSpikeFit(j)+ntmin(k):kSpikeFit(j)+ntmin(k)+mindiff(SpikeFitNo(j)));
        ttemp(s:s+mindiff(SpikeFitNo(j)))...
         =t(kSpikeFit(j)+ntmin(k):kSpikeFit(j)+ntmin(k)+mindiff(SpikeFitNo(j)));
        s=s+mindiff(SpikeFitNo(j));
        count=count+1;
        end
    end
    disp([' ',num2str(count),' spikes used in refractory EIF fit for ',...
        num2str(tmin(k)),'-',num2str(tmax(k)),' ms postspike.',10])
    kend=find(Itemp~=0,1,'last');
    vtemp(kend+1:end)=[];dvdttemp(kend+1:end)=[];
    Itemp(kend+1:end)=[];ttemp(kend+1:end)=[];

    Id = zeros(size(Vbin)); IdSE = zeros(size(Vbin));
    Iion = Itemp - C*dvdttemp;

    for j = 1:numel(Vbin)
        L = Vbin(j) - delta/2; U = Vbin(j) + delta/2;
        Iionbin = Iion(vtemp>=L & vtemp<U);
        Id(j) = mean(Iionbin);
        IdSE(j) = std(Iionbin)/sqrt(numel(Iionbin));
    end

    F(:,k) = -Id/C;
    FSE(:,k) = IdSE/C;

    vfit=(Vbin(1):0.1*delta:Vbin(end))';
    lb = [0 -100 0 -100]; ub = [1 -30 5 0];
    Ftemp=F(:,k);FSEtemp=FSE(:,k);

    betaFit = lsqcurvefit(@EIF,beta0,Vbin(Ftemp<=Fval&Vbin<=Vval),...
        Ftemp(Ftemp<=Fval&Vbin<=Vval),lb,ub,options);
    Ffit(:,k) = EIF(betaFit,vfit);

    TAUpoints(k)=betaFit(1); Epoints(k)=betaFit(2);
    DTpoints(k)=betaFit(3); VTpoints(k)=betaFit(4);
end
```

```
end
```

A.6 Function to Fit Post-spike Parameter Dynamics

```
function [ betaTAU,betaE,betaVT,tPostFit,TAUfit,Efit,VTfit ] = Paramfit( TAUpoints,Epoints
%PARAMFIT Fit post-spike parameter response
%Inputs:
%   TAUpoints - Points for dynamics of 1/tau
%   Epoints - Points for dynamics of E
%   VTpoints - Points for dynamics of VT
%   tPost - Post-spike time points
%   EfitExp - Number of exponential functions to fit the dynamics of E to
%   (typically 2)
%Outputs:
%   betaTAU - Vector of post-spike fit parameters for 1/tau.
%       betaTAU(1)=1/tau=beta0(1), betaTAU(2)=A1, and betaTAU(3)=tau1.
%   betaE - Vector of post-spike fit parameters for E.
%       betaE(1)=E=beta0(2), betaE(2)=E1, betaE(3)=tauE1, betaE(4)=E2, and
%       betaE(5)=tauE2.
%   betaVT(1)=VT=beta0(4), betavT(2)=VT1, and betavT(3)=tauT.
%   tPostFit - Time vector for fitted functions
%   TAUfit - Vector of fit to dynamics of 1/tau
%   Efit - Vector of fit to dynamics of E
%   VTfit - Vector of fit to dynamics of VT


options = optimset('TolFun',1e-10,'Display','off');

%% Initial guess
betatau0 = [0 10];
if EfitExp == 1
    betaE0 = [0 10];
elseif EfitExp == 2
    betaE0=[2*Epoints(end) 4/TAUpoints(end) 2*abs(Epoints(end)) 1/TAUpoints(end)];
end
betavT0 = [0 10];
```

```
%% Define bounds
lbtau = [-Inf 0]; ubtau = [Inf Inf];
if EfitExp == 1
    lbE = [0 0]; ubE = [Inf Inf];
elseif EfitExp == 2
    lbE = [-Inf 0 0 0]; ubE = [0 Inf Inf Inf];
end
lbvT = [-Inf 0]; ubvT = [Inf Inf];

%% Fit
betaTAU=lsqcurvefit(@Paramfit_TAUfit,betatau0,tPost,TAUpoints,lbtau,ubtau,options);
if EfitExp == 1
    betaE=lsqcurvefit(@Paramfit_Efit1,betaE0,tPost,Epoints,lbE,ubE,options);
elseif EfitExp == 2
    betaE=lsqcurvefit(@Paramfit_Efit2,betaE0,tPost,Epoints,lbE,ubE,options);
end
betaVT=lsqcurvefit(@Paramfit_vTfit,betavT0,tPost,VTpoints,lbvT,ubvT,options);

tPostFit = 0:0.1:max(tPost)+50;
TAUfit = Paramfit_TAUfit(betaTAU,tPostFit);
if EfitExp == 1
    Efit = Paramfit_Efit1(betaE,tPostFit);
elseif EfitExp == 2
    Efit = Paramfit_Efit2(betaE,tPostFit);
end
VTfit = Paramfit_vTfit(betaVT,tPostFit);

betaTAU=[TAUpoints(end),betaTAU];
betaE=[Epoints(end),betaE];
betaVT=[VTpoints(end),betaVT];

    function TAUf = Paramfit_TAUfit(beta,x)
        TAUf = TAUpoints(end) + beta(1)*exp(-x/beta(2));
    end

    function Ef = Paramfit_Efit1(beta,x)
        Ef = Epoints(end) + beta(1)*exp(-x/beta(2));
    end
```

```
    function Ef = Paramfit_Efit2(beta,x)
        Ef = Epoints(end) + beta(1)*exp(-x/beta(2)) + beta(3)*exp(-x/beta(4));
    end

    function vTf = Paramfit_vTfit(beta,x)
        vTf = VTpoints(end) + beta(1)*exp(-x/beta(2));
    end
end
```

A.7 Additional Functions Required by Toolbox

Function to Locate Action Potentials

```
function [ kSpike ] = LocateSpikes( V,dt,VDetect )
%LOCATESPIKES Locate spikes from a voltage trace.
%
%Inputs:
%   V:       Voltage trace
%   dt:      Time step (ms)
%   VDetect: Voltage above which a spike can be detected - typically
%            vDetect=-30mV for neocortical pyramidal cells.
%
%Outputs:
%   kspike:  Vector of spike indexes

nTraces=size(V,2);
if nTraces==1
    dvdt=[diff(V);V(end)-V(end-1)]/dt;
    dvdtleft=[dvdt(1);dvdt(1:end-1)];
    kSpike=find(V>=VDetect&dvdt<0&dvdtleft>=0);
    kdiff=diff(kSpike);
    tdiff=kdiff*dt;
    kSpike(tdiff<=2)=[];
else
    dvdt=[diff(V);V(end,:)-V(end-1,:)]/dt;
    dvdtleft=[dvdt(1,:);dvdt(1:end-1,:)];
    [kspike_i,kspike_j]=find(V>=VDetect&dvdt<0&dvdtleft>=0);
```

```
    kSpike=cell(1,nTraces);
    for k=1:nTraces
        kSpike{k}=kspike_i(kspike_j==k);
    end
    kdiff=diff(kSpike{k});
    tdiff=kdiff*dt;
    kSpike{k}(tdiff<=2)=[];
end

end
```

Single Exponential Function

```
function [ func ] = SingleExp( beta, t )
%SINGLEEXPFIT Summary of this function goes here

func = beta(1) + beta(2)*exp(-t/beta(3));

end
```

Double Exponential Function

```
function [ func ] = DoubleExp( beta, t )
%DOUBLEEXP Double exponential function

func = beta(1) + beta(2)*exp(-t/beta(3)) + beta(4)*exp(-t/beta(5));

end
```

Data Selection Functions

```
function [kselect] = SelectData(v,dt,kspike,posttime)
%SELECTDATA Select data at least posttime after spikes
    kspikediff=diff(kspike); n=round(posttime/dt);
    nspike=numel(kspike);kselect=zeros(size(v));
    kselect(1:kspike(1))=1:kspike(1);s=kspike(1);
    count=1;
    for k=1:nspike-1
        if kspikediff(k)>n
            kselect(s+1:s+1+kspikediff(k)-n)...
                = kspike(k)+n:kspike(k+1);
```

```
            s=s+1+kspikediff(k)-n;
            count=count+1;
        end
    end
    kend=find(kselect~=0,1,'last');kselect(kend+1:end)=[];
end

function [kselect] = SelectData2(v,dt,kspike,pretime,posttime)
%SELECTDATA2 Select Data pretime before and posttime after spikes
    kspike(kspike<=0)=[];
    npre=round(pretime/dt);
    npost=round(posttime/dt);
    kpre=max(kspike-npre,1);
    kpost=min(kspike+npost,length(v));
    nspike=numel(kspike);kselect=zeros(size(v));
    kselect(1:kpre(1))=1:kpre(1);s=kpre(1);
    count=1;
    for k=1:nspike-1
        if kpre(k+1)-kspike(k)>npost
            kselect(s+1:s+1+kpre(k+1)-kpost(k))...
                = kpost(k):kpre(k+1);
            s=s+1+kpre(k+1)-kpost(k);
            count=count+1;
        end
    end
    kend=find(kselect~=0,1,'last');kselect(kend+1:end)=[];
end
```

Dynamic I-V Curve Quantification Function

```
function [ F ] = EIF( beta, x )
%Exponential Integrate and Fire model ionic current
%beta(1) = 1/taum, beta(2) = Em, beta(3) = deltaT, beta(4) = VT
    F = beta(1)*(beta(2) - x + beta(3)*exp((x-beta(4))/beta(3)));
end
```

Appendix B

Code for Generation of Population of EIF Models

```
function [ Data_gen_class,Variables ] = Generate_EIF( N )
%GENERATEEIF Generate populations of EIF neuron models of layer 2/3, 4,
%slender-tufted layer 5, and thick-tufted layer 5 pyramidal cells. Requires
%MATLAB Statistics toolbox.
%   Input:
%       N = number of cells to generate. 4x1 vector consisting of the
%       number required for each class in the order stated above. If the
%       same number from each class are required just input a single
%       number.
%   Output:
%       Data_gen_class = 4x1 cell array where each element corresponds to
%       the cell classes in the order stated above (Data_gen_class{1} are
%       layer 2/3 cells etc.). Each element in the cell array is an N(k)*5
%       array of parameter values. Rows correspond to to model neurons and
%       columns are parameters [C,tau,E,VT,DT].
%       Variables = Cell array of variable names.

nClass=4;%Number of cell classes
if numel(N)==1
    N=N*ones(nClass,1);
end
```

```
%% Distribution Parameters
Variables={'C';'tau';'E';'VT';'DT'};
DistName={'logn';'logn';'norm';'norm';'logn'};
nVar=numel(DistName);%Number of EIF parameters
mu=[4.87 4.86 4.86 5.61;...%C
    2.67 2.82 2.88 2.9;...%tau
    -79.3 -71.8 -69.9 -68.5;...%E
    -49.5 -48.7 -49.7 -52.7;...%VT
    .227 .213 .235 .0836];%DT
sig=[.258 .289 .251 .273;...%C
    .171 .24 .255 .229;...%tau
    4.27 4.2 4.18 3.98;...%E
    3.81 3.53 3.56 3.59;...VT
    .359 .266 .361 .364];%DT

Rho{1}=...
   [1.0000 -0.2721  0.0042 -0.5636 -0.1307;
   -0.2721  1.0000 -0.1357  0.4244 -0.4509;
    0.0042 -0.1357  1.0000  0.4765 -0.0464;
   -0.5636  0.4244  0.4765  1.0000 -0.3097;
   -0.1307 -0.4509 -0.0464 -0.3097  1.0000];
Rho{2}=...
   [1.0000  0.1124  0.2056 -0.2430 -0.1318;
    0.1124  1.0000  0.2773 -0.0053 -0.1034;
    0.2056  0.2773  1.0000  0.3427 -0.3416;
   -0.2430 -0.0053  0.3427  1.0000 -0.4020;
   -0.1318 -0.1034 -0.3416 -0.4020  1.0000];
Rho{3}=...
   [1.0000  0.3380  0.4681 -0.1710 -0.2218;
    0.3380  1.0000  0.2582 -0.0344 -0.2067;
    0.4681  0.2582  1.0000  0.3974 -0.4300;
   -0.1710 -0.0344  0.3974  1.0000 -0.1410;
   -0.2218 -0.2067 -0.4300 -0.1410  1.0000];
Rho{4}=...
   [1.0000  0.0639  0.1435 -0.2865 -0.2151;
    0.0639  1.0000  0.0773 -0.0066 -0.2062;
    0.1435  0.0773  1.0000  0.3730  0.1508;
```

```
   -0.2865 -0.0066  0.3730  1.0000  0.1949;
   -0.2151 -0.2062  0.1508  0.1949  1.0000];

%% Generate Random Sample
Data_copula_gen=cell(nClass,1);
Data_gen_class=cell(nClass,1);
for k=1:nClass
    %Allocate memory
    Data_copula_gen{k}=zeros(N(k),nVar);
    Data_gen_class{k}=zeros(N(k),nVar);

    %Generate a random sample from the t copula
    Data_copula_gen{k}=copularnd('Gaussian',Rho{k},N(k));

    %Transform the random sample back to the original scale of the data
    for j=1:nVar
        Data_gen_class{k}(:,j)=icdf(DistName{j},Data_copula_gen{k}(:,j),...
            mu(j,k),sig(j,k));
    end
end

end
```

Appendix C

Code for Generation of Population of rEIF Models

```
function [ Data_gen_class,Variables ] = Generate_rEIF( N )
%GENERATEREIF Generate populations of rEIF neuron models of layer 2/3, 4,
%slender-tufted layer 5, and thick-tufted layer 5 pyramidal cells. Requires
%MATLAB Global Optimzation and Statistics toolboxes.
%   Input:
%       N = number of cells to generate. 4x1 vector consisting of the
%       number required for each class in the order stated above. If the
%       same number from each class are required just input a single
%       number.
%   Output:
%       Data_gen_class = 4x1 cell array where each element corresponds to
%       the cell classes in the order stated above (Data_gen_class{1} are
%       layer 2/3 cells etc.). Each element in the cell array is an N(k)*13
%       array of parameter values. Rows correspond to to model neurons and
%       columns are parameters
%       [C,tau,E,VT,DT,Dg,taug,VT1,tauT,E_A1,tau_E1,E_A2,tau_E2]. In the
%       case of cells with a mono-exponential decaying equilibrium
%       potential E_A1=0 and tau_E1=10.
%       Variables = Cell array of variable names.

nClass=4;%Number of cell classes
```

```
if numel(N)==1
    N=N*ones(nClass,1);
end

%% Non-Eref Distribution Parameters
Variables_rEIF={'C';'tau';'E';'VT';'DT';'Dg';'taug';'VT1';'tauT'};
nVar=numel(Variables_rEIF);%Number of EIF parameters
DistName={'logn';'logn';'norm';'norm';'logn';'logn';'logn';'logn';'logn'};
mu=[4.87 4.86 4.86 5.61;...C
    2.67 2.82 2.88 2.9;...tau
    -79.3 -71.8 -69.9 -68.5;...E
    -49.5 -48.7 -49.7 -52.7;...VT
    .227 .213 .235 .0836;...DT
    2.83 3.22 2.91 3.38;...Dg
    2.62 2.65 2.87 2.99;...taug
    3.11 3.03 2.84 2.98;...VT1
    2.49 2.61 2.65 2.44];%tauT
sig=[.258 .289 .251 .273;...C
    .171 .24 .255 .229;...tau
    4.27 4.2 4.18 3.98;...E
    3.81 3.53 3.56 3.59;...VT
    .359 .266 .361 .364;...DT
    .719 .575 .639 .590;...Dg
    .570 .578 .694 .635;...taug
    .368 .436 .335 .421;...VT1
    .442 .345 .479 .432];%tauT

Rho{1}=...
   [1.0000 -0.2721  0.0042 -0.5636 -0.1307  0.2364  0.1288  0.2043 -0.1811;
   -0.2721  1.0000 -0.1357  0.4244 -0.4509 -0.0316 -0.1978 -0.2401 -0.0952;
    0.0042 -0.1357  1.0000  0.4765 -0.0464 -0.0996  0.0114 -0.0582  0.1897;
   -0.5636  0.4244  0.4765  1.0000 -0.3097 -0.1154 -0.0708 -0.2104  0.1030;
   -0.1307 -0.4509 -0.0464 -0.3097  1.0000 -0.0789 -0.0322 -0.1531  0.5705;
    0.2364 -0.0316 -0.0996 -0.1154 -0.0789  1.0000 -0.8146  0.2130  0.0587;
    0.1288 -0.1978  0.0114 -0.0708 -0.0322 -0.8146  1.0000 -0.1387 -0.1869;
    0.2043 -0.2401 -0.0582 -0.2104 -0.1531  0.2130 -0.1387  1.0000 -0.6494;
   -0.1811 -0.0952  0.1897  0.1030  0.5705  0.0587 -0.1869 -0.6494  1.0000];
Rho{2}=...
```

```
   [1.0000  0.1124  0.2056 -0.2430 -0.1318  0.2010  0.1578  0.1739 -0.0830;
    0.1124  1.0000  0.2773 -0.0053 -0.1034 -0.2226  0.4213  0.1214  0.0287;
    0.2056  0.2773  1.0000  0.3427 -0.3416  0.1542  0.2933 -0.0526 -0.0035;
   -0.2430 -0.0053  0.3427  1.0000 -0.4020 -0.1815  0.1829  0.1586 -0.2779;
   -0.1318 -0.1034 -0.3416 -0.4020  1.0000  0.2125 -0.4755 -0.0343  0.2555;
    0.2010 -0.2226  0.1542 -0.1815  0.2125  1.0000 -0.7392  0.0166 -0.0973;
    0.1578  0.4213  0.2933  0.1829 -0.4755 -0.7392  1.0000  0.0415 -0.0620;
    0.1739  0.1214 -0.0526  0.1586 -0.0343  0.0166  0.0415  1.0000 -0.7271;
   -0.0830  0.0287 -0.0035 -0.2779  0.2555 -0.0973 -0.0620 -0.7271  1.0000];
Rho{3}=...
   [1.0000  0.3380  0.4681 -0.1710 -0.2218  0.0724  0.3500  0.0418 -0.1258;
    0.3380  1.0000  0.2582 -0.0344 -0.2067 -0.0662  0.3596 -0.1925  0.1171;
    0.4681  0.2582  1.0000  0.3974 -0.4300 -0.0447  0.3367  0.0282 -0.3766;
   -0.1710 -0.0344  0.3974  1.0000 -0.1410 -0.1432  0.0882  0.1782 -0.2095;
   -0.2218 -0.2067 -0.4300 -0.1410  1.0000 -0.0111 -0.1694 -0.2146  0.6912;
    0.0724 -0.0662 -0.0447 -0.1432 -0.0111  1.0000 -0.7995 -0.0193 -0.0619;
    0.3500  0.3596  0.3367  0.0882 -0.1694 -0.7995  1.0000 -0.0502  0.0137;
    0.0418 -0.1925  0.0282  0.1782 -0.2146 -0.0193 -0.0502  1.0000 -0.5143;
   -0.1258  0.1171 -0.3766 -0.2095  0.6912 -0.0619  0.0137 -0.5143  1.0000];
Rho{4}=...
   [1.0000  0.0639  0.1435 -0.2865 -0.2151  0.0301  0.2344 -0.1657  0.0791;
    0.0639  1.0000  0.0773 -0.0066 -0.2062  0.0809  0.1660  0.0330 -0.0385;
    0.1435  0.0773  1.0000  0.3730  0.1508  0.2124  0.2225 -0.0367  0.0006;
   -0.2865 -0.0066  0.3730  1.0000  0.1949  0.3164 -0.2837 -0.0578  0.0485;
   -0.2151 -0.2062  0.1508  0.1949  1.0000  0.1193 -0.2135  0.0238  0.3646;
    0.0301  0.0809  0.2124  0.3164  0.1193  1.0000 -0.6317  0.0914  0.0114;
    0.2344  0.1660  0.2225 -0.2837 -0.2135 -0.6317  1.0000  0.0645 -0.1816;
   -0.1657  0.0330 -0.0367 -0.0578  0.0238  0.0914  0.0645  1.0000 -0.7549;
    0.0791 -0.0385  0.0006  0.0485  0.3646  0.0114 -0.1816 -0.7549  1.0000];

%% Eref Distribution Parameters

%Double exponential decay distribution parameters
DistName_dexp={'logn';'logn';'logn';'logn'};
mu_dexp=[3.04 2.61 2.65 2.44;...%Ejump
    .0898 .442 .814 1.38;...%Esag
    4.49 4.21 3.97 3.76;...%tsag
    3.86 3.48 3.12 2.62];%t0
```

```
sig_dexp=[.324 .463 .602 .702;...%Ejump
    .549 .599 .594 .493;...;%Esag
    .251 .304 .423 .273;...%tsag
    .328 .379 .540 .519];%t0

Rho_sag{1}=[1.0000   -0.2760    0.2810    0.4070;
   -0.2760    1.0000   -0.4830   -0.6697;
    0.2810   -0.4830    1.0000    0.9244;
    0.4070   -0.6697    0.9244    1.0000];
Rho_sag{2}=[1.0000    0.1296    0.0601    0.1833;
    0.1296    1.0000   -0.1522   -0.5280;
    0.0601   -0.1522    1.0000    0.8862;
    0.1833   -0.5280    0.8862    1.0000];
Rho_sag{3}=[1.0000    0.3431   -0.5353   -0.2578;
    0.3431    1.0000   -0.7634   -0.8683;
   -0.5353   -0.7634    1.0000    0.9223;
   -0.2578   -0.8683    0.9223    1.0000];
Rho_sag{4}=[1.0000   -0.2209   -0.1987    0.6116;
   -0.2209    1.0000   -0.2795   -0.6076;
   -0.1987   -0.2795    1.0000    0.5650;
    0.6116   -0.6076    0.5650    1.0000];

Rho_nosag{1}=[1.0000   -0.6752;
   -0.6752    1.0000];
Rho_nosag{2}=[1.0000   -0.3825;
   -0.3825    1.0000];
Rho_nosag{3}=[1.0000   -0.3575;
   -0.3575    1.0000];
Rho_nosag{4}=[1.0000    0.9944;
    0.9944    1.0000];

%Mono exponential decay distribution parameters (drawn from single
%distribution)
DistName_mexp={'logn';'logn'};
mu_mexp=[3.09;...A
    2.70];%tau
sig_mexp=[.337;...A
    .318];%tau
```

```
nVarSag=numel(DistName_dexp);
nVarNoSag=numel(DistName_mexp);

%% Sag Probability
Psag=[0.3226;
    0.7586;
    0.6897;
    0.9362];

%% Randomly Assign Cells with E sag or no sag
CellSag_class=cell(nClass,1);
NSag=zeros(nClass,1);
NNoSag=zeros(nClass,1);
for k=1:nClass
    temp=rand(N(k),1);
    CellSag_class{k}=(temp<Psag(k));
    NSag(k)=sum(CellSag_class{k});
    NNoSag(k)=N(k)-NSag(k);
end

%% Generate Random Sample Excluding Eref Parameters
disp('Generate Random Sample: Non-Eref Parameters')
Data_copula_gen=cell(nClass,1);
Data_gen_class=cell(nClass,1);
for k=1:nClass
    %Generate a random sample from the t copula
    Data_copula_gen{k}=copularnd('Gaussian',Rho{k},N(k));

    %Transform the random sample back to the original scale of the data
    Data_gen_class{k}=zeros(size(Data_copula_gen{k}));
    for j=1:nVar
        Data_gen_class{k}(:,j)=icdf(DistName{j},Data_copula_gen{k}(:,j),...
            mu(j,k),sig(j,k));
    end
end

%% Generate Random Sample of Eref Parameters
```

```
%Cells with sag
disp('Generate Random Sample: Eref Parameters - Cells with Sag')
Data_copula_gen_sag=cell(nClass,1);
Data_gen_class_sag=cell(nClass,1);
for k=1:nClass
    if NSag(k)>0
        %Generate a random sample from the Gaussian copula
        Data_copula_gen_sag{k}=copularnd('Gaussian',Rho_sag{k},NSag(k));

        %Transform the random sample back to the original scale of the data
        Data_gen_class_sag{k}=zeros(size(Data_copula_gen_sag{k}));
        for j=1:nVarSag
            Data_gen_class_sag{k}(:,j)=icdf(DistName_dexp{j},...
                Data_copula_gen_sag{k}(:,j),mu_dexp(j,k),sig_dexp(j,k));
        end
    end
end

%Cells with no sag
disp('Generate Random Sample: Eref Parameters - Cells with No Sag')
Data_copula_gen_nosag=cell(nClass,1);
Data_gen_class_nosag=cell(nClass,1);
for k=1:nClass
    if NNoSag(k)>0
        %Generate a random sample from the t copula
        Data_copula_gen_nosag{k}=copularnd('Gaussian',Rho_nosag{k},...
            NNoSag(k));

        %Transform the random sample back to the original scale of the data
        Data_gen_class_nosag{k}=zeros(size(Data_copula_gen_nosag{k}));
        for j=1:nVarNoSag
            Data_gen_class_nosag{k}(:,j)=icdf(DistName_mexp{j},...
                Data_copula_gen_nosag{k}(:,j),mu_mexp(j),sig_mexp(j));
        end
    end
end

%% Fit Double Exponential Parameters Cells' Sag Response
```

```
disp('Fit Double Exponential to Cells'' Sag Response')
betaE=cell(nClass,1);
Ejump=cell(nClass,1);
Esag=cell(nClass,1);
tsag=cell(nClass,1);
t0=cell(nClass,1);
for k=1:nClass
    betaE{k}(~CellSag_class{k},:)=[repmat([0 10],NNoSag(k),1),...
        Data_gen_class_nosag{k}];
    Ejump{k}=Data_gen_class_sag{k}(:,1);
    Esag{k}=Data_gen_class_sag{k}(:,2);
    tsag{k}=Data_gen_class_sag{k}(:,3);
    t0{k}=Data_gen_class_sag{k}(:,4);
end

ind_total=1;
Tpoints=cell(nClass,1);
Epoints=cell(nClass,1);
opts=optimset('Display', 'off');
gs=GlobalSearch('NumStageOnePoints',200,'NumTrialPoints',1000,...
    'StartPointsToRun','bounds-ineqs','Display', 'off');
warning off

dt=.05;t=(0:dt:300)';
func_dexp=@(x,t) -x(1)*exp(-t/x(2))+x(3)*exp(-t/x(4));
gs2=GlobalSearch('NumStageOnePoints',500,'NumTrialPoints',2000,...
    'StartPointsToRun','bounds-ineqs','Display', 'off');

for ClassInd=1:nClass
    ind=1;
    Tpoints{ClassInd}=zeros(N(ClassInd),3);
    Epoints{ClassInd}=zeros(N(ClassInd),3);
    for k=1:N(ClassInd)
        if CellSag_class{ClassInd}(k)
            disp([' ',num2str(100*ind_total/sum(NSag)),'% Complete'])
            Tpoints{ClassInd}(k,:)=[0 t0{ClassInd}(ind) tsag{ClassInd}(ind)];
            Epoints{ClassInd}(k,:)=[Ejump{ClassInd}(ind) 0 -Esag{ClassInd}(ind)];
            func=@(x) sum((-x(1)*exp(-Tpoints{ClassInd}(k,:)/x(2)) +...
```

```
        x(3)*exp(-Tpoints{ClassInd}(k,:)/x(4)) -...
        Epoints{ClassInd}(k,:)).^2);
    c=@(x) (x(1)/x(2)^2)*((x(1)*x(4))/(x(3)*x(2)))^(-x(4)/(x(4)-x(2)))-...
        (x(3)/x(4)^2)*((x(1)*x(4))/(x(3)*x(2)))^(-x(2)/(x(4)-x(2)));
    ceq=@(x) [x(2)*x(4)*log((x(1)*x(4))/(x(3)*x(2)))/(x(4)-x(2))-...
        tsag{ClassInd}(ind);
        x(1)*exp(-tsag{ClassInd}(ind)/x(2))-...
        x(3)*exp(-tsag{ClassInd}(ind)/x(4))-Esag{ClassInd}(ind)];
    confun=@(x) deal(c(x),ceq(x));
    problem=createOptimProblem('fmincon',...
        'objective',func,...
        'x0',[.5*Ejump{ClassInd}(ind) .5*tsag{ClassInd}(ind) ...
        1.5*Ejump{ClassInd}(ind) .55*tsag{ClassInd}(ind)],...
        'lb',[0 0 0 0],...
        'ub',[Inf Inf Inf Inf],...
        'Aineq',[1 0 -1 0;0 -1 0 1],...
        'bineq',[0;0],...
        'Aeq',[-1 0 1 0],...
        'beq',Ejump{ClassInd}(ind),...
        'nonlcon',confun,...
        'options',opts);
%           betaE{ClassInd}(k,:)=fmincon(problem);
    betaE{ClassInd}(k,:)=run(gs,problem);

    Espiketemp=func_dexp(betaE{ClassInd}(k,:),t);
    Esagtemp=-min(Espiketemp);
    if abs(Esag{ClassInd}(ind)-Esagtemp)>.2*Esag{ClassInd}(ind)
        problem=createOptimProblem('fmincon',...
            'objective',func,...
            'x0',[.5*Ejump{ClassInd}(ind)*(.9+.2*rand(1)) ...
            .5*tsag{ClassInd}(ind)*(.9+.2*rand(1)) ...
            1.5*Ejump{ClassInd}(ind)*(.9+.2*rand(1)) ...
            .55*tsag{ClassInd}(ind)*(.9+.2*rand(1))],...
            'lb',[0 0 0 0],...
            'ub',[Inf Inf Inf Inf],...
            'Aineq',[1 0 -1 0;0 -1 0 1],...
            'bineq',[0;0],...
            'Aeq',[-1 0 1 0],...
```

```
                    'beq',Ejump{ClassInd}(ind),...
                    'nonlcon',confun,...
                    'options',opts);
    %              betaE{ClassInd}(k,:)=fmincon(problem);
                betaE{ClassInd}(k,:)=run(gs2,problem);
            end

            ind=ind+1;ind_total=ind_total+1;
        end
    end
end

%% Store Data
for k=1:nClass
    Data_gen_class{k}=[Data_gen_class{k},betaE{k}];
end
Variables=[Variables_rEIF;'A1';'tau1';'A2';'tau2'];
end
```